THESIS FOR THE DEGREE OF DOCTOR OF PHILOSOPHY

Structure evolution of phase-separated EC/HPC films for controlled drug release

PIERRE CARMONA

Department of Physics
CHALMERS UNIVERSITY OF TECHNOLOGY
Gothenburg, Sweden 2022

Structure evolution of phase-separated EC/HPC films for controlled drug release
PIERRE CARMONA
ISBN: 978-91-7905-727-5

Doktorsavhandlingar vid Chalmers tekniska högskola
Ny serie nr 5193
ISSN 0346-718X

pierre.carmona@ri.se
Division of Bioeconomy and Health
Department of Agriculture and Food
Unit of Product Design
RISE Research Institutes of Sweden | ri.se
Frans Perssons väg 6 | Box 5401, SE-402 29, Gothenburg, Sweden

pierre.carmona@chalmers.se
Department of Physics
Division Nano- and Biophysics
Eva Olsson Group
CHALMERS University of Technology | chalmers.se
Fysikgränd 3 | 412 96, Gothenburg, Sweden

Cover: Schematic illustration of a controlled drug release system made of porous ethylcellulose/hydroxypropylcellulose (EC/HPC) films. The different parts of the system are displayed following the line from the top left to bottom right. First, the sick patient swallows a pellet that contains the drug (in pink). The pellet is coated with a phase-separated EC/HPC film (EC is blue, and HPC is yellow). Then, an example of the phase-separated pellet film structure is shown. The film structure was imaged using Confocal Laser Scanning Microscopy (CLSM). In the next step, when the phase-separated film comes into contact with the body fluids (here marked as H_2O), the water-soluble HPC leaches out, revealing a porous structure. Subsequently, a Scanning Electron Microscopy (SEM) micrograph shows an example of the porous phase-separated film structure. Finally, the drug is then delivered in a controlled manner through the porous film. At the top right, an example of a 3D structure of an EC/HPC multilayer film used for controlled delivery is shown. The 3D structure was obtained with CLSM.

Printed by:
Chalmers Reproservice
Gothenburg, Sweden 2022

Structure evolution of phase-separated EC/HPC films for controlled drug release

Pierre Carmona
Division Bioeconomy and Health, RISE Research Institutes of Sweden
Department of Physics, Chalmers University of Technology

ABSTRACT

Porous phase-separated ethylcellulose/hydroxypropylcellulose (EC/HPC) films are used to control drug transport out of pharmaceutical pellets. The drug transport rate is determined by the structure of the porous films that are formed as the water-soluble HPC leaches out. In industry, the pellets are being coated using a fluidized bed spraying device, and layered films with varying porosity and structure are obtained. A detailed understanding of the formation mechanisms of the multilayered phase-separated structure during production is lacking. Here, we have investigated EC/HPC films produced by spin-coating, which mimics the industrial manufacturing process in a reproducible and well-controlled manner. This work is aimed to understand why the film structure is layered, and why it exhibits different porosities and structures by understanding the film formation mechanisms. The 2D and 3D structures of the EC/HPC films were characterized using confocal laser scanning microscopy (CLSM), scanning electron microscopy (SEM), focused ion beam SEM (FIB-SEM) and image analysis. The thickness of the films was measured by profilometry.

To be able to understand the multilayer formation, we first studied the structure evolution in EC/HPC monolayer films. The effect of the EC/HPC ratio (from 15 to 85 wt% HPC) on the in-plane and cross-sectional structure evolution was determined. Bicontinuous structures were found for 30 to 40 wt% HPC and discontinuous structures were found for the fractions 15 to 22 and 45 to 85 wt% HPC. The growth of the characteristic length scale followed a power law, $L(t) \sim t^n$, with $n \sim 1$ for bicontinuous structures, and $n \sim 0.45$ - 0.75 for discontinuous structures. An image analysis method to characterize the time-dependent 2D curvature evolution was developed. Two main coarsening mechanisms could be identified: interfacial tension-driven hydrodynamic growth for bicontinuous structures and diffusion-driven coalescence for discontinuous structures. The cross-sectional structure evolution shows that during shrinkage of the film, the phase-separated structure undergoes a transition from 3D to nearly 2D structure evolution along the surface. The shrinkage rate was found to be independent of the EC/HPC ratio. A new method to estimate part of the binodal curve in the ternary phase diagram for EC/HPC in ethanol has been developed. For multilayer films, the results showed that the inherent behaviour of the monolayer films have a strong impact on the formation of each new layer in multilayer films. A gradient in structure size with larger structures close to the substrate and smaller structures close to the air surface was found and explained by the redissolution of the layers already deposited during previous deposition cycles. By varying the EC/HPC ratio during the multilayer film production, we showed *in situ* that the layers do not mix. By varying the spin speed every other layer, we produced a layered film exhibiting varying porosity, proposing a possible explanation for obtaining a layered coating in the industrial process. The findings of this work provide a good understanding of the mechanisms responsible for the morphology development and enable tailoring of multilayer EC/HPC films structure for controlled drug release.

Keywords: biopolymer, cellulose, coarsening, confocal laser scanning microscope, controlled drug release, drug release, electron microscopy, phase separation kinetics, phase separation mechanisms, porous film, spin-coating.

PREFACE

The research presented in this work was carried out at the Department of Agriculture and Food, RISE Research Institutes of Sweden, Gothenburg, Sweden during the period October 2018 – October 2022. Main supervisor was Adj. Prof. Niklas Lorén, RISE, and assistant supervisors were Adj. Asst. Prof. Magnus Röding, RISE, and Prof. Aila Särkkä, Department of Mathematical Sciences, Chalmers University of Technology and Gothenburg University. Examiner was Prof. Eva Olsson, Department of Physics, Chalmers University of Technology. The research was done in collaboration with the Eva Olsson group, Department of Physics, Chalmers University of Technology and Dr. Christian von Corswant, AstraZeneca.

The work was funded by the Swedish Foundation of Strategic Research. The project was also supported by AstraZeneca.

List of publications included in the thesis

Paper I.	*Structure evolution during phase separation in spin-coated ethylcellulose/hydroxypropylcellulose films*. **P. Carmona,** M. Röding, A. Särkkä, C. von Corswant, E. Olsson and N. Lorén Published in Soft Matter (March 2021); Vol. 17 Pages 3913-3922 DOI: 10.1039/d1sm00044f
Paper II.	*Structure formation and coarsening kinetics of phase-separated spin-coated ethylcellulose/hydroxypropylcellulose films* **P. Carmona,** M. Röding, A. Särkkä, C. von Corswant, E. Olsson and N. Lorén Published in Soft Matter (March 2022) Vol. 18 Pages 3206–3217 DOI: 10.1039/d2sm00113f
Paper III.	*Cross-sectional structure evolution of phase-separated spin-coated ethylcellulose/hydroxypropylcellulose films during solvent quenching* **P. Carmona,** C. von Corswant, M. Röding, A. Särkkä, E. Olsson and N. Lorén Published in RSC Advances (September 2022) Vol. 20 Pages 26078-26089 DOI: 10.1039/d2ra04178b
Paper IV.	*Controlling the structure of spin-coated multilayer ethycellulose/hydroxypropylcellulose films for drug release* **P. Carmona,** T. Nilsson Pingel, J. Poulsen, J. Westergren, M. Röding, E. Lambrechts, H. de Keersmaecker, K. Brackmans, A. Särkkä, C. von Corswant, E. Olsson and N. Lorén Manuscript

List of publications not included in the thesis

Paper V.	*Glyceraldehyde as an Efficient Chemical Crosslinker Agent for the Formation of Chitosan Hydrogels* **P. Carmona,** A. M. Tasici, S. A. Sande, K. D. Knudsen and B. Nyström Published in Gels (October 2021) Vol. 7 Issue DOI: 10.3390/gels7040186
Conference Paper I.	*Simultaneous improvement of surface finish and bonding of centrifugal microfluidic devices in cyclo-olefin polymers* E. Vereshchagina, **P. Carmona**, E. Andreassen, J. Batalden, M. Plassen and M. M. Mielnik 2018 IEEE Micro Electro Mechanical Systems (MEMS) 21-25 Jan. 2018 Pages: 1257-1260 DOI: 10.1109/memsys.2018.8346792
Conference Paper II.	*Structure of spin-coated phase-separated thin polymer films* **P. Carmona,** M. Röding, A. Särkkä, C. von Corswant, E. Olsson and N. Lorén European Microscopy Congress 2020 March 2021 DOI:10.22443/rms.emc2020.97

Contribution Report

Paper I, II, III and Conference Paper II: Planned and performed the experimental work; carried out the calculations; image analysis and discussion with co-authors; wrote the original draft; reviewed and edited the paper together with the co-authors.

Paper IV: Planned and performed most of the experimental work; carried out the calculations; image analysis and discussion with co-authors; wrote the original daft; reviewed and edited the paper together with the co-authors. Part of the experimental work was performed by a master thesis student that I supervised (Eileen Lambrechts from Ghent University). FIB-SEM experiments were performed together with Dr. Torben Nilsson Pingel from RISE.

ACKNOWLEDGEMENTS

A PhD journey is certainly a challenge, and impossible to perform alone. I would like to thank all the people from close and far away, that participated in making this journey a success.
To begin with, I would like to acknowledge the Swedish Foundation for Strategic Research (SSF), for funding my fun and exciting PhD project, and AstraZeneca for the financial support.

I would like to express my sincere gratitude to my main supervisor, Niklas Lorén, RISE, for the continuous support in my PhD study and related research, for your never-ending optimism, motivation, your passion for science, and all your "crazy ideas". Your guidance helped me throughout my whole PhD journey.
To my co-supervisors, Magnus Röding, RISE, and Aila Särkkä, Chalmers. Magnus for the support, your feedback, and for the many hours spent together writing in MATLAB, it is another language that I could not have been able to master without you. Aila for your kind support and thorough feedback.
I want to thank my examiner, Eva Olsson, Chalmers, for the warm welcome in the Eva Olsson group, for being an inspiration, for your honesty, and for the continuous support.
Thanks to Christian von Corswant, AstraZeneca, for the support, all your ideas, the fruitful discussions and your deep knowledge on the EC/HPC system.

My sincere thanks also to all RISE team, and especially the whole Product Design unit for the support, the conviviality, and the funny talk during coffee and lunch break. Lina, for the warm and continuous support as manager. Annika A. for teaching me how to use my dear confocal microscope. Special thanks to Ana, my roomie, for your support, the friendship, and hours of laughter. But also, Loredana, Patricia, Nodas, Mihaela, Johanna, Astrid, Lisa-Maria, Claudia, Jun, Patrik, Annika K., Mats, Camilla, Emil, Sophia, Evelina, Torben, Annika K, Åsa, Tim, Erik, Hannah and Leyla.

I want to thank the whole Eva Olsson group, my fellow colleagues, for the conviviality, laughter and the exiting talks during our group meetings: Cecilia F., Gustav, Jonathan, Andy, Lunjie, Shun, Rebecka, Alok, Maria and Melike.

I am thankful to CMAL (Chalmers Materials Analysis Laboratory), to Ludvig de Knoop, and Stefan Gustafsson for sharing your skills and teaching me electron microscopy.
I give my regards to Tobias Gebäck and Sandra Barman from the Mathematical Department of Chalmers, for interesting discussion and collaboration on phase separation simulation and 3D data visualization.
I thank Jens Poulsen and Jan Westergren from Wendelsbergs beräkningskemi for the fruitful collaboration on simulation of EC/HPC multilayer films.
Christian Müller and Sandra Hutmark from the Department of Chemistry of Chalmers are acknowledged for access to lab facilities (spin coater and profilometer), for help and useful advice.

To all my friends from Sweden, thanks for always being present. My thanks go to Cecilia B., Zach, James, Yasmin, Adam, Zandy, Emma, Athena-Morgane, Kengo, Ida-Brita, Govin and Pavlina. Cecilia B. thank you for bringing so much joy in my life, for your wonderful energy, constant support, and our laughter.
Les amis pour toujours : Kim, Croustine, Louis, Cécile, Katz, Zucchi, Nina, Laura, Emma, Nono et Constance. Merci, merci, d'avoir été là pour moi, me convaincre de continuer, de m'avoir aidé à avancer dans la thèse, mais aussi dans la vie.

Last but not the least, I am deeply grateful to my family for the support and the encouragement during all those years, special thanks to my parents and my twin brother Julien. Papa et Maman merci pour votre soutien et votre amour. Papa pour les nombreuses heures passées à m'enseigner les maths, pour t'être levé avec moi tous les matins d'école pendant 20 ans. Maman pour absolument tout, pour toujours avoir les mots. Merci à mes oncles et tantes, aux cousins, Thomas, Charlotte, Camille. Un grand merci à Brigitte ma grand-mère pour son amour et son soutien constant. Enfin, une pensée émue pour mes grands-parents, Jacques et Maryse, merci pour tout.

LIST OF ABBREVIATIONS AND ACRONYMS

2D	Two dimensions
3D	Three dimensions
CLSM	Confocal Laser Scanning Microscopy
EC	Ethylcellulose
FFT	Fast-Fourier Transform
FIB	Focused Ion Beam
FOV	Field Of View
$h(t)$	Film thickness at time t
HPC	Hydroxypropylcellulose
$L(t)$	Characteristic length scale at time t
$(m \pm sd)$	Mean plus/minus standard deviation
Mw	Molecular weight
nb_r	Number of replicates
NG	Nucleation and Growth
PCT	Percolation to Cluster Transition
SEM	Scanning Electron Microscope
SD	Spinodal Decomposition
wt%	Weight percentage

TABLE OF CONTENTS

1 Introduction

Controlled drug release formulations are used to deliver drugs at predetermined rates and periods of time in the body to optimize the efficiency of the drug and to minimize side effects. For the last decades, solid oral dosage forms have been the most popular way of drug administration (Gupta *et al.*, 2009). One way to obtain the desired release is to use a controlled release formulation in form of a pellet, containing a drug reservoir coated with a film, that becomes porous in contact with body liquids. Ethylcellulose (EC) and hydroxypropylcellulose (HPC) are two cellulose derivatives with established use in the pharmaceutical industry (Sakellariou and Rowe, 1995). Figure 1.1 is showing the formation of an EC/HPC film for drug release. Mixed with a common solvent *e.g.* ethanol, EC and HPC form a one-phase polymer solution at low polymer concentration. During solvent evaporation (see Figure 1.1), phase separation occurs, and subsequently a dry film is produced. EC is water-insoluble and HPC is water-soluble, and in contact with water the dissolution and leakage of the water-soluble HPC leads to the formation of a porous EC matrix through which the drug flows or diffuses. The porous microstructure of the pellet coating controls the mass transport of the drug from the core to the surrounding liquid in the stomach or intestine. By controlling the manufacturing and the formulation, and therefore the coating structure, the drug release rate can be controlled (Tiwari *et al.*, 2012). Coatings made of porous phase-separated films were shown to be very effective in controlling mass transport (Marucci *et al.*, 2011) but the kinetics and mechanisms of structure formation in such films are not fully understood.

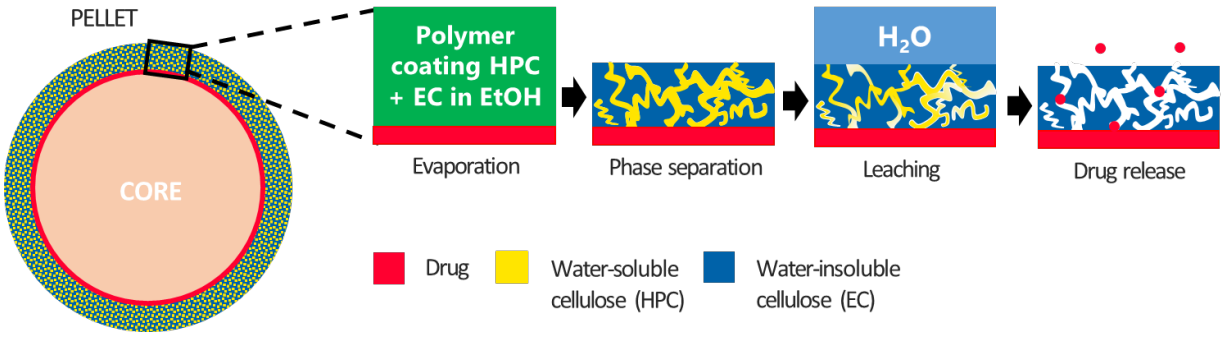

Figure 1.1 *Formation of porous film made of EC and HPC for the delivery of drugs. From left to right, the different steps: evaporation of ethanol, phase separation and kinetic trapping, leaching of HPC and the release of the drug.*

The 3D structure determines the transport through the porous network in phase-separated systems (Wassén *et al.*, 2014, Gebäck *et al.*, 2015). By controlling the process of phase separation, the film structure, and hence the mass transport can be tailored. The 3D structure porosity, pore size distribution, pore shape and connectivity of EC/HPC films in pellets have been determined using focused ion beam scanning electron microscopy (FIB-SEM) and advanced image analysis (Fager, 2020, Fager *et al.*, 2020a, Fager *et al.*, 2020b, Röding *et al.*, 2021, Fager *et al.*, 2021a, Fager *et al.*, 2021b, Barman, 2020). The method allowed identification of central features of the porous network by quantification of channels where pore paths coincide. It was found that the interconnectivity and porosity increase with increasing amount of HPC. In films made with spraying and a rotating drum, the effect of the molecular

weight of EC and HPC on the microstructure (Andersson *et al.*, 2009, Andersson *et al.*, 2011, Andersson *et al.*, 2013, Andersson, 2015, Andersson *et al.*, 2016) and interactions of the film with water and its influence on permeability of both water and drug during leaching have also been investigated (Jansson *et al.*, 2014).

The coating of the EC/HPC films is nowadays made batch-wise in a fluidized bed spraying device to coat drug-containing pellets. One challenge is to relate the final properties of the polymer coating to the parameters of the industrial process used during production of coated pellets. During spraying, small droplets containing EC, HPC and ethanol are hitting the pellets, interacting with the already present film, and coating the pellets, which influences the structure evolution of the phase-separated EC/HPC film. Many mechanisms are involved in the formation of the phase-separated films on the pellets, and they are competing in a complex and time-dependent manner. Examples of involved mechanisms are phase separation, kinetic trapping by viscosity increase, solvent evaporation, solvent quench, wetting, redissolution, and mixing. This research focuses on understanding how all these mechanisms interact during the film structure evolution and how the composition of the polymer mixture and the manufacturing process influence the final film structure.

2 Aim of the thesis and thesis outline

2.1 Purpose and goals

The purpose of this work was to obtain a mechanistic understanding of the structure evolution of phase-separated films and to increase the quality and robustness in the tailoring of thin EC/HPC film for pharmaceutical applications.

Specific goals were to:

- Find a method to mimic the industrial process of fluidized bed spraying device and film formation of multilayered structures in a controlled lab environment (**Paper I** and **Paper IV**).
- Develop an experimental set-up which allows observation *in situ* of the structure evolution and structure formation in monolayer (**Paper II** and **Paper III)** and multilayer (**Paper IV**) films.
- Understand the different mechanisms of phase separation and coarsening that influence the structure evolution in a competing manner (**Paper II, Paper III**, and **Paper IV**).
- Determine the kinetics of phase separation during solvent quenching (**Paper II** and **Paper III**) and relate it to the phase diagram (**Paper III**).
- Investigate the effect of the EC/HPC ratio and the spin-coating parameters on the structure evolution and the final film structure (**Paper I-IV**).
- Understand the origin of the layered structure in the film on industrial pellets (**Paper IV**).

2.2 Thesis outline

The thesis is structured as follows. In the background section, the pharmaceutical applications, the phase separation theories and the EC/HPC system are introduced. In the experimental section, an overview of the materials and methods used in the thesis work is given. In the results section, we first introduce spin-coating as a model to mimic the industrial fluidized bed spraying device, then we study the structure evolution *in situ* in a monolayer. Finally, we investigate the effects of the EC/HPC ratio and spin-coating parameters on the monolayer and multilayer film structures.

3 Background

In this section, the background and context of the research are established. First, the drug delivery systems and the use of phase separation to make controlled drug release formulations are introduced. Second, an overview of phase separation mechanisms and coarsening in polymer mixtures is provided. Then, information about the biopolymers we use in this thesis, namely the two cellulose derivatives ethylcellulose (EC) and hydroxypropylcellulose (HPC), is given. Finally, we describe the industrial process of making drug delivery systems using phase-separated EC/HPC films and discuss the challenges of mimicking such a process.

3.1 Controlled drug release in pharmaceutics

Drug delivery systems, referring to the ensemble of technologies for transporting a drug into the body to achieve a targeted therapeutic effect, have been used worldwide for decades to deliver pharmaceutics (Rhodes and Porter, 1998). Figure 3.1 summarizes the main objectives and features of a drug delivery system. The main aim of a drug delivery system is to obtain an optimal treatment at the right location in the body at correct time (Klein, 2002) using a combination of active pharmaceutical ingredient (API) and release rate system. The delivery rate is critical, because the drug concentration in the blood must be within a certain interval, called the therapeutic window. If the concentration is too low, the drug has no effect and if it is too high the drug can cause side effects and be poisonous (Jong, 2008). The location where the drug is released is also crucial for the functionality of the drug. In the case of oral dosage, the drug needs to be released in a particular zone in the gastrointestinal tract. The pH value varies between 1 and 5.5 in the upper part (stomach, upper intestine) and between 5.5 and 7 in the lower part (lower intestine, colon) (Rawlings and Lucas, 1985). Therefore, the pH must be considered when selecting materials for the delivery system. Other challenges when formulating a drug release system are the reduction of the amount of drug needed and the reduction of side effects (Hutton and Morris, 1992, Edsbäcker *et al.*, 2003).

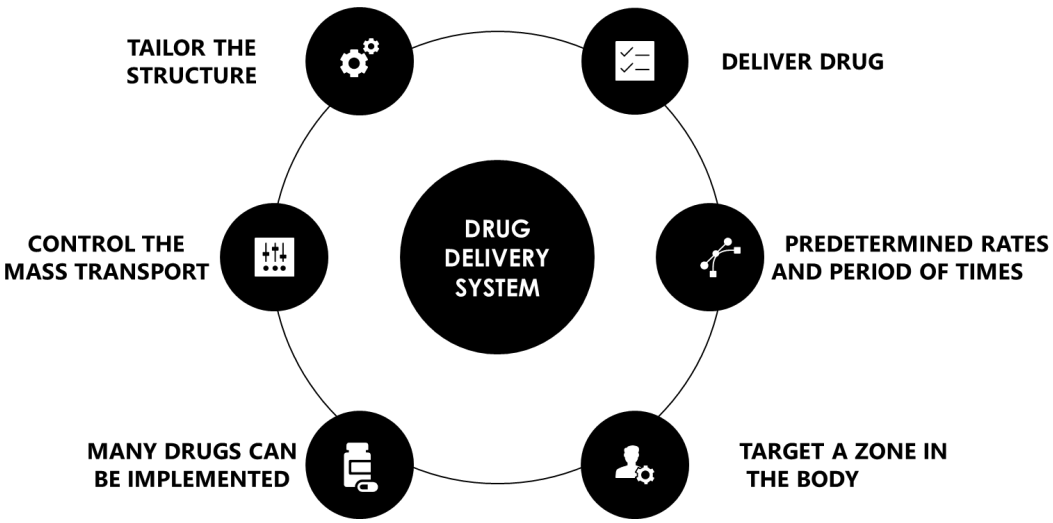

Figure 3.1 *Drug delivery system objectives.*

Conventional formulations, also called immediate release systems, give a rapid release of the drug, and can be obtained by several systems such as capsules, tablets, and pellets. Such formulations are used where diseases or infections need acute drug delivery. However, when the release of the drug needs to be maintained over a longer period of time and the delivery rate needs to be precise, controlled release formulations are used (Huynh and Lee, 2015). Figure 3.2 shows the drug level in the blood for the two release systems, conventional release and controlled release. In theory, the desired drug concentration (grey area representing the therapeutic window) can be obtained with both release systems. Conventional release can last if multiple doses are taken (blue dashed curve). However, the controlled release (red curve) is more stable and fewer doses are needed.

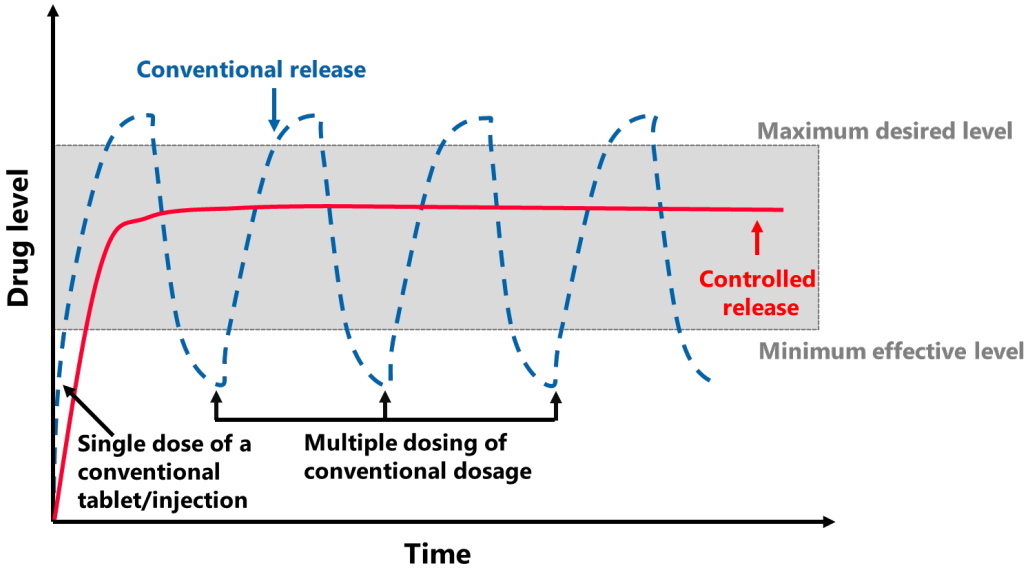

Figure 3.2 *Drug levels in the blood released from a traditional release system, a combination of multiple oral capsules or injection dosing (blue dashed curve) and a controlled release system (red continuous curve). Adapted from Huynh and Lee (2015).*

Soft materials and in particular polymers are often used for drug formulations. Both synthetic and natural polymers are used (Langer and Peppas, 2003, Fredenberg *et al.*, 2011). Natural polymers are highly accessible due to the huge number of sources and exhibit high affinity to biological tissue while synthetic polymers need to be synthetized. However, the synthesis offers good control, and the properties can be more easily tuned. Cellulose derivatives are an example of natural polymers that can be used for drug formulations. Like other polysaccharides they offer wide a range of possible chemical modifications and therefore modifications a large range of material properties (Sakellariou and Rowe, 1995, Langer and Peppas, 2003).

For controlled release formulations two main approaches exist, shown in Figure 3.3: the reservoir controlled release system where a coating encapsulates the drug, see Figure 3.3a, and the matrix controlled system where the drug is dispersed in the matrix, see Figure 3.3b (Langer and Peppas, 1983, Sershen and West, 2002). Compared to the reservoir system, the matrix system is not enveloped within a delivery rate limiting membrane. As such, the release rate of the drug from the matrix system is usually not constant and decreases in time. The most

common matrix-based formulations use polymers which erode or dissolve with time as shown in Figure 3.3b. The mechanisms of release for both approaches are mainly diffusion, dissolution, osmotic pumping and swelling (Sakellariou and Rowe, 1995, Langer and Peppas, 1983, Uhrich *et al.*, 1999). In the case of EC/HPC phase-separated film coating, the system is a reservoir-controlled release, and the main release mechanism is diffusion. The water-soluble polymer in the coating is leached out, forming a porous transport path through which the drug diffuses (see Figure 1.1).

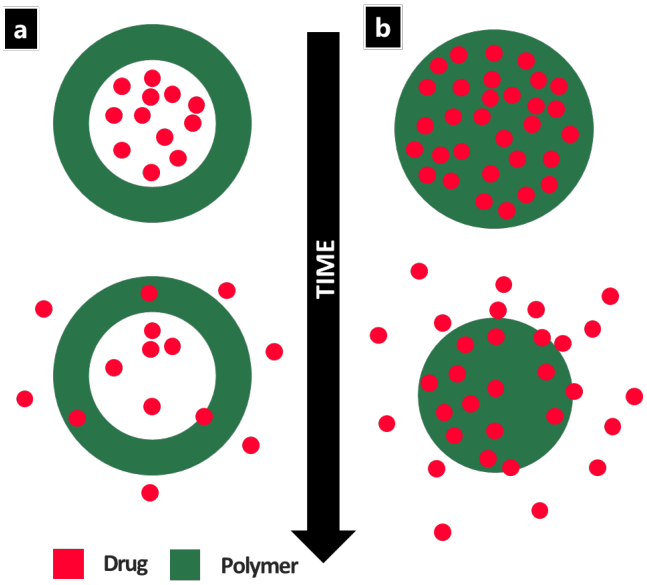

Figure 3.3 *Schematic illustration of controlled release formulations systems, with a) a reservoir-controlled release system, and b) a matrix-controlled system. Adapted from Stewart et al. (2018).*

3.2 Phase separation in polymer mixtures

Phase separation is a general phenomenon of many polymer mixtures (Piculell *et al.*, 1995). By controlling the phase separation process, properties of high-performance polymer can be tuned. It allows changes of material characteristics, often leading to an improvement with respect to *e.g.* rigidity, toughness, chemical resistance, or abrasion. Phase separation can be initiated by a change in temperature (Jin *et al.*, 2015). It can also be triggered by evaporation and drying (removal of solvent) (Schaefer *et al.*, 2016, Petersson, 2005), polymerization, by change of pH or salt concentration (Firoozmand *et al.*, 2012) and by gelation and conformational ordering (Lorén *et al.*, 2001).

In polymer mixtures, phase separation is used mainly in separation and purification procedures within the manufacturing of films, fibers, membranes, and foams. In the pharmaceutical field, phase-separated polymer films are very effective in controlling the mass transport of drugs (Sakellariou and Rowe, 1995). Phase separation is also very common in food science (Scholten *et al.*, 2004b, Lorén *et al.*, 2001, Tanaka, 2012, Zhou *et al.*, 2014, Li *et al.*, 2016). For example, phase-separated polymer mixtures can be used as fat replacement materials to control texture and consistency in food products (Clark, 1995). Furthermore depletion-induced phase

separation and gelation of xanthan and casein mixtures allow for controlling the stability, the microstructure and the mechanical properties (Mezzenga *et al.*, 2005). Also, viscoelastic phase separation in food caused by incompatibility and viscoelastic forces is used to control texture and stability of products (Tanaka, 2012). This type of phase separation occurs for instance in mixtures composed of *e.g.* globular protein, bovine serum albumin and an anionic polysaccharide, low-methoxyl pectin (Donato *et al.*, 2005). Phase separation in emulsions is also an important aspect in food science to form water/water/oil systems. For example, sodium caseinate is used as an emulsifying agent in dairy products or soy protein systems (Renkema, 2004).

3.2.1 The Gibbs free energy of mixing

Whether two polymers are mutually miscible depends on the shape of the Gibbs free energy of the mixing curve (Gibbs, 1961, Jones and Richards, 1999). The system reaches a state of minimum free energy at equilibrium. Gibbs free energy (G) is a measure of the maximum available work that can be derived from any system under conditions of constant temperature (T) and pressure (P) and is an important thermodynamic quantity. The changes in Gibbs free energy is defined as $\Delta G = \Delta H - T\Delta S$, where ΔS is the change in entropy and ΔH is the change in enthalpy. The partial molar Gibbs free energy of mixing with respect to the solvent for the formation of a polymer solution is given by the following equation, according to the Flory-Huggins theory (Flory, 1942).

$$\Delta_{mix}G = RT[\varphi_1 \ln \varphi_1 + \varphi_2 \ln \varphi_2 + \chi \varphi_1 \varphi_2]$$

where φ_i is the volume fraction of the component *i*, *i=1,2*, χ is the Flory-Huggins binary interaction parameter, R is the universal gas constant, and T is the absolute temperature. The first two terms inside the bracket of the right-hand side in the equation above, are related to the entropy of mixing, and the third term is related to the enthalpy of mixing.

3.2.2 Phase diagrams of polymer mixtures

3.2.2.1 Phase diagram at constant temperature

Phase diagrams are useful for describing the status of a polymer mixture. Figure 3.4 shows the different behavioral regions for a typical polymer/polymer/solvent mixture at constant temperature (Tolstoguzov, 2003a, Tolstoguzov, 2003b).

The binodal curve represents the transition from the one phase region (region 1) to the two-phase region (regions 2, 3 and 4). In Figure 3.4, going from region 1 to regions 2 and 3 occurs through nucleation and growth (NG); going from region 1 to region 4 occurs through spinodal decomposition (SD) (refer to section "3.2.3 Mechanisms of phase separation"). Regions 2 and 3 represent the meta-stable regions and region 4 represents the unstable region. The boundary between the unstable and the meta-stable regions is the spinodal curve. When phase separation occurs, the process does not stop before the compositions in each phase have reached their equilibrium concentrations in the different phases. These compositions are located along the binodal curve. They are connected through the tie line that passes through the original

composition and the equilibrium compositions of each phase in the phase diagram. Note that for entropic reasons, even after reaching equilibrium, the concentrations in the different phases will never be 100% of any of the components.

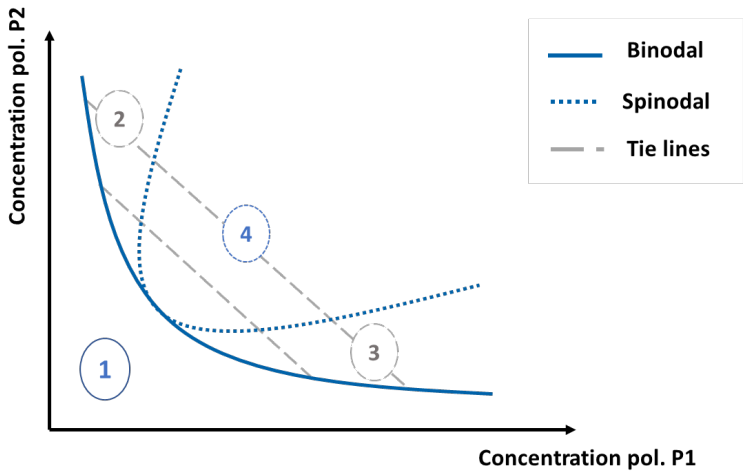

Figure 3.4 *Schematic phase diagram of solvent/ polymer/polymer system. Regions: 1, one-phase region; from 2 to 4, phase-separated morphologies. Adapted from Tolstoguzov (2003b).*

Figure 3.5 shows a typical ternary phase diagram, used to describe a ternary system consisting of two polymers and a solvent. In the diagrams, two regions are described: the one-phase region where the mixture is one homogeneous phase and the two-phase region where the mixture is separated into two distinct phases. Depending on the types of interactions that occur between the polymers in solution, an associative or a segregative phase separation can occur (Piculell *et al.*, 1995). During associative phase separation (Figure 3.5a), both polymers are enriched in one phase and depleted in the other phase. During segregative phase separation (Figure 3.5b), each phase is enriched in one of the polymers. Solvent partitioning is taking place when the polymer A or B has stronger affinity with the solvent, in this case the solvent will not be equally distributed between the phases enriched in polymer A or B. The type of assembly of the components in the system is governed by the free energy of mixing (Jones and Richards, 1999) (refer to previous section 3.2.1).

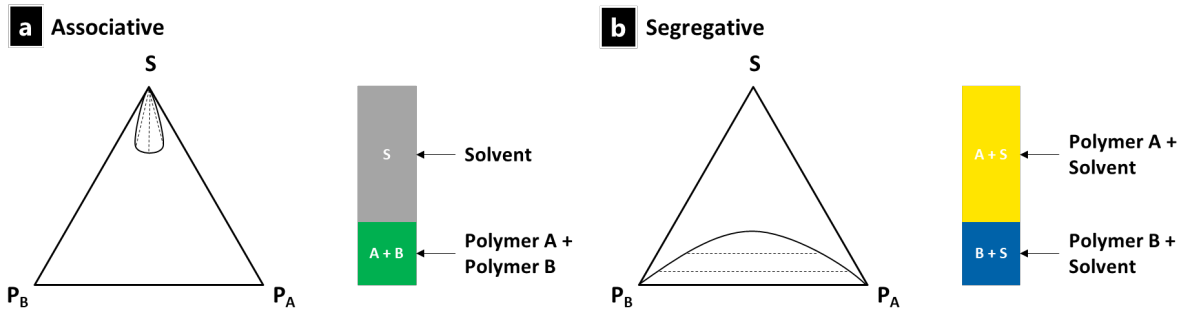

Figure 3.5 *Ternary phase diagram with a) associative phase separation and b) segregative phase separation.*

3.2.2.2 Phase diagram at varying temperature

Temperature and composition are two key parameters influencing incompatibility. Figure 3.6 shows a phase diagram of a ternary polymer mixture composed of two polymers in a solvent, (Clark, 1995) with the temperature *versus* the composition of polymer A ($x_A = 1 - x_B$), where x_i is the composition of the polymer i. In the diagram, the separation between the one-phase and two-phase regions is represented by the binodal curve whereas the spinodal separates the metastable region from the unstable region within the two-phase region. The binodal and the spinodal coincide in only one point: the critical point (composition x_{cr} and temperature T_{cr}).

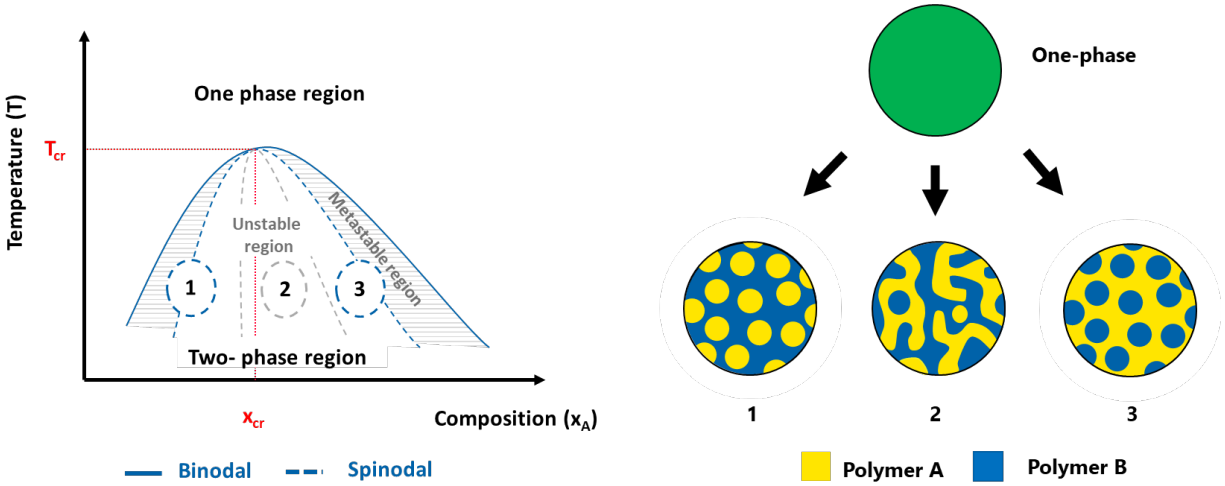

Figure 3.6 *Schematic phase diagram of a ternary polymer mixture composed of two polymers and a solvent. To the left, regions 1,2,3 represent possible mechanisms of phase separation. To the right, the corresponding morphologies 1,2,3. The composition x_{cr} and temperature T_{cr} (in red) correspond to the critical point.*

In Figure 3.6, compositions inside the meta-stable region, separate according to the nucleation and growth (NG) mechanism, whereas those within the unstable region separate through the spinodal decomposition (SD) mechanism. Morphologies 1 and 3 are droplet-like structures mainly initiated by the NG mechanism. Morphology 2 is an interconnected structure obtained through SD (see section "3.2.3Mechanisms of phase separation" for the explanation about NG and SD).

However, temperature and pressure are influencing the phase behavior of ternary mixtures. For example, temperature is not described in the ternary diagram shown in Figure 3.5. Figure 3.7 is an example of a phase diagram describing a ternary system for varying temperature. To describe the spinodal and the binodal in ternary systems composed of two polymers and a solvent, a three-dimensional ternary phase diagram can be used. In this case, the binodal and the spinodal regions are represented with planes (Figure 3.7). Some systems exhibit a UCST behavior (upper critical solution temperature) and some an LCST behavior (lower critical solution temperature) (Clark and Lipson, 2012, Ougizawa and Inoue, 1986). Eventually, the binodal becomes a circle and then a point, and thus there is an upper temperature limit (UCST).

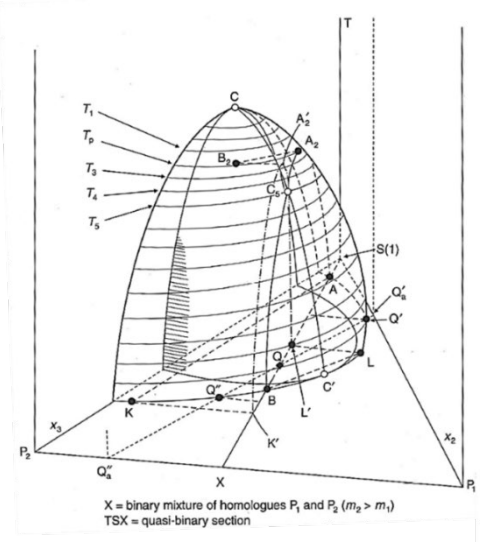

Figure 3.7 *Illustration of the binodal and spinodal region in a ternary system at constant pressure. The spinodal plane is partly hatched (Koningsveld et al., 2001).*

3.2.3 Mechanisms of phase separation

There are two main phase separation mechanisms in polymer mixtures: nucleation and growth (NG) and spinodal decomposition (SD). The binary phase diagram in Figure 3.6 shows, for instance, at which composition the mixture has been separated through either mechanism: the compositions within the metastable region separate according to the NG mechanism while the compositions within the unstable region separate trough the SD mechanism. During SD the system can undergo percolation to cluster transition (PCT). And more generally a secondary phase separation can take place.

3.2.3.1 Nucleation and growth

The mechanism nucleation and growth describes the formation of a heterogeneous structure from a homogenous structure, initiated by a nuclei (Gibbs, 1961). In the phase diagram, when the polymer mixture ends up in the metastable region, the NG will appear (Das, 2014). Figure 3.8 shows the different steps of a general case of NG: step I) the concentration increases up to a certain level denominated by C_{nuc} in Figure 3.8 ; step II) a nuclei is formed; step III) the growth takes place at the surface of the nuclei until reaching the equilibrium concentration C_{eq}.

During polymer phase separation, NG can be associated with the formation of irregular sized droplets that grow bigger as a function of time. In addition, the occurrence of the droplets is distributed in time (Sagui and Grant, 1999, Debenedetti, 2000). Most often NG occurs through a heterogeneous mechanism: when foreign particles act as nucleating agents and induce the phase separation, the growth is taking place by addition of constituents from the bulk. More rarely, homogenous NG can occur, where droplets are formed by concentration fluctuations that overcome the energy barrier and reach the equilibrium state (C_{eq}, in Figure 3.8) in which they remain. For a polymer mixture, the NG-type phase separation leads to a droplet-like structure (Tanaka and Nishi, 1985) (see morphologies 1 and 3 in Figure 3.6).

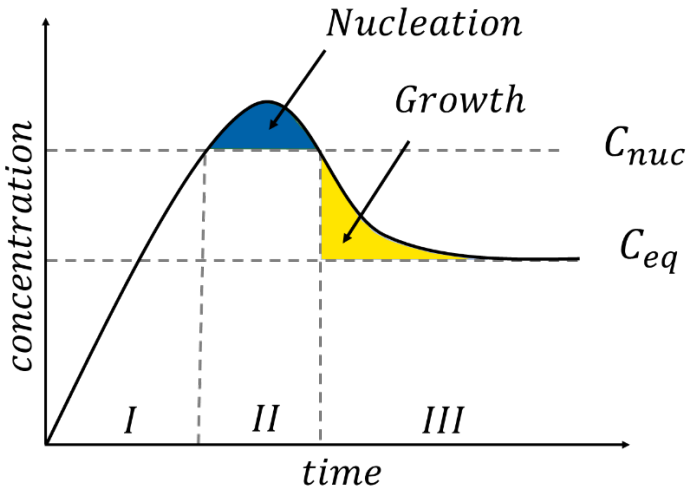

Figure 3.8 *Homogeneous nucleation and growth mechanism. C_{nuc} is the minimal concentration for nucleation. C_{eq} is the concentration at equilibrium. Adapted from Ottesen (2011).*

3.2.3.2 Spinodal decomposition

Spinodal decomposition is a mechanism for rapid unmixing of a mixture of liquids from one compatible phase to two coexisting phases. SD is characterized by a periodicity in the domain formation, or equivalently as having a characteristic length scale L(t) (see Figure 3.9d). In general, SD is initiated by small fluctuations in concentration within the blend, reducing the free energy of mixing (Jones and Richards, 1999).

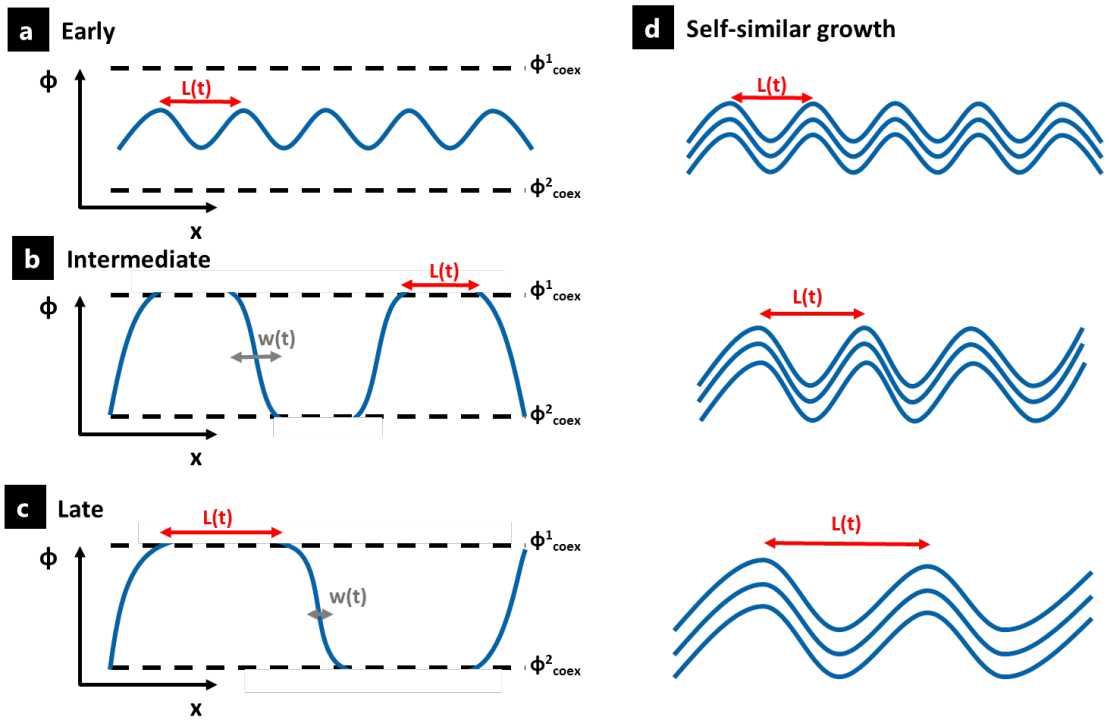

Figure 3.9 *Time-dependent structural evolution of the length scale as a function of time through the a) early, b) intermediate, and c) late stages of the spinodal decomposition mechanism. In d), an illustration of self-similar growth during spinodal composition is shown. Adapted from Hashimoto (1988).*

Figure 3.9 shows the successive steps of SD. Initially an interconnected structure will be formed, then the SD goes through three stages: an early stage (see Figure 3.9 a), an intermediate stage (see Figure 3.9b), and a late stage (see Figure 3.9c). In the early stage, the concentration fluctuations are present at different length scales and therefore grow at different rates (Hashimoto, 1988). The length scale selection mechanism (Cahn, 1965) makes the concentration fluctuations with an intermediate length scale predominate. Fluctuations with short length scales exhibit a sharp concentration of gradients which make them energetically not preferable. Fluctuations with long length scales involve diffusion over large distances, which is relatively slow. The structure with length scales $L(t)$ and interfacial width $w(t)$ evolve through the SD process. At the early stage, $L(t)$ and $w(t)$ remain constant, only the amplitude increases. In the intermediate stage, the amplitude reaches its maximum (the maximum corresponds to the equilibrium concentration, ϕ_{coex} in Figure 3.9), the length scale $L(t)$ increases while the interfacial width $w(t)$ starts to decrease towards the equilibrium. During the late stage of SD the entire system is brought to equilibrium, $w(t \to \infty) = w_{eq}$ and the system evolves solely by self-similar growth (Binder and Stauffer, 1974).

3.2.3.3 Percolation-to-cluster transition

With spinodal decomposition in bulk, the system first evolves to a bicontinuous structure, and then the structure either continue to develop as a bicontinuous structure, where the polymer phases are interconnected, or it develops to a discontinuous morphology via a percolation-to-cluster-transition (PCT), where droplets of one polymer are distributed in the other continuous polymer phase, depending on the phase volume. For the discontinuous morphology, the droplets appear at the same time during the structure evolution and have similar sizes. In critical and near-critical mixtures (which correspond to a specific concentration interval), each phase keeps percolation. However, in off-critical mixtures as phase separation proceeds the minority phase cannot keep the percolation and the system undergoes PCT (Takeno *et al.*, 1999). After this transition the system cannot minimize its surface energy anymore by surface diffusion and shift to cluster (Lauger *et al.*, 1994). Several steps can be identified: first, the percolating morphology is broken into grains of partly branched substructures producing a broad cluster distribution. Second, when all percolation paths have been destroyed the structure cuts its strands and a structure with inclusions is formed. Finally, after the PCT, the structure can continue to grow.

3.2.3.4 Secondary phase separation

During phase separation a first quench brings the phase separation to coarsen and reach a certain length scale. A second quench, or a continuation of the first quench, can lead to a secondary phase separation. The secondary phase separation exhibits smaller length scale than the primary phase separation. Figure 3.10 shows an illustration of secondary phase separation taking place in a symmetric polymer blend during phase separation via spinodal decomposition. It is symmetric in terms of system solubility (same solvent solubility), substrate interactions (affinity with the substrate), and concentration (*i.e.* 50:50 ratio). Secondary phase separation has been observed experimentally in immiscible polymer blends (Tanaka and Araki, 1998, Kim *et al.*, 1993, Alig *et al.*, 2003, Tanaka, 1994, Yamamura *et al.*, 2002), and during the spin-

coating process (Ebbens *et al.*, 2011, Heriot and Jones, 2005). It has also been investigated through modelling and computer simulation (Henderson and Clarke, 2004, Tran *et al.*, 2006).

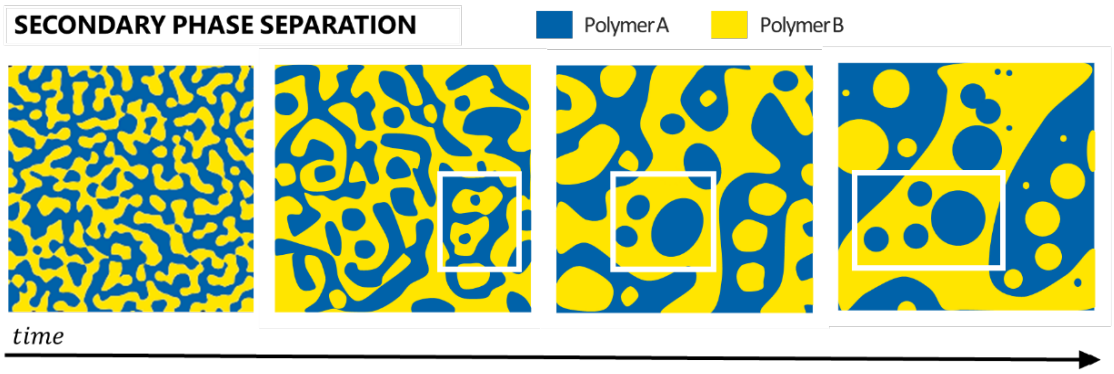

Figure 3.10 . *Schematic illustration of the secondary phase separation during phase separation of a symmetric immiscible polymer blend. During phase separation of polymer A and polymer B, the two phases coarsen, and secondary phase separation takes place. The white rectangles show areas where secondary phase separation is particularly visible. Adapted from Tanaka and Araki (1998).*

It was found that secondary phase separation occurs only if the second quench is sufficiently deep. Henderson *et al.* (2004) could quantify the maximum degree of secondary phase separation as a function of quench depth and found that the greater the quench depth, the greater the degree of secondary phase separation and the finer the secondary morphology.

3.2.4 Coarsening of phase-separated structures

The growth of bicontinuous or discontinuous structures in phase-separated polymer mixtures are governed by different coarsening mechanisms: hydrodynamic growth (Siggia, 1979), droplet coalescence (Chesters, 1991), and Ostwald ripening (De Gennes *et al.*, 2004, Hill, 1995), illustrated in Figure 3.11. Hydrodynamic growth takes place within a bicontinuous structure due to differences in the Laplace pressure, which corresponds to the pressure difference between the inside and outside of a curved surface between two phases, caused by surface tension at the interface. The Laplace pressure $p_{Laplace}$ is proportional to the product of the interfacial tension γ and the curvature (Solon *et al.*, 2018) $1/R$ (where R is the radius of curvature): $p_{Laplace} \sim \gamma/R$. The pressure gradient between the thinner arms (regions with high curvature) and the thicker areas (region with smaller curvature) shown in Figure 3.11a (pressures $p_1,\ldots,p_5 > P_A$), causes a Poiseuille flow of material from the outside arms to the inner thicker areas, causing hydrodynamic growth.

During coalescence of the discontinuous structures, the droplets merge to form new larger droplets (Chesters, 1991). After the creation of a connecting bridge between the two surfaces of the droplets (see Figure 3.11b), the speed of the coalescence results in a competition between the capillary forces in favor of the merge and the viscous forces slowing it down (Aarts *et al.*, 2005). The coalescence can be induced by Brownian motion, concentration gradients, or by collision-induced phenomena (Bray, 2003). During Ostwald ripening, smaller droplets feed larger droplets that grow and expand (De Gennes *et al.*, 2004, Hill, 1995). Both coalescence and Ostwald ripening are governed by diffusion.

All these growth mechanisms are time-dependent, and the characteristic length scale $L(t)$ approximately follows a time-dependent power law function, $L(t) \sim t^n$, where the exponent n depends on the type of coarsening mechanism(s) (Dhont, 1996). Bray *et al.* (2003, 2010) studied this exponent and found two regimes: the diffusive regime with $n = 1/3$ and the hydrodynamic regime with $n = 1$.

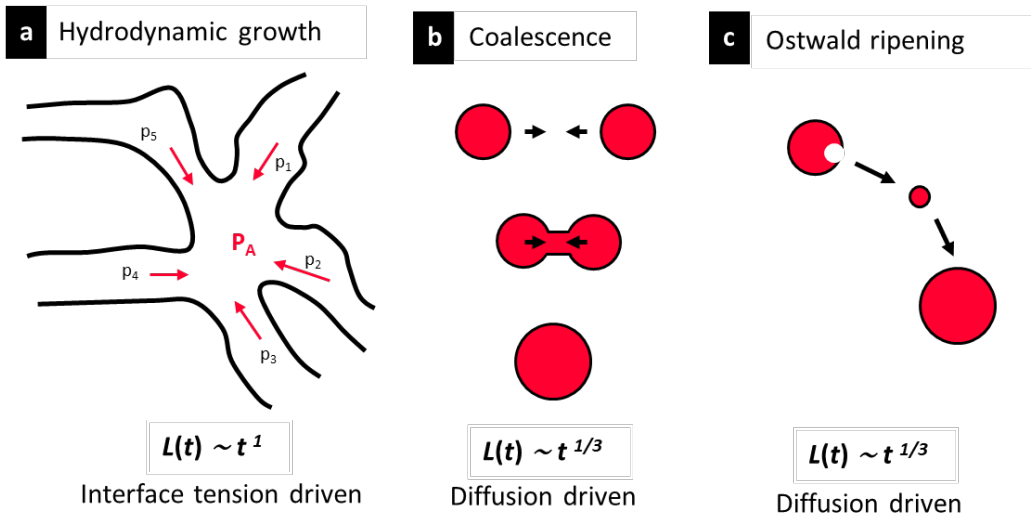

Figure 3.11 *Illustration of the three coarsening mechanisms, a) hydrodynamic growth, b) coalescence, and c) Ostwald ripening.*

In Figure 3.11, the coarsening of bicontinuous structures (Figure 3.11a) relates to $n = 1$ and the growth of discontinuous structures relates to coalescence and Ostwald ripening with $n = 1/3$ (Figure 3.11b and c). The exponent *n* is a good indicator of which coarsening mechanism is dominating (Bouttes *et al.*, 2015, Scholten *et al.*, 2004a). With regards to interfacial tension driven coarsening mechanisms, a transition from one mechanism to another can take place. Experimentally, the coarsening rate of bicontinuous polymer mixtures have been previously studied (Bailey *et al.*, 2007, Lorén *et al.*, 2001) and two regimes were identified: a diffusive regime at small length scales and less well-defined interfaces with the exponent $1/3$ and a hydrodynamic regime at larger length scales and well defined interfaces with a transition to the exponent 1, as first predicted by Siggia (1979).
Other growth laws have been found. The growth law $L(t) \sim t^{2/3}$ was first predicted by Furukawa (1985) under the conditions of capillary and inertial effects. Kendon *et.al. (2001)* used lattice Boltzmann simulations and explained that the exponent $2/3$ for the inertial regime has never been observed experimentally, partly because the time needed for observing this regime is very long. In addition, a $n = 2/3$ regime has been observed at late times in simulations of two-dimensional binary liquids (Alexander *et al.*, 1993, Farrell and Valls, 1989, Datt *et al.*, 2015, Kendon *et al.*, 2001).

The theories and simulations mentioned above were developed for bulk 3D systems. When studying phase separation in thin films, the confinement effect also needs to be considered. During shrinkage of the film, the phase separation might undergo a transition from 3D to nearly

2D structure evolution (refer to **Paper III**), and the cross-over occurs when the characteristic length scale of the structure is in the order of the film thickness (Sung *et al.*, 1996).

3.2.5 Influence of solvent quenching on phase separation

In this work, phase separation is initialized by solvent evaporation (solvent quenching) which leads to a substantial increase in the viscosity of the polymer mixture. This decelerates and eventually retards the coarsening and finally leads to kinetic trapping of the structure in a non-equilibrium state (Schaefer *et al.*, 2016).

Phase separation induced by solvent evaporation is particularly challenging to understand, because during the evaporation, the state of the mixture changes continuously, and the impact of this transforming state on the structure evolution is not fully understood (Schaefer *et al.*, 2015b). However, the effect of solvent evaporation on the phase separation has been theoretically investigated. For example, previous theoretical work has shown that faster evaporation is expected to lead to smaller features in the final dried structures (Kouijzer *et al.*, 2013, van Franeker *et al.*, 2015, Walheim *et al.*, 1997). The characteristic length scale of the phase-separated structure depends on the coarsening time but also on the time-dependent depth of the solvent quench (Schaefer *et al.*, 2015b, Schaefer *et al.*, 2016). The solvent quench corresponds to the final distance in the phase diagram from the binodal line to the final blend composition when all solvent has evaporated. Faster evaporation leads to a deeper solvent quench, and the characteristic length scale is expected to become smaller (Schaefer *et al.*, 2015a).

Cummings *et al.* modelled solvent evaporation during thin film formation in a phase-separating polymer mixture using linearized non-equilibrium thermodynamics (Cummings *et al.*, 2018). It was demonstrated that kinetical trapping can lead to rougher films at the air interface (De Gennes, 2002). Buxton and Clarke (2007) have simulated the evolution of a polymer blend solution undergoing solvent evaporation and phase separation as the system moved from the one-phase to the two-phase region of the ternary phase diagram. They predicted that phase separation occurs initially at the air-film surface, where solvent concentrations are the lowest and then progressively propagates down through the film. Zoumpouli and Yiantsios (2016) examined the effects of hydrodynamics on polymer phase separation-induced morphologies in thin films formed during evaporation. They used Cahn-Hilliard and Flory-Huggins theories to describe the free energy of the phase-separating systems. They found a difference between symmetric and asymmetric systems; symmetric in terms of system solubility (same solvent solubility), substrate interactions (affinity with the substrate), or concentration (*i.e.* 50:50 ratio). Asymmetric systems tend to form lamellar configurations (horizontal layers) during phase separation, whereas symmetric ones tend to form laterally segregated configurations (vertical pillars). In this work, structure evolution of asymmetric and symmetric EC/HPC systems were explored.

3.2.6 Phase separation in spin-coated thin films

Spin-coating is used to prepare uniform thin films in the thickness range of micrometers to nanometers. The substrate is fixed on the rotation plate and rotates the sample when the spinning starts. The centrifugal force drives the liquid radially outward while viscous forces and surface tension cause a flat deposition on the surface. Finally, the thin film is trapped by the solvent

evaporation. Spin-coating is a broadly used technique for producing uniform, thin polymer films (Fowler *et al.*, 2016, van Franeker *et al.*, 2015, Heriot and Jones, 2005). There has been an increasing interest in this technique due to the possibility of obtaining a broad range of different morphologies and hence the ability to tailor the structure (van Franeker *et al.*, 2015, Zhang *et al.*, 2006). Figure 3.12 shows the schematic principle of phase separation during spin-coating. First, the casting solution is deposed in excess onto the substrate. Then the spinning leads to the formation of a thin film due to the excess being projected onto the outside walls of the spin-coater. Subsequently, the evaporation of the solvent triggers the phase separation.

It has been found experimentally that the final morphology of the phase-separated film depends on a wide range of factors including properties of the polymers (molecular weight (Li *et al.*, 2004), solubility (Walheim *et al.*, 1997), surface tension, and viscosity), properties of the blended solution (solid content (Dunbar *et al.*, 2010), solvent properties (Walheim *et al.*, 1997), blend ratio), and properties of the substrate (chemistry (Walheim *et al.*, 1997), roughness, size and shape). Along with the polymer and substrate features, the final morphology also depends on the spin-coating parameters such as the spin speed (Fang *et al.*, 2010), acceleration, spin time, and the surrounding atmosphere (Mokarian-Tabari *et al.*, 2010).

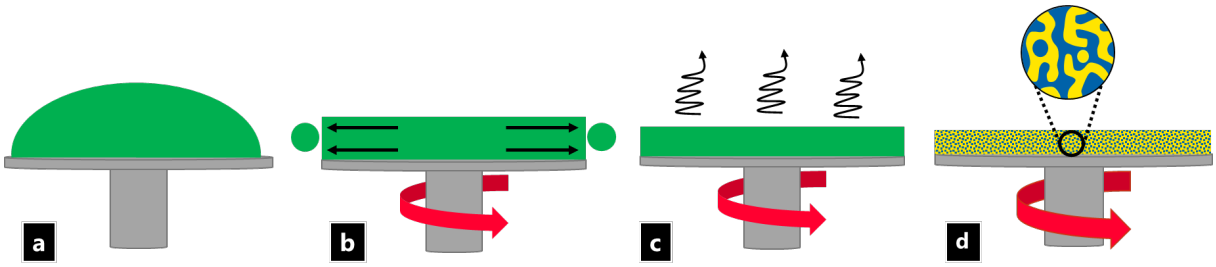

Figure 3.12 *Schematic principle of spin-coating with the different steps a) deposition of the spin cast solution b) spinning and film formation c) evaporation, and d) drying of the solution and phase separation.*

Toolan and Hose (2013) developed an *in situ* method for studying the phase separation of PS/PMMA systems (polystyrene/poly(methyl-methacrylate)) using synchronized stroboscopic LED illumination with a highly sensitive electron-multiplying charge coupled device camera (EMCCD) connected to an optical microscope. They proposed a two-step mechanism for the phase separation during spin-coating: a hydrodynamic thinning (flow dominated step) followed by a solvent thinning (solvent evaporation dominated) step. They determined the influence of the spin-coating parameters on the final morphology of the film. Furthermore, a relationship between characteristic length scale and thickness has been demonstrated for thin films made of synthetic polymers (Schaefer, 2016, Williams *et al.*, 2013, van Franeker *et al.*, 2015, Muller-Buschbaum and Stamm, 2001). It has been found that the length scale increases with increasing the thickness of the film. In addition, a wide range of models have been proposed to explain the experimental observations such as vertical solvent gradient (Buxton and Clarke, 2007), Marangoni instabilities (Scriven and Sternling, 1960) and stratification during spin-coating. However, information about such relationships in mixed biopolymer systems such as mixtures of EC and HPC is lacking.

3.2.7 Influence of surface on phase separation

During phase separation the system can go through several phenomena, related to the surface. In general, phase separation is never surface-free, and depending on the special affinity of either phase, the phase separation can be perturbed by the surface. However when making thicker films, the surface is influencing the phase separation up to a certain distance from the substrate (Puri and Binder, 1994). Above this distance we have more a bulk- type phase separation.

One possible phenomenon related to the surface is the wetting, happening by preferential wetting of solid surface by one or several components of a complex mixture (Jasnow, 1984, De Gennes, 1985). It can affect the development and the kinetics of the phase separation and coarsening, independently of whether the obtained structure is bicontinuous or discontinuous. In addition, Tanaka (2001) pointed out that it could also induce a secondary phase separation (refer to section "3.2.3.4 Secondary phase separation") and demonstrated that hydrodynamics plays a role in the evolution of phase-separating fluid mixture interacting with solid surfaces.

Figure 3.13 shows the two possible types of wetting behaviors in a capillary (2D confinement) at equilibrium: complete wetting forms layered structures; and partial wetting forms droplet-like structures. In Figure 3.13, the yellow phase has more affinity with the solid surface than the blue phase. In other terms, it is energetically more favorable for the yellow phase to wet the surface. Tanaka discussed the hypothesis of having different types of coarsening depending on wettability strength: a 3D growth for weak wettability and a 2D growth for strong wettability.

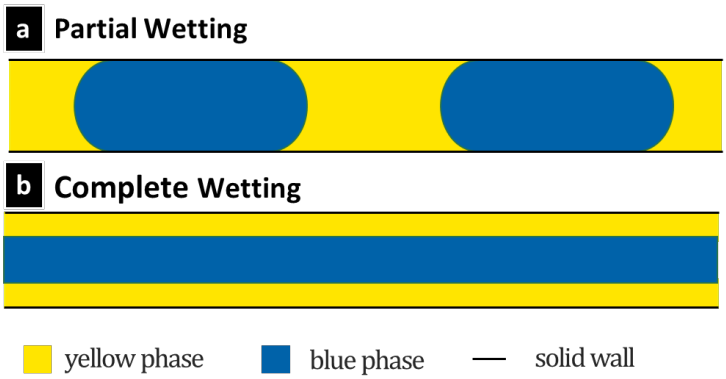

Figure 3.13 *Final equilibrium structures for a) partial and b) complete wetting. Here the yellow-phase is more capable to wet the solid wall than the blue-phase. Adapted from Tanaka (2001).*

Phase separation in confinement has been widely studied (Jinnai *et al.*, 2003, Fransson *et al.*, 2009, Wassén *et al.*, 2013, Zolali and Favis, 2017, Tanaka, 1994, Binder *et al.*, 2010, Jamie *et al.*, 2012, Wise and Millett, 2018). It has been shown that the time dependency can be influenced by the confinement (see section "3.2.4 Coarsening of phase-separated structures and time dependency"). For example, Wiltzius *et al.* (1994) studied the influence of wetting on the time dependency of the coarsening mechanisms. Using light scattering, they studied the phase separation of a fluid mixture at a glass interface and in bulk. Because of the formation of a wetting layer parallel to the surface, they found that at the substrate interface, the power law exponent was higher than in the bulk, and the coarsening faster than in the bulk. In the bulk in 3D, as explained in the previous section the length scale follows a $n = 1$ behaviour (hydrodynamic regime). However, for 2D structure evolution, certain hydrodynamics

instabilities do not occur and instead, coarsening occurs through a diffusive process, leading to $n = 1/2$ (Jinnai *et al.*, 2003).

3.3 The EC/HPC system and phase separation

3.3.1 Cellulose and derivatives

3.3.1.1 Cellulose

Cellulose is a polysaccharide and the principal component of the primary cell wall of green plants. Cellulose is the most abundant organic polymer on Earth (Khandelwal and Alan, 2013). In industry, cellulose is mainly used to produce paper and is extracted primarily from wood pulp and cotton. As a polysaccharide, cellulose is composed by D-glucose units (see Figure 3.14) linked by β(1→4)-glycosidic bonds forming a linear chain. The numerous hydroxyl groups on each unit form hydrogen bonds with neighboring chains, forming crystalline regions and making native cellulose, a rigid, highly oriented and highly crystalline polymer (Klemm *et al.*, 2005). Substitutions of these hydroxyl groups can produce cellulose derivatives with a wide range of properties.

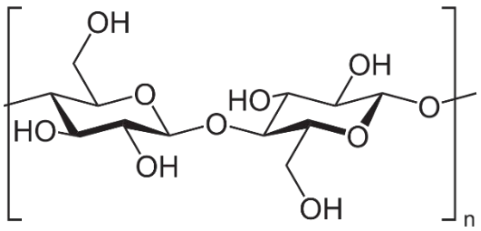

Figure 3.14 *Chemical structure of cellulose repetitive unit (Klemm et al., 2005).*

3.3.1.2 EC and HPC

Etherification and esterification (Fox *et al.*, 2011) of cellulose can be used to produce ethylcellulose (EC) and hydroxypropylcellulose (HPC), respectively. The average number of substituted hydroxyl groups per glucose unit is referred to as the degree of substitution (DS). Complete substitution is obtained with a DS of 3. In general, the nominal viscosity is the parameter used to characterize the grade of EC and HPC. It gives an indication of the average molecular weight, Mw of the batch. For EC, nominal viscosity it is often provided in the grade name and expressed in centipoises (cPs). Due to the strict regulations on pharmaceuticals, the grade and the Mw are specified for each batch.

3.3.1.2.1 Hydroxypropylcellulose

Hydroxypropylcellulose (see Figure 3.15) is an ester of cellulose where the hydroxyl groups of the repeating glucose units have been transformed into hydroxypropyl groups. HPC is prepared by reacting alkali cellulose with propylene oxide. While cellulose is a very crystalline polymer and not soluble in water, HPC is highly soluble in water at room temperature due to the large number of hydrophilic groups (Sakellariou and Rowe, 1995).

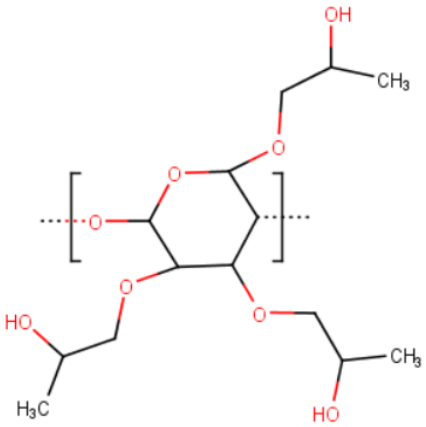

Figure 3.15 *Chemical structure of hydroxypropylcellulose repetitive unit.*

HPC is also soluble in ethanol. HPC molecular mobility and chain orientation make it difficult to determine the glass transition temperature (T_g) with accuracy. However, a T_g of about 124°C has been proposed for HPC (Sakellariou *et al.*, 1985). The solubility of HPC in its solvent is enhanced by the hydrogen bonds and therefore a HPC-solvent system exhibits a lower critical solution temperature (LCST) between 40-45°C. Above this temperature, HPC is no longer soluble in water and form a crystal solvate of six water molecules per unit of HPC (Fischer *et al.*, 1995). HPC has been used in pharmaceutical applications to form tablets (Picker-Freyer and Dürig, 2007), coatings (Huang *et al.*, 2013) and as ophthalmic inserts for treatments of dry eye syndrome (Nguyen and Latkany, 2011). In food industry, it has been used as emulsifier and as bubble stabilizer in bread (Andersson *et al.*, 2011, Schober *et al.*, 2008).

3.3.1.2.2 Ethylcellulose

Ethylcellulose (see Figure 3.16) is an ether of cellulose where the hydroxyl groups on the glucose units of cellulose have been converted to ethyl ether groups. EC is produced by reacting alkali cellulose with an appropriate alkyl halide (Klemm *et al.*, 2005).

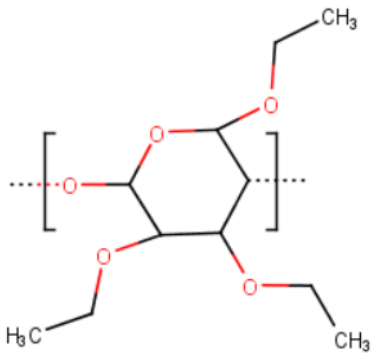

Figure 3.16 *Chemical structure of ethylcellulose repetitive unit.*

With its high glass transition temperature (T_g = 124-132°C (Sakellariou *et al.*, 1985)), EC can be used as a plasticizer in coatings to improve the mechanical properties and the thermal behavior. At room temperature, EC is totally insoluble in water due to the large number of hydrophobic groups. However, it is soluble in ethanol and to some extent in ethanol-water mixtures.

3.3.2 Phase separation in EC/HPC mixtures

EC and HPC can be dissolved in ethanol at low concentrations. During ethanol evaporation, the polymer blend concentration increases, and the mixture becomes incompatible and starts to phase separate. EC/HPC mixtures phase separate through segregative phase separation which results in an enrichment of the polymers in two separate phases (see Figure 3.6) (Piculell *et al.*, 1995). When the evaporation of ethanol is complete, a kinetically trapped, phase-separated film of EC/HPC remains.

As described in section "3.2 Phase separation in polymer mixtures", phase diagrams are useful to describe the state of a polymer mixture. But phase diagrams are unique to each polymer system, and they are determined for a given temperature and pressure. The system of interest in this study is EC/HPC in ethanol and the selected grades are HPC-LF and EC 10 cps.

Figure 3.17 shows the phase diagram for these specific grades of EC and HPC elaborated at atmospheric pressure for two temperatures: 25°C (Figure 3.17 b) and 50°C (Figure 3.17 a) (Baderstedt, 2011). Baderstedt *et al.* (2011) let EC/HPC solutions rest in vials for at least one month and performed a visual inspection of the meniscus to determine if the solution was one phase or two phases.

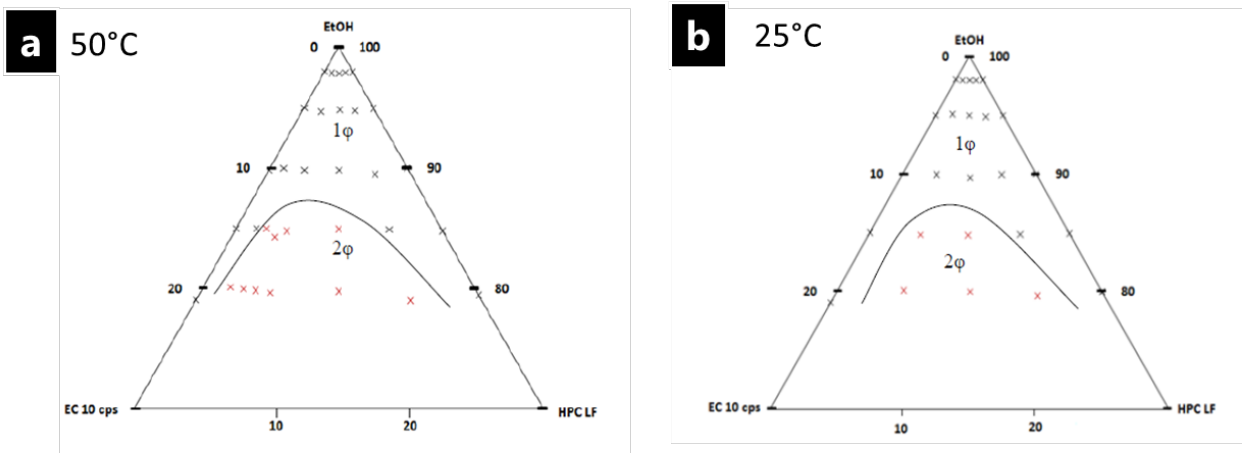

Figure 3.17 *Ternary phase diagrams of EC 10cps and HPC-LF in ethanol at a) 50°C and b)25°C. The red dots represent the samples that have phase-separated, whereas the lines are suggestions for binodal lines. (Baderstedt, 2011)*

3.3.3 EC/HPC systems for drug release

The presence of the water-soluble HPC in the phase-separated film of EC and HPC is a good feature for drug release. Immersion of such film in an aqueous media (*e.g.* body liquids) leads to a leaching of HPC and the formation of pores in the EC matrix. Through these pores the drug can be released. By tailoring the structure of the pores, the drug release rate can be controlled. Several studies have been performed to find a method to regulate the pore shapes in the final film.

Previous work have shown that the structure of EC and HPC in the film and its properties depend on numerous parameters such as the EC/HPC ratio, the molecular weight distribution of EC and HPC (Andersson *et al.*, 2009, Andersson *et al.*, 2013), and the coating processing parameters (temperature, gas flow, spray rate) (Marucci *et al.*, 2009). Differences were observed in the microstructure, in water and solute permeability, in drug release rate and release

rate of HPC. It should be noted that most of this work was performed using a rotating drum and spray nozzle device to mimic the industrial set-up of fluidized bed spraying. However, it was found that a higher molecular weight of HPC results in a lower permeability (Andersson *et al.*, 2016). Marucci *et al.* (2009) studied permeability and leaching of EC/HPC films with different compositions. They discovered the presence of a percolation onset at about 22 wt% HPC (see Figure 3.18). When the HPC fraction exceeded 22 wt%, both the amount of HPC leached out and the water permeability of the films increased linearly with the HPC fraction up to a certain concentration of HPC (Fager, 2018, Andersson *et al.*, 2009, Marucci *et al.*, 2009, Jarke, 2009, Marucci *et al.*, 2011).

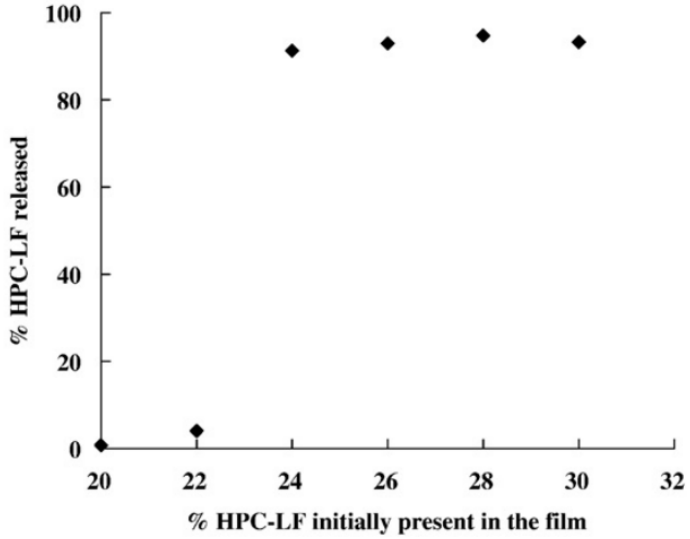

Figure 3.18 *HPC-LF leached from EC/HPC-LF films after 24h exposure to phosphate buffer solution at pH 6.8 under well-stirred conditions. (Marucci et al., 2009).*

3.3.4 Industrial process of fluidized bed spraying

In industry, coating of drug-containing pellets with thin phase-separated films is often performed batch-wise using fluidized bed spraying. In the case of EC/HPC coating, the Wurster coating process is used, which is a bottom spray fluidized bed technique (Heinrich *et al.*, 2015, Lipin and Lipin, 2022, Havaić *et al.*, 2018). In this device, the pellets are circulating through the spraying zone and then back to the bottom of the device. The polymer mixture is in one phase state and the mixture is sprayed onto the pellets in the spraying zone. Many small droplets hit the pellet and form a coating onto its core. With the ethanol evaporation, the mixture starts to phase separate, and the film structure useful for drug release is formed. Figure 3.19 shows an illustration of the coating process and the pellet trajectory in the device. Thanks to the gas circulation (nitrogen with ethanol) the particles go from the bed to the spraying zone formed by the spray nozzle, and back in the bed in a chaotic trajectory. The pellets will pass through the spraying zone many times during the processing. Consequently, the pellets perform a cycle with spraying, phase separation and drying, which results in a film. The cycle is repeated until obtaining the desired coating (see Figure 3.19).

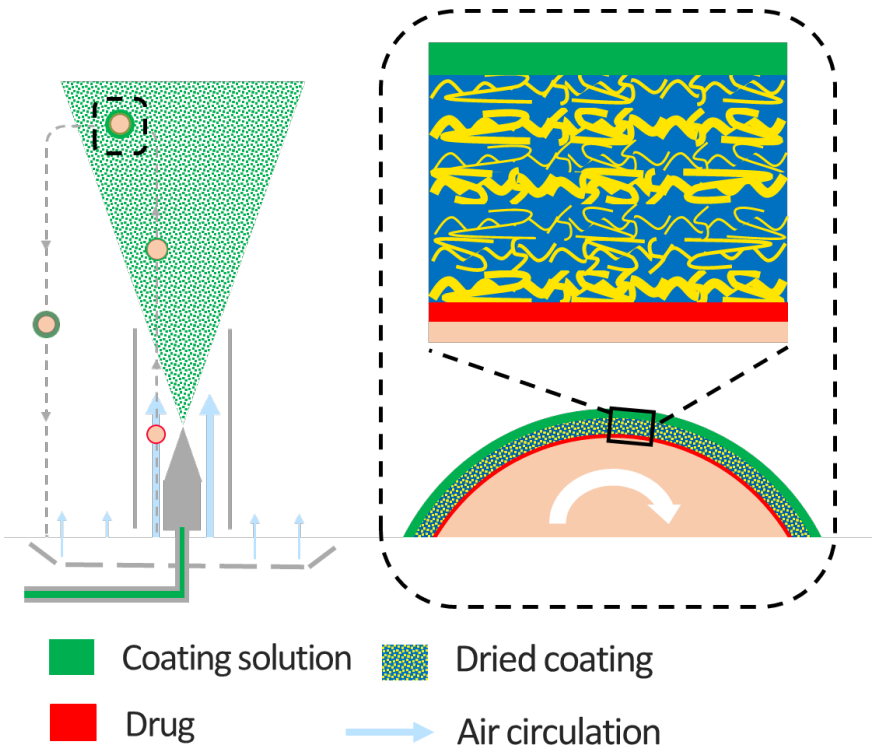

Figure 3.19 *Schematic illustration of the industrial coating process using a fluidized bed spaying. To the left, the fluidized bed with the nozzle spraying droplets of the coating solution onto the circulating pellets. To the right, magnified structure of a pellet being coated. Each passage in the spraying zone corresponds to a layer.*

The structure of industrial pellets have been analysed at high resolution using FIB-SEM, allowing the characterization of the coating structure in terms of porosity, connectivity, and tortuosity (Fager, 2020, Fager *et al.*, 2020a, Fager *et al.*, 2020b, Röding *et al.*, 2021, Fager *et al.*, 2021a, Fager *et al.*, 2021b). According to a recent study (Fager, 2020), the EC/HPC coating structure after spraying and leaching of the water soluble HPC takes the form of a superposition of layers exhibiting different porosity. These findings have inspired the idea that the droplets have been distributed on the surface and a thin layer is deposited for each passage in the spraying zone, which gives rise to the formation of a multilayer film. During the circulation, a large number of droplets is hitting the pellet and spread all over the surface while the pellet is spinning due to the air circulation. To the right in Figure 3.19, the layered structure around the pellet formed during coating is illustrated.

4 Materials and Methods

In this section, an overview of the material and methods used in this work is given. First, the preparation of the EC/HPC solutions for the different experiments is explained. Then, the principle of spin-coating, confocal scanning laser microscopy, scanning electron microscopy, rheology and profilometry are addressed. Finally, the image analysis methods are described.

4.1 Materials

The HPC used in this work was Klucel Pharm HPC, grade LF (Ashland Inc, Covington, Kentucky, USA) with a mean molecular weight of 95 kDa according to the manufacturer (Ashland, 2017). The EC used in this work was Ethocel Standard Premium, viscosity 10 cps (Dow Cellulosics, Dow Chemical Company, Midland, Michigan, USA) with a mean molecular weight of 30 kDa according to the manufacturer (DowCellulosics, 2005).
The batches of HPC and EC were the same during the whole work.

4.2 Preparation of EC/HPC solutions

Solutions of HPC and EC were prepared. 6 wt% of polymer blends were mixed in a solution of 2 mM Na-fluorescein and ethanol, see Figure 4.1. The EC/HPC polymer ratios studied were 15, 20, 22, 25, 30, 35, 37, 40, 45, 50, 55, 60 and 85 wt% of HPC in the polymer blend. This procedure was used to make the solutions in **Papers I - IV**. For the viscosity measurements (**Paper I**), solutions were prepared with the following compositions: 22, 30, 45, and 60 wt% HPC and 4 ratios of solvent: 94, 90, 85 and 80 wt% of ethanol (96 vol%). The ethanol was added to the polymer blend and the solutions were sealed and stirred overnight at room temperature.

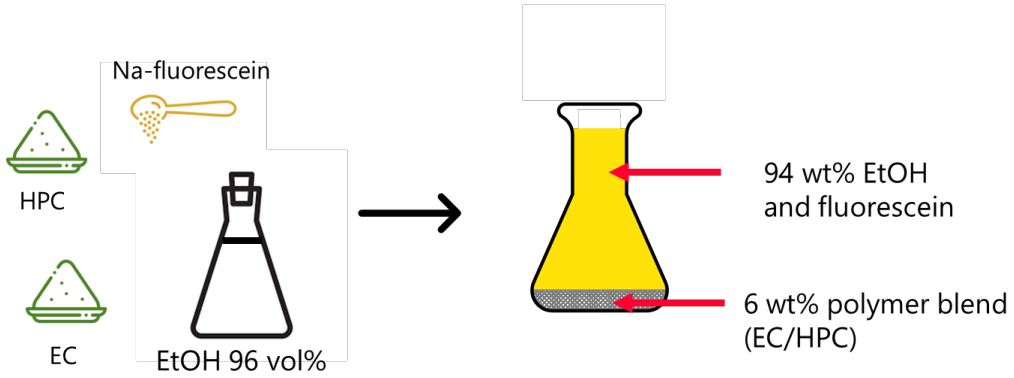

Figure 4.1 *Preparation of EC/HPC solutions in ethanol with fluorescein as fluorochrome.*

4.3 Rheology of EC/HPC mixtures

To determine the zero-shear viscosity of the stock solutions (6 wt% polymer blends in 94 wt% of ethanol) and during evaporation, experiments on different EC/HPC mixtures were conducted using a rotational rheometer (**Paper I).** A logarithmic flow sweep was performed with a bob and cup geometry. The system was closed to prevent evaporation. A similar approach was used to determine the viscosity of EC/HPC solutions by Andersson *et al.* (2013). The zero-shear

viscosity was extrapolated from the rheology data (Barnes, 2000) (see the blue arrow in Figure 4.2). The specific viscosity at zero shear rate was calculated using $\eta_{sp,zero\ shear} = \eta_{zero\ shear}/\eta_{solvent} - 1$.

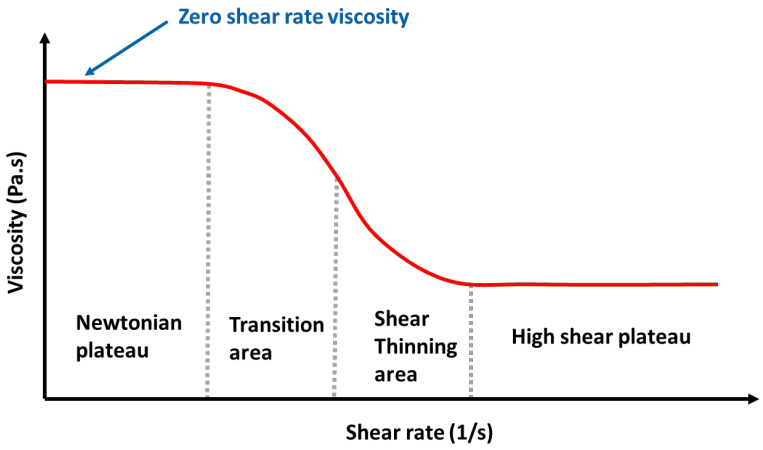

Figure 4.2 *Viscosity profile of a typical shear thinning mixture. Adapted from Morris et al. (1981).*

4.4 Spin-coating of EC/HPC films

It is challenging to follow the multilayer formation and the phase separation occurring in a fluidized bed. It is very difficult to characterize the structure evolution *in situ* since it is not feasible to introduce a characterization method equipment inside the fluidized bed chamber. One technique with which phase separation during solvent evaporation in a thin film is much easier to follow and understand is spin-coating. Therefore, spin-coating was selected to mimic the structure formation occurring in a fluidized bed in this work. The spin speed was varied between 1 000 and 10 000 RPM and the spin time between 1s and 1min. The volume of the solution was optimized and fixed at 200 µL. The polymer solution was deposed onto different substrates, depending on the study: a 25x7 mm^2 glass microscope slide for the study of final structure of dried monolayer films (**Paper I**). For the kinetics study (**Paper II** and **Paper III**), and the multilayer films study (**Paper IV)** the solution was poured in a 22 mm diameter round glass bottom petri dish. For electron microcopy (**Paper IV**), the substrate used was carbon tape deposited on a 12.7 mm diameter aluminum pin stub. For multilayer film deposition, deposition cycles consisted of three steps (**Paper IV**). The spin-coater bowl was equipped with nitrogen flow, which ensured a nitrogen environment while coating. In this work, we used a Laurell spin-coater (WS-650MZ-23NPP, Laurell Technologies, North Wales, Pennsylvania, USA).

4.5 CLSM and analysis of phase separation kinetics

Confocal laser scanning microscopy (CLSM) is a fluorescence microscopy technique which offers possibilities to determine material structures at the micrometer scale. The image information is coming from a thin confocal plane in the specimen, which allows for three-dimensional imaging of the structure. For decades it has been an important technique to study soft materials and biological samples (Pawley, 2006). CLSM is a non-invasive technique, it does not require a long and difficult preparation of samples and provides the possibility to study

bulk material. In this work, CLSM was used for the characterization of phase-separated EC/HPC dried monolayer (**Paper I**) and multilayer films (**Paper IV**), to follow *in situ* the kinetics of phase separation and coarsening mechanisms on the in-plane (**Paper II**) and cross-sectional (**Paper III**) structure evolution, and to monitor the interaction between a multilayer film and a droplet of polymer solution (**Paper IV**). The CLSM used were a Leica TCS SP5 (Leica, Wetzlar, Germany) and a Facility Line (Abberior Instruments, Göttingen, Germany).

4.5.1 Principle and components

Figure 4.3 shows a schematic illustration of a CLSM with the principal components. To obtain an image of the specimen, one or several laser beams are used to excite fluorochromes in the specimen at specific wavelengths. The laser power transmitted from each laser is controlled by an acousto-optical tunable filter (AOTF). The laser beam goes through a first pinhole called the illumination aperture and is directed towards the specimen, going through the beam splitter, the scanning mirrors, and the objective. The acousto-optical beam splitter mixes the proportion of light coming from each laser in the array and subsequently transmits it to the specimen. Depending on the scale of the structure, the objective features can be changed *i.e.* magnification, numerical aperture and immersion medium. The beam splitter is a filter that differentiates the incoming laser light from the light emitted by the excitation of the specimen. The pinhole removes the out of focus fluorescent light and allows only the light that emanates from the focal plane to go to the detector (Lorén *et al.*, 2007).

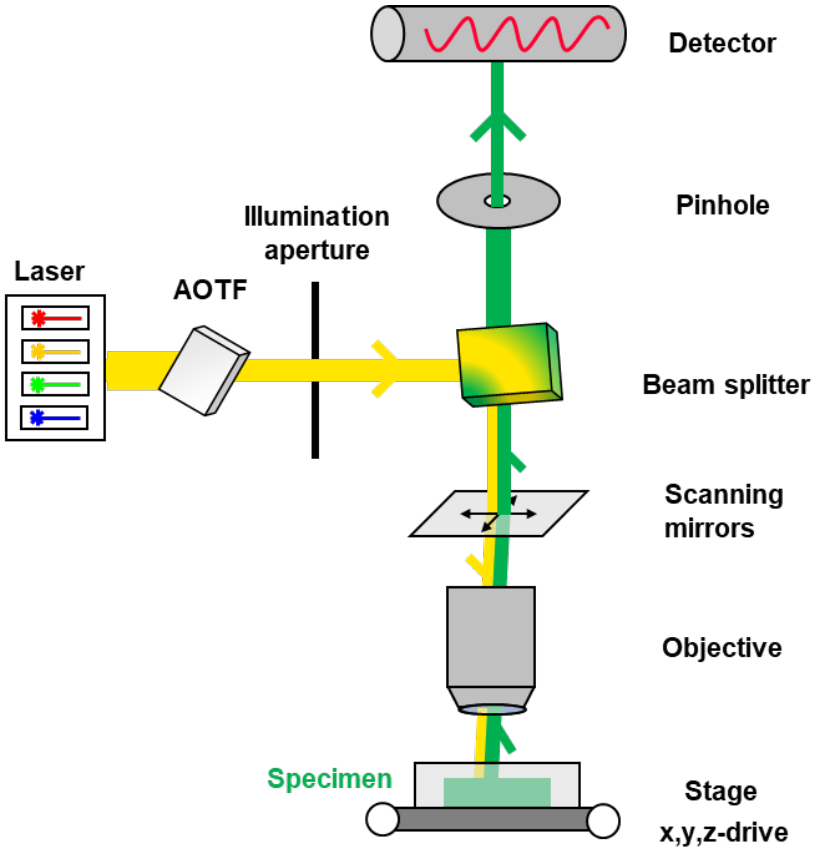

Figure 4.3 *Scheme of a confocal laser scanning microscope. Adapted from Lorén et al.(2007).*

4.5.2 Fluorescence

Fluorescence is the ability of some atoms and molecules to absorb the light from a specific wavelength and subsequently re-emit it at longer wavelengths after a short time interval. The CLSM technique is based on using a fluorescent sample. Hence, the sample preparation solely consists of labelling the specimen with fluorochromes (if the sample is not already auto-fluorescent) (Shotton, 1989). Fluorochromes can be dyes added to the solution with affinity for the structure of interest, or fluorescent molecules covalently bonded to the molecule of interest. Different species can be detected separately by using different fluorochromes. Each fluorochrome has a typical emission spectrum and the detector can simultaneously detect different intervals of emission wavelengths for several fluorochromes. If the emission spectra are non-overlapping, it is possible to detect several species at the same time.

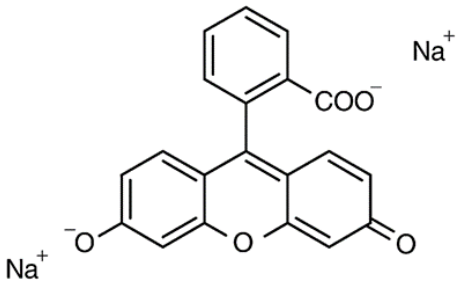

Figure 4.4 *Chemical structure of sodium fluorescein (Barbero et al., 2009).*

For the EC/HPC system, sodium fluorescein (see Figure 4.4 for the chemical structure) was used to label HPC. In previous work, sodium fluorescein was mixed into the polymer mixture and its strong affinity with HPC allowed observation with CLSM (Andersson *et al.*, 2009). In other studies, HPC covalently labelled with fluorescein isothiocyanate (FITC-HPC) was used (Deprez, 2016, Jarke, 2009, McDonough *et al.*, 2015).

4.5.3 Spatial resolution

It is of fundamental importance to guide the maximum number of photons emitted by the fluorochromes in the specimen safely to the detector. The spatial resolution is governed by the features of the CLSM: the numerical aperture (NA, typically 0.1 up to 1.45), which determines how much of the re-emitted fluorescent light is collected by the objective; and the working distance of the objective (which decreases when NA increases). It is also important to use refractive index matching as much as possible to avoid aberrations. All these parameters are related to the lateral and axial resolution trough the following equations (Jonkman and Stelzer, 2002).

$$R_{lateral} \propto \frac{\lambda_{emission}}{NA} \quad , and \quad R_{axial} \propto \frac{n\lambda_{emission}}{NA^2} \quad with\ NA = n \sin \alpha$$

where $\lambda_{emission}$ is the wavelength of the incoming laser light, NA is the numerical aperture, n is the refractive index of the immersion medium, and α is the maximum half angle of diffracted light that can enter the lens. Spatial resolution is defined as the minimum spatial separation required between two-point objects to distinguish them as two separate objects. With CLSM,

resolution is always a compromise between spatial resolution, temporal resolution, and noise (Sheppard and Shotton, 1997). The signal to noise ratio sets the limits for how small the pinhole can be. In optics, the Airy disk and Airy pattern are descriptions of the best-focused spot of light that a perfect lens with a circular aperture can make, limited by the diffraction of light (Lorén *et al.*, 2007). It has been shown that a good compromise is obtained at a pinhole size equal to the first minimum in the Airy disk. Many commercial instruments set the pinhole size equal to the first minimum in the Airy disk by default.
In this work, a 488 nm argon laser was used for excitation of the Na-fluorescein used to stain the HPC phase. The signal emitted in the interval 500-600 nm was recorded (the fluorescein emission peak is expected at 515 nm).

4.5.4 Imaging modes in CLSM

The CLSM technique offers many different modes of imaging. In Figure 4.5, we introduce a coordinate system where the in-plane is denoted as the xy-plane and the cross-sectional plane as the xz-plane. Two types of kinetics measurements were performed: xyt measurements with a time interval of 2.575 s between each frame in **Paper II** (Figure 4.5a) ; and xzt measurements with a time interval of 2.77 s between each frame in **Paper III** (Figure 4.5b). The xzt imaging was performed with a galvanometric stage that moves rapidly up and down (16 µm/s) and with high precision in the z-direction permitting to image a slice in the xz-plane with high quality.
The combination of the two planes offers a good view of the phase separation process and the morphology evolution. In **Paper IV,** the xyz mode allowed to obtain xyz stacks (see Figure 4.5c). We used an in-built plugin of Fiji/ImageJ to visualize the 3D structure of the EC/HPC multilayer films (Schmid *et al.*, 2010).

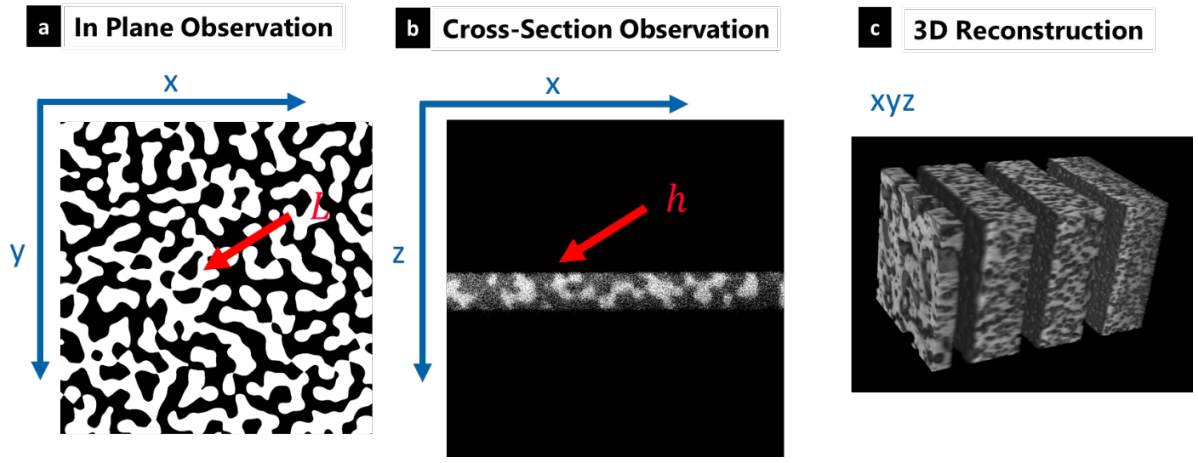

Figure 4.5 *Coordinate system for the kinetic measurements with a) the in-plane xy and b) the cross-section xz. In c), a 3D reconstruction (xyz) of a multilayer film with ImageJ/Fiji is shown.*

By combining the different CLSM modes and image analysis, we could extract the characteristic length scale L and interfacial curvature from the in-plane micrographs (see Figure 4.5a) and estimate the thickness h from the cross-sectional micrographs (see Figure 4.5b).

4.6 Scanning Electron Microscopy (SEM) and Focused Ion Beam SEM (FIB-SEM).

In this work, SEM and FIB-SEM were used to characterize the structure of spin-coated multilayer EC/HPC films. The exact methods are described in **Paper IV**, in the following section we give an overview of the principle of SEM and FIB-SEM. In this work we used a SEM JSM-7800F Prime (JEOL, Tokyo, Japan) and a FIB-SEM Tescan GAIA3 (Tescan, Brno, Czech Republic).

4.6.1 SEM and Electron beam imaging

Scanning electron microscopy (SEM) is a powerful technique to examine the structure of materials with applications in a large number of fields such as metallurgy, geology, biology, and pharmaceutics. In SEM, electrons are utilized to image specimen surfaces with high resolution. First, an electron beam is generated from a source (tungsten filament or a field emission electron gun), then the electron beam is accelerated through a high voltage (*e.g.* 20 kV) by an anode. The anode is positively charged, forcing the electrons to accelerate. The accelerated electron beam goes through a system of electromagnetic lenses to produce a thin beam of electrons which scans the surface of the specimen.

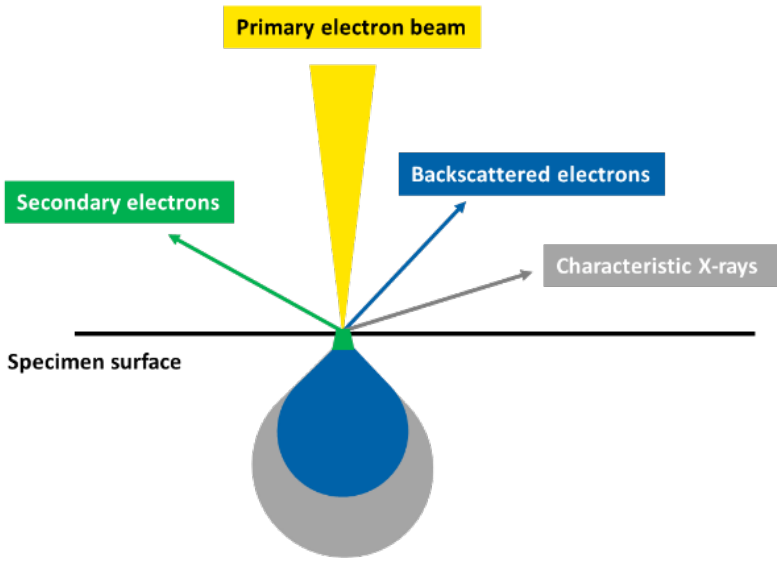

Figure 4.6 *Schematic illustration of the interaction between the electron beam and the specimen. Adapted from Fager (2020).*

The incident electrons from the electron beam interact with the specimen surface resulting in an interaction volume that produces different signals (see Figure 4.6). The most commonly used signals are backscattered electrons, secondary electrons, and characteristic X-rays (see Figure 4.6). Each type of signal has a dedicated detector (Goldstein *et al.*, 2003), resulting in different types of images. The secondary electron image is used to image the surface and gives a high resolution. With the backscattered electron image, the resolution is lower than in the secondary electron, but the backscattered electrons, with their higher energy are generated at greater depth in the sample, they interact with an atom from the specimen, and the signal intensity is dependent on the atomic number of the specimen. Finally, the characteristic X-rays are

produced when electrons from the specimen are ejected from the inner shell, and elementary information and chemical composition can be obtained.

4.6.2 Sample preparation for SEM

When studying soft materials like polymer films, sample preparation for electron microscopy is crucial. The electron beam may give rise to accumulation of charges at the surface due to poor electrical conduction and cause image distortion. To avoid charging, the samples were coated with an Au sputter coater, with thickness ranging from 3 to 20 nm depending on the samples, as described in **Paper IV**.

To study the EC/HPC multilayer films with SEM we needed to obtain cross-sections of the films, which was performed by using a cryostat or FIB-SEM milling, as described in **Paper IV**.

4.6.3 Ion Beam Milling in FIB-SEM

SEM is a characterization technique in which an electron beam is used to scan across the surface of a sample. Associated with a focused ion beam column (FIB), an image of the internal structure can be obtained by slicing and removing materials (see Figure 4.7).

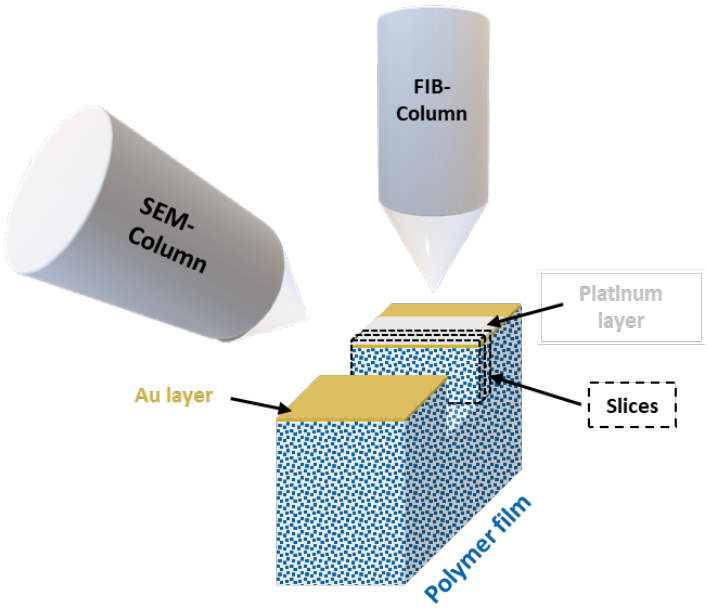

Figure 4.7 *Set-up of combined FIB and SEM microscope with a polymer film as specimen. An Au layer is deposed with a gold sputter coater. A platinum layer is deposed with the gas injection system from the FIB-SEM set-up. Adapted from Fager (2020)*

During the FIB-SEM procedure, ions are used to remove material from a specimen with high precision, to deposit material onto the specimen, and to image the specimen surface. Hence, with the FIB-SEM technique, porous materials as EC/HPC films, can be imaged with high precision, and the 3D structure of the film can be revealed. However, with FIB, one should be aware of the possible beam damage: ions are significantly more massive compared to electrons, and they may sputter away and damage the specimen surface (Giannuzzi, 2005). Therefore, optimization of FIB-SEM parameters is crucial.

In this work (**Paper IV**) we used FIB-SEM to image the 3D structure of porous EC/HPC multilayer films with a method inspired from the work by Fager *et al.* (Fager, 2020, Fager *et al.*, 2020a, Fager *et al.*, 2020b, Röding *et al.*, 2021, Fager *et al.*, 2021a, Fager *et al.*, 2021b).

4.6.4 Leaching of EC/HPC films for electron microscopy

To increase the contrast under electron microscope, samples were leached prior to imaging, thus obtaining a porous film. To study the influence of leaching, CLSM and SEM imaging were performed on 3-layer films made with 4 EC/HPC ratios before and after leaching (22, 30, 45 and 60 wt% HPC). Leaching was performed as described in Fager (2020), in MilliQ water for 24H with gentle agitation. Also, prior to imaging the films were coated with 4nm Au in a sputter coater. Figure 4.8 shows CLSM and SEM micrographs of the top surface of the film before and after leaching.

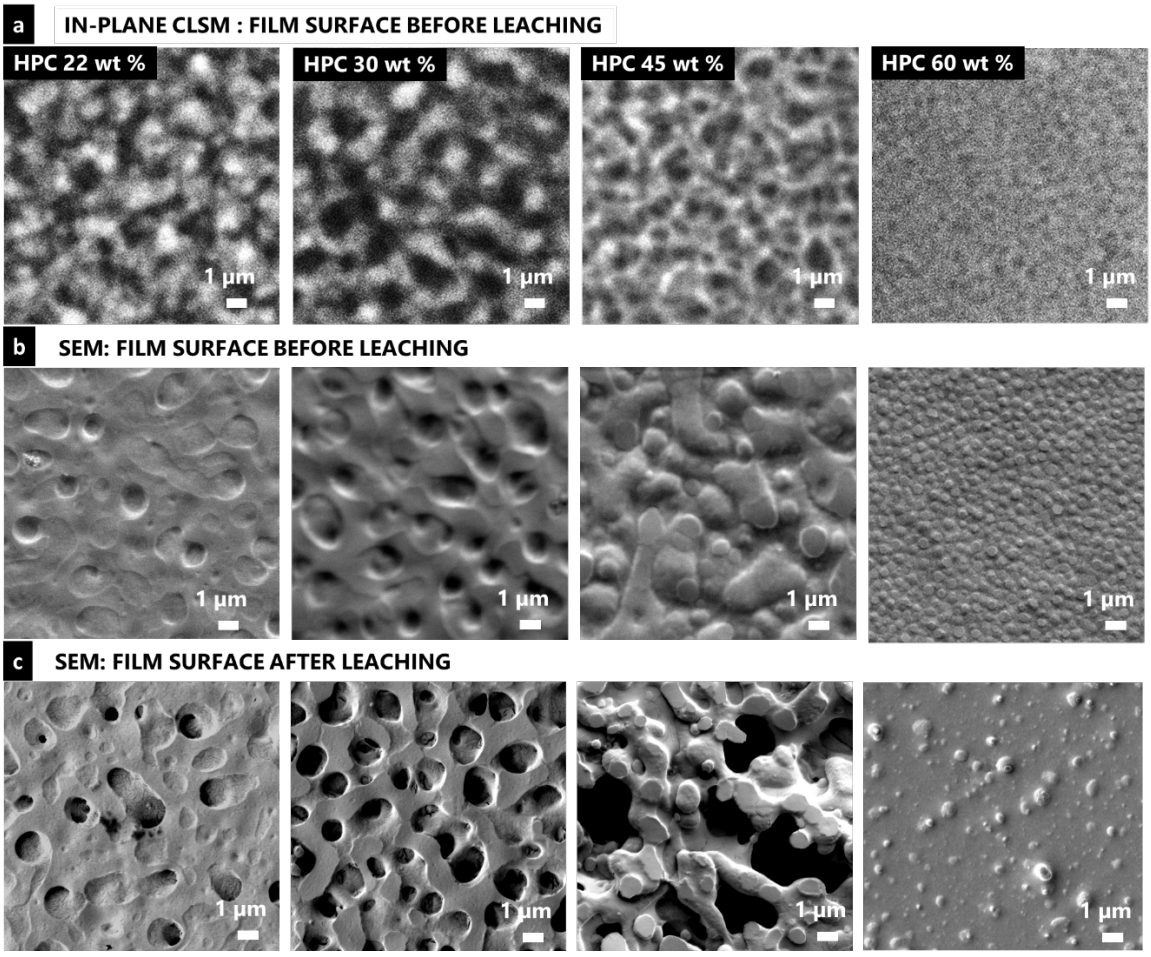

Figure 4.8 *In-plane surface micrographs of 3-layers films with 4 different EC/HPC ratio with a) the CLSM micrographs with HPC in bright, EC in dark, b) the SEM micrographs before leaching, and c) the SEM micrographs after leaching of HPC.*

By comparing the resolutions in Figure 4.8a and Figure 4.8b we can justify the choice of using SEM as a complementary method to study the EC/HPC films. The resolution reached is much higher than in CLSM and information of smaller features can be obtained.

In Figure 4.8b, the features observed are the two phases EC and HPC. The contrast between the two phases is probably mostly topological since the two cellulose derivatives present a similar

density. By looking at the surface morphology, it seems that EC domains are forming convex features bowing outward from the continuous HPC matrix for 45 and 60 wt% HPC films; while the HPC domains are forming features that are curved inward from the continuous EC matrix for 22 wt% and 30 wt% HPC films. Similar shapes and features were observed in Jansson (2014), when looking at EC/HPC films with an E-SEM (Environmental-SEM).
In Figure 4.8b, the continuous phase for 45 wt% HPC and 60 wt% HPC films, is HPC. This is confirmed in the micrographs after leaching in Figure 4.8c, when most of the material has been removed in the 45wt% HPC film, and almost all the material in the 60 wt% HPC film. The continuous phase for 22 wt% HPC is EC. For 30 wt% the structure is more bicontinuous.

4.7 Film thickness determination

To estimate the thickness, a combination of CLSM and image analysis was used (**Paper I, Paper III** and **Paper IV**). However, it was found that by using this approach the thickness could be overestimated and that the results were less accurate for thin samples, especially when the film thickness was close to the axial resolution of the CLSM. The axial resolution of the CSLM measuring the thickness is about $\Delta_z \sim 500$ nm while the profilometer precision is about 1 nm.

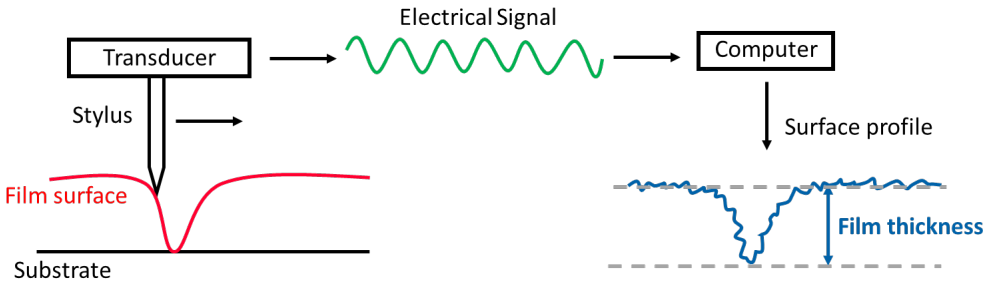

Figure 4.9 *Schematic principle of stylus profilometry. Adapted from (El Khoury, 2017).*

Since profilometry offers more accurate measurements it was used to determine the thickness of the dried films. Stylus profilometers use a contact probe to detect the surface. The diamond stylus is physically moving along the surface to measure the surface height. Prior to the measurement, the film surface was scratched with a razor blade. The stylus slides across the film and uses the difference in height from the film surface to the glass surface (inside of a scratch) to determine the film thickness. The method used is described in detail in **Paper I** and **Paper III**. In this work, a stylus profilometer (Alpha-Step D-100 KLA Tencor, Milpitas, CA, USA) was utilized.

4.8 Image analysis

In this work, image analysis is used to extract quantitative data from the CLSM micrographs. We develop methods to analyze different properties of the phase-separated film. The image analysis was conducted using MATLAB (MathWorks, Natick, MA, USA).

4.8.1 Characteristic length scale determination

The first parameter that we investigated was the characteristic length scale. During spinodal decomposition (SD), a periodicity or characteristic length scale of the bicontinuous (interconnected) pattern is unique for each structure and describes the stage of phase separation. The Cahn-Hilliard model (Cahn, 1965) is the reference model when studying SD and the evolution of the bicontinuous pattern (Playne and Hawick, 2009). Spinodal decomposition can also form discontinuous structures, see Figure 3.6. When the obtained structure is discontinuous, the term characteristic length scale is still used but it then refers to the diameter of the droplet-like inclusions. The Fourier image analysis used to determine the characteristic length scale is explained in detail in **Paper I**. In **Paper II,** we used two methods to extract the length scale, the fast Fourier Transform (FFT) for bicontinuous structures, and the estimation of the diameter for the discontinuous structures.

In this work, we studied the characteristic length scale L(t) to determine the influence of the EC/HPC ratio and the spin-coating parameters on the dried film morphology (**Paper I** and **Paper IV**). Additionally, the characterization of the length scale combined with image analysis methods allowed determination of the time-dependent structure evolution in **Paper II** and **Paper III**.

4.8.2 Curvature map of the interface between EC and HPC

A new image analysis method to determine the time-dependent curvature evolution of bicontinuous systems was developed. It allowed further analysis of the role of interfacial tension driven coarsening mechanisms (refer to section “3.2.3 Mechanisms of phase separation”). The local curvature at the interface EC/HPC was calculated using the xyt CLSM micrographs series (**Paper II**).

To fully understand the phase separation, we wanted to determine which coarsening mechanisms are prominent for different conditions (see section “3.2.4 Coarsening of phase-separated structures"). During hydrodynamic growth (see Figure 3.11), the domains are coarsening, and the shapes evolve from high curvature (small radius) to low curvature (large radius). Being an important indicator of the coarsening mechanisms, changes of curvature at the EC/HPC interface during the coarsening are therefore evaluated. To obtain the curvature, the osculating radius formula developed by Coeurjolly and Svensson (2003) was used. Figure 4.10 shows the principle of osculating radius: the curvature in v_o is given by the inverse of the radius of the circumscribing circle R_c of the triangle (v_0, v_1, v_2) (see Figure 4.10),

$$R_c = \frac{abc}{4A}$$

with A being the area of the triangle (v_0, v_1, v_2)

$$A = \frac{\sqrt{(b+c)^2 - a^2}.\sqrt{a^2 - (b-c)^2}}{4}$$

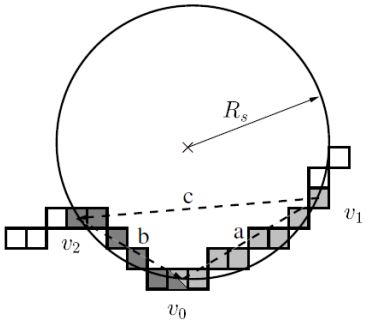

Figure 4.10 *Illustration of the osculating radius formula to approach the curvature estimation (Coeurjolly and Svensson, 2003).*

Figure 4.11a displays a randomly generated curve. By using the osculating formula, we could estimate the local curvature in each point of a curve. In **Figure 4.11**b, the random curve in the xy-plane and the local curvature is plotted on the z-axis. It can be seen that for large radii (straight curve), the curvature is low and for small radii, the curvature is high.

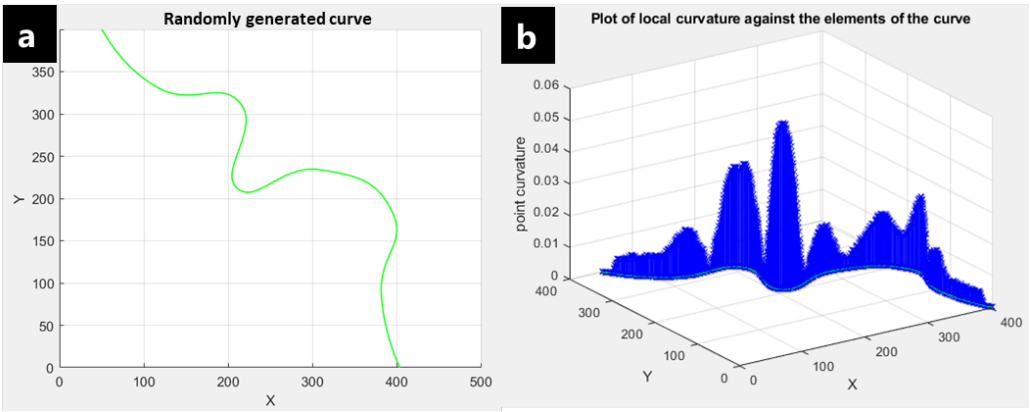

Figure 4.11 *Example of the calculation of the local curvature in each point of a a) randomly generated curve, with b) the corresponding local curvature values for each point along the curve in a).*

Figure 4.8 shows an example of the estimation of the curvature at the EC/HPC interface in a 37 wt% HPC system. First, a background subtraction was done by smoothing the original image with a 2D Gaussian smoothing kernel with high standard deviation (σ = 100 pixels) and subtracting the smoothed image from the original. Second, the resulting image was smoothed with another Gaussian filter (σ = 10 pixels) for noise reduction, see Figure 4.8a (in dark the EC phase and in bright the HPC phase). Third, the image was binarized using thresholding, see Figure 4.8b (in white the EC phase and in black the HPC phase). Fourth, the interfaces were identified and extracted as independent curves. By using the osculating radius formula, the local curvature on each point of the curve can be estimated. Figure 4.8c shows the curvature at the interfaces (the color scale corresponding to the curvature value, yellow indicates high curvature and blue indicates low curvature). Figure 4.8d shows the distribution of the curvature values estimated from all the EC/HPC interfaces in the micrograph. Figure 4.8e is an example of a curve extracted from Figure 4.8c (red square). In Figure 4.8f, the local curvature of the same curve is plotted in the xy-plane.

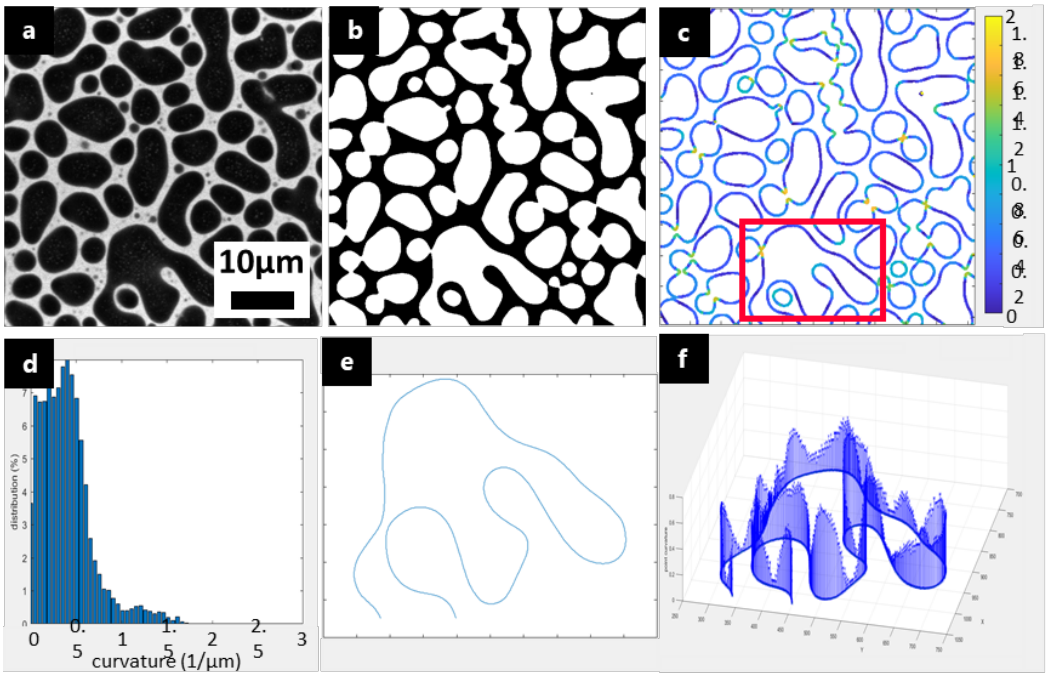

Figure 4.12 *Illustration of the local curvature estimation, showing a) background subtracted and smoothed CLSM micrograph of a film with 37 wt% HPC at 495 s (EC is dark, HPC is bright), b) binarized image (EC is white, HPC is black), c) identification of the interface and calculation of the local curvatures along the interface, d) histogram of the local curvatures, e) example of a single interfacial curve extracted from the micrograph (red square in c)), and f) the corresponding local curvature values for each point along the curve in e).*

5 Results and Discussion

The main aim of this work was to investigate the structure evolution of phase-separated EC/HPC films and to determine the influence of the EC/HPC ratio and the process parameters on the formed structure. After evaluating the feasibility to produce multilayer films using spin-coating, we developed a model for mimicking the industrial pellet production process. By observing the structure evolution and the final structure of monolayer films, we obtained crucial information about the influence of the EC/HPC ratio on the structure evolution. By developing and optimizing an *in situ* experimental set-up, we could determine the different coarsening mechanisms and phenomena involved in the structure formation of monolayer films, and estimate part of the phase diagram. Finally, we extensively studied the multilayer film formation, and proposed a possible explanation for the multilayered structure exhibiting different porosity in the industrial pellets.

5.1 A model system for mimicking the industrial process of fluidized bed spraying

Observing the phase separation *in situ* during fluidized bed spraying raises big challenges. In the fluidized bed, the polymer solution is coated around a pellet. Figure 5.1 shows an illustration of the industrial pellet structure. The core is coated with a drug layer that will be delivered in the body and this layer is coated with a phase-separated EC/HPC film. The porous structure of the EC/HPC film controls the drug release rate. Information about the coating layer can be obtained by analyzing the final dried microstructure of free-standing films or industrially produced pellets.

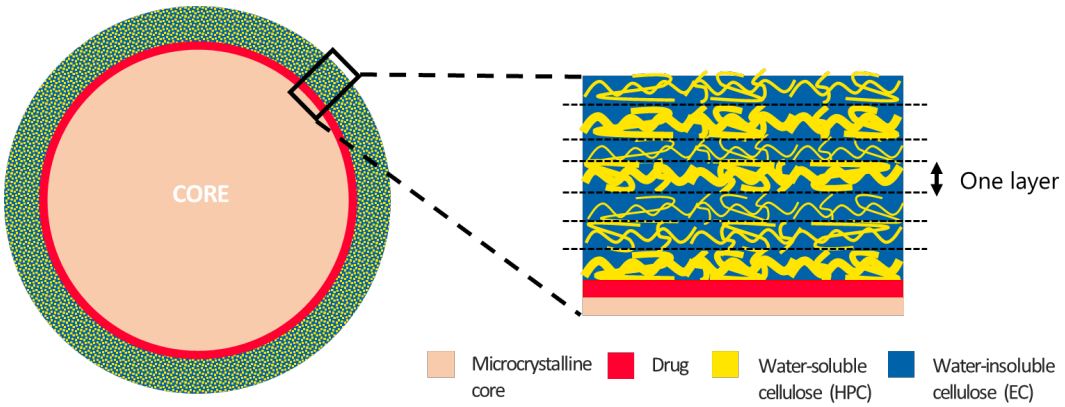

Figure 5.1 *Illustration of the multi-layered phase-separated coating around a pharmaceutical pellet obtained via the industrial process.*

In previous work, the complex structure of EC/HPC pellet coating was imaged using FIB-SEM (Fager *et al.*, 2020a) and CLSM (Gebäck *et al.*, 2015), and was mathematically reconstructed. Image analysis of the coating structure was performed using MIST[1]. Quantitative data, such as porosity, connectivity and tortuosity have been extracted from the 3D reconstructions (Röding

[1] MIST is an open source software that was developed by Barman *et al.* BARMAN, S. 2020. *The pore geometry of pharmaceutical coatings: statistical modelling, characterization methods and transport prediction.* Doctoral Thesis, Chalmers University of Technology.

et al., 2021, Fager *et al.*, 2021a, Fager *et al.*, 2021b). It was found that the structure of the industrial pellets is layered (Fager, 2020), as illustrated in Figure 5.1.
In this work, we wanted to monitor the effect of the composition of the polymer mixture and process parameters on the structure evolution and the final film structure as well as to understand the reason for the layering. The strategy was to find a model to mimic the industrial process of fluidized bed spraying. Our hypothesis is that since the coating in the fluidized spraying device is rather chaotic, the experimental conditions are varying with each passage in the spraying zone, thus influencing the structure of each layer (see section "3.3.4 Industrial process of fluidized bed spraying"). For each passage, at least the following three parameters can influence the porosity: the pellet drying rate, the ethanol content, and the EC/HPC ratio. In the model set-up we were able to change and control the later parameters.
The main elements to reproduce in the model set-up were the production of a thin layer and the homogeneous evaporation of ethanol over the film surface during the fluidized bed spraying process (see section "3.3.4 Industrial process of fluidized bed spraying"). The spin-coating technique meets these requirements and has, therefore, previously been widely used for making uniform polymer films, showing high reproducibility of the film structure. That is why spin-coating was chosen to produce EC/HPC films for our model set-up. Since the structure of the industrial pellet is layered, we also had to examine the practical feasibility of the production of multilayer films via spin-coating.

5.1.1 Development of an experimental set-up to produce multilayer EC/HPC films via spin-coating

The aim of this part of the work was to investigate the feasibility of producing multilayer films by spin-coating, and to identify different layers with CLSM and SEM. Therefore, we decomposed the multilayering and studied step-by-step how a newly coated layer interacts with an already present layer *i.e.* templating and/or redissolution.

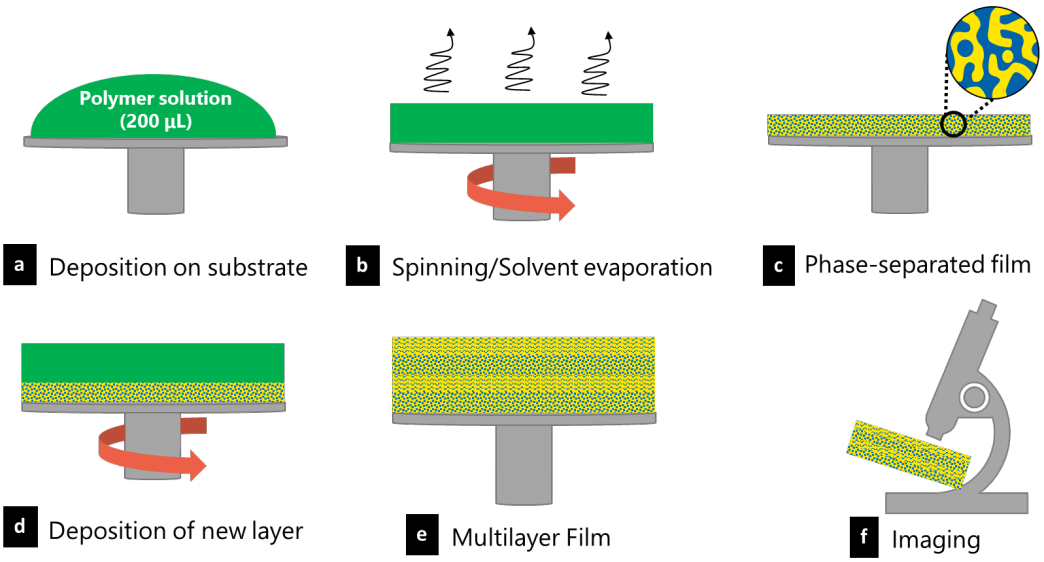

Figure 5.2 *Schematic illustration of the spin-coating process for the production of a multilayer film with a) deposition of the polymer mixture (EC/HPC in ethanol) onto the substrate, b) spinning and solvent evaporation inducing c) phase separation of the film d) we repeat step a and b to form a multilayer film in e). Finally, the film is characterized using microscopy, profilometry and image analysis techniques in f).*

An example of a multilayer film produced using spin-coating is displayed in Figure 5.2 (Ebbens *et al.*, 2011, Heriot and Jones, 2005). First, 200 µL of polymer solution was deposed on a glass petri dish (Figure 5.2a). Then, the system was spun, and the spinning consisted of two steps: 1 min at 2000 RPM to form the film and 4 min at 8000 RPM to dry the layers (Figure 5.2b). After the first spinning, we obtain a first layer of phase-separated EC and HPC (Figure 5.2c). Then, the step is repeated and a new layer is deposited (Figure 5.2d), and so on, until a multilayer film is obtained (Figure 5.2e). Then, the film can be characterized using microcopy and image analysis (Figure 5.2f). Using the multilayer spin-coating procedure with 50 wt% HPC and 100 wt% EC polymer solutions with 29 deposition cycles we obtained the multilayer film displayed in Figure 5.3. The spin-coating sequence is shown in Figure 5.3a, and a CLSM micrograph of the cross-section of the multilayer film in Figure 5.3b. It can be observed that the film exhibits different layers. The structure in the layers with 50 wt% HPC seems overall to be discontinuous and a gradient in structure size can be observed with decreasing size when going from the substrate to the air surface. The thickness of the film for the groups of 5 layers of 50 wt% HPC seems to be constant except for the very first deposited layers.

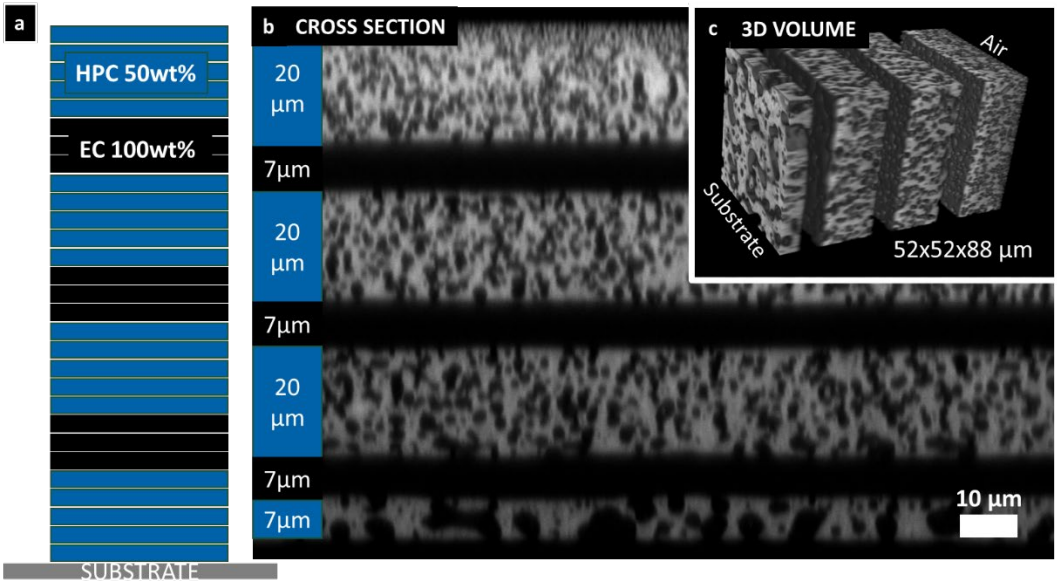

Figure 5.3 *Multilayer EC/HPC film obtained with 29 deposition cycles via spin-coating using a EC/HPC mixture alternating between a mixture with 50 wt% HPC and a mixture with 100 wt% EC with a) the sequence of layers illustrated b) the cross-sectional micrograph with the estimated thickness displayed. c)the 3D reconstruction obtained with Fiji/ImageJ, after imaging a stack of xy images along the z axis. HPC is solid/bright, and EC is hollow/dark.*

We can identify layers in the micrographs in Figure 5.3b and Figure 5.3c and conclude that making a multilayer film by spin-coating is feasible. However, many questions can be raised: What is the effect of the EC/HPC ratio? What is the effect of the spin speed during the spin-coating process? What influences the structure evolution and the thickness of the layers? How can the structure that is obtained by spin-coating be predicted and controlled? Is it possible to produce paths of HPC, which after leaching will form pores, going from the substrate to the air surfaces?

5.1.2 Development of an experimental set-up to characterize with correlative microscopy multilayer EC/HPC films

As explained in the background and experimental sections, the films are meant to be in contact with water so that the HPC will be leached out, resulting in a porous structure. The objectives here were to assess the feasibility of using a combination of spin-coating and complementary microscopy with CLSM and SEM to study multilayer EC/HPC films and to analyze the films before and after leaching.

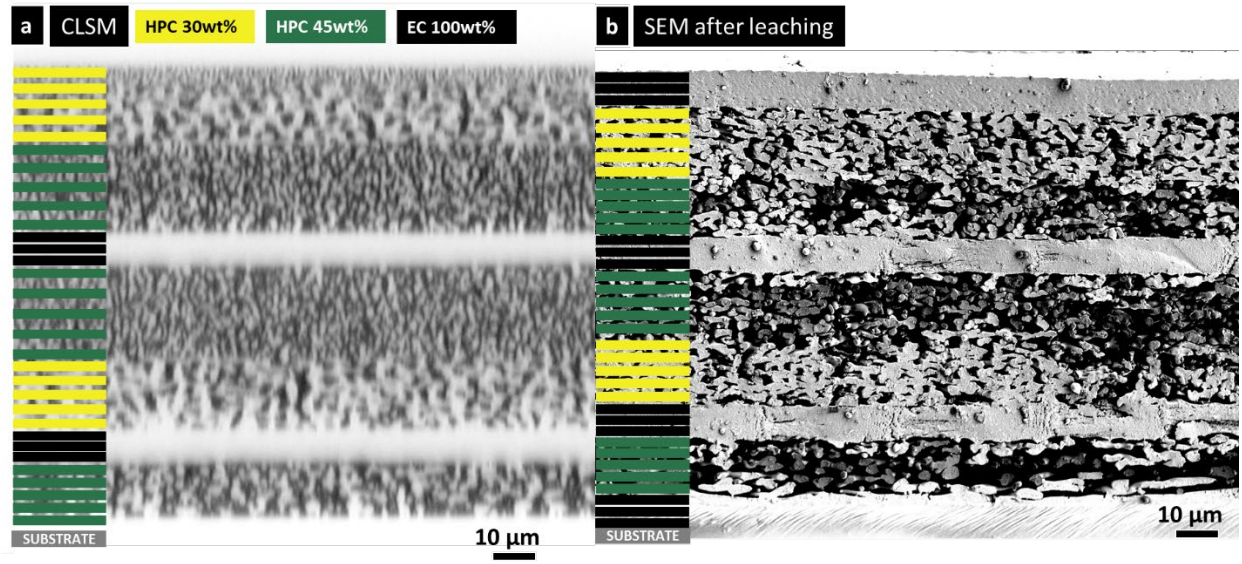

Figure 5.4 *Cross-section of a multilayer film with a) a CLSM-micrograph of a multilayer film with HPC in dark and EC in bright and b) a SEM-micrograph of a similar film cross-section obtained with cryostat after leaching.*

In Figure 5.4, a CSLM micrograph (Figure 5.4a) and a SEM micrograph (Figure 5.4b) of the same film are shown. As in Figure 5.3, we can observe similar layers both in CSLM and in SEM. Because of the cryo-sectioning and the leaching, some structure information might be lost in the SEM micrograph, but on the other hand, higher resolution is reached. Having SEM and CLSM as complementary techniques seems to be a good way to characterize the phase-separated multilayer structure.

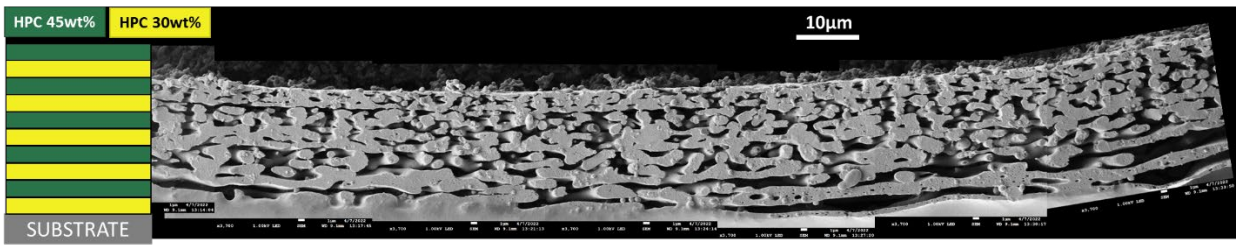

Figure 5.5 *SEM micrograph of a multilayer film cross-section made of 10 alternating layers of 30 wt% and 45 wt% HPC after cryo-sectioning and leaching. EC is solid and HPC is hollow.*

Figure 5.5 shows a porous film made with 10 deposition cycles via spin-coating making 10 alternating layers of 30 and 45wt% HPC. Overall, the film cross-section seems bicontinuous with a continuous matrix of EC (bright) and pores (dark) that are forming paths from the substrate to the air surface. In this micrograph, we assume that templating has occurred between the layers, making the structure arrangement favorable for a bicontinuous film. In this film, we can imagine the drug being able to diffuse through the pores into the surrounding liquids in the body. This is in favor of using the spin-coating technique in our model set-up, since with this technique, we can mimic the film around the drug pellet.

5.1.3 Development of an experimental framework to study the layered film formation

The spin-coating of multilayer films was found to be a good model set-up to mimic the industrial process of pellet coating. The strategy was first to study the structure formation in monolayer films and investigate the kinetics of phase separation and the effect of spin speed and EC/HPC ratio. Secondly, we used this knowledge and experimental optimization to produce multilayer films in a controlled manner in order to understand the layered film formation.
To investigate the structure evolution and the final structure of thin films, an experimental framework was developed, summarized in Figure 5.6. The experimental design involved testing the influence of EC/HPC ratio, spin speed, volume of substrate, spin speed and spin time, on the monolayer and multilayer film formation.

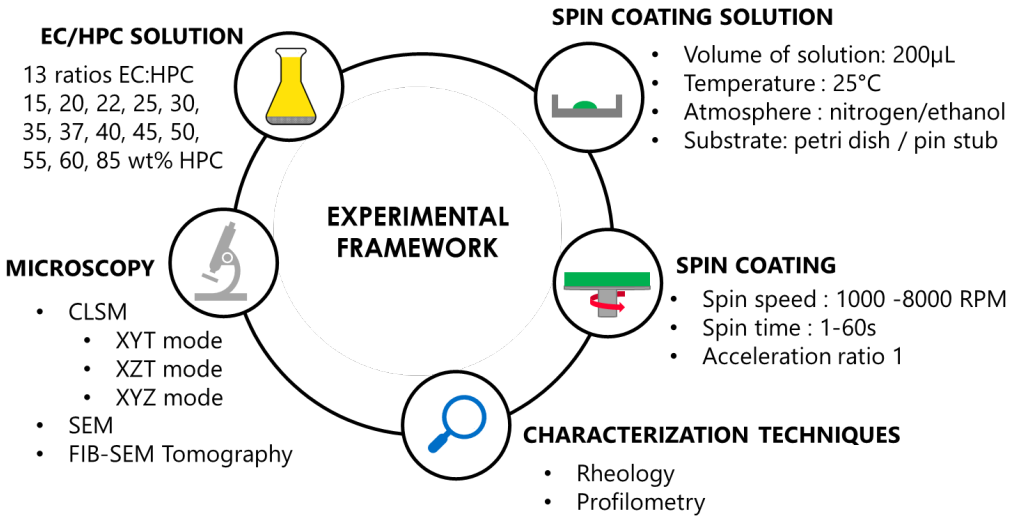

Figure 5.6 *Schematic illustration of the experimental framework of this work, showing the varied and fixed parameters used to investigate the monolayer and multilayer EC/HPC film structure formation.*

Furthermore, it is widely known that the atmosphere, *i.e.* temperature and humidity, has a strong influence on spin-coating results (Mokarian-Tabari *et al.*, 2010, Dandapat *et al.*, 2005) and particularly, on the structure evolution. For example, high temperature can provoke the so-called Marangoni effect (Yiantsios *et al.*, 2015, Fowler *et al.*, 2016) and high humidity can alter the structure formation (Birnie, 2011). That is why, in all cases, the experiments were carried

out in humidity free atmosphere (nitrogen purge) and at 25 °C. The influence of spin speed and spin time on the final structure were investigated. When evaluating the kinetics of the phase separation, spin speed and spin time were fixed at 2000 RPM and 3 s, respectively, and the EC/HPC ratio was the main parameter to be investigated. For CLSM analysis, two modes of observation (xy and xz) were chosen to characterize the 3D structure of the film (so we obtain information in xyz). To reach a higher resolution and to characterize smaller features of the film structure, SEM and FIB-SEM were used. Finally, the viscosity of the polymer mixtures was determined with rheology and the thickness of the films with profilometry.

5.2 Monolayer film formation

To understand the multilayer EC/HPC film formation, the structure evolution in monolayer films were investigated first. Then, the gained knowledge was applied to study the multilayer films. For the monolayer film formation, the influence of spin-speed on the final film structure and film thickness was characterized. To be able to understand the structure evolution, an experimental set-up was developed to slow down the evaporation process and to make the *in situ* CLSM monitoring of the phase separation possible. The influence of the EC/HPC ratio on the time-dependent structure evolution was determined and the coarsening of bicontinuous and discontinuous phase-separated structures was studied. Finally, a novel method for the estimation of the binodal curve of the phase diagram was developed.

5.2.1 Rheology of EC/HPC solutions

The effect of the HPC concentration and the polymer concentration on the viscosity of the polymer solutions was investigated using rheology (**Paper I**). The samples contained 22, 30, 45 and 60 wt% HPC. Furthermore, solutions with different solvent content were investigated to evaluate the increase of viscosity during ethanol evaporation.

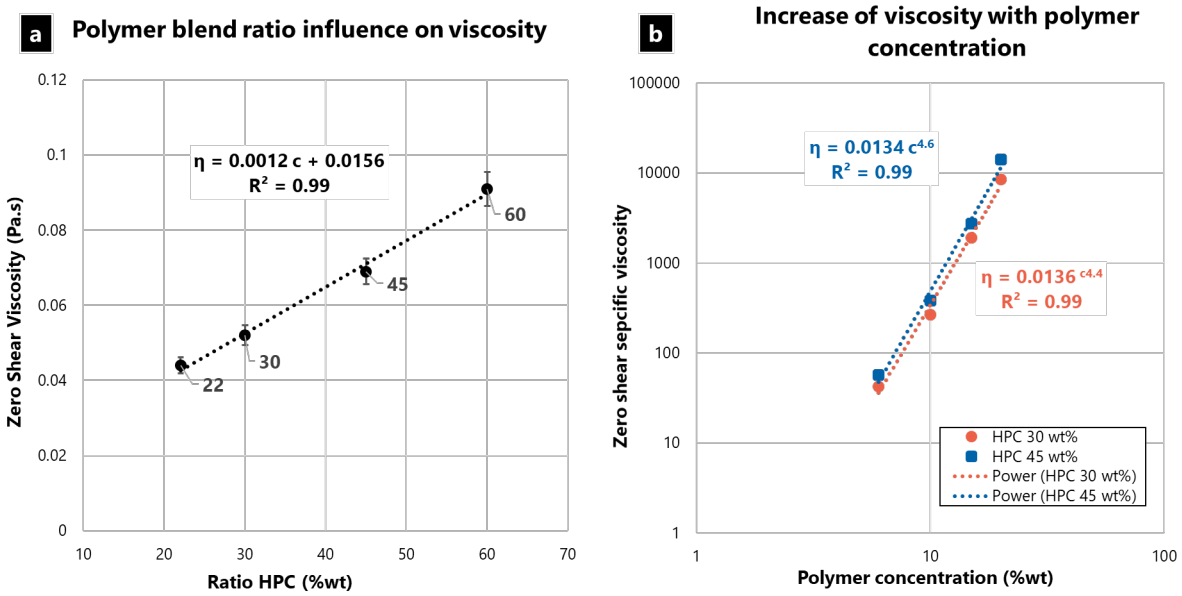

Figure 5.7 *Rheology measurements on the EC/HPC system with a) zero-shear viscosity versus the HPC ratio in the polymer blend (m ± sd) (nb_r=3). The solutions were the stock solutions with 6 wt% polymer in 94 wt% ethanol and b) zero-shear specific viscosity (m ± sd) (nb_r=3) as a function of polymer concentration.*

Figure 5.7a shows the zero-shear viscosity *versus* the ratio of HPC in the polymer blend at 6 wt% total polymer concentration for the four compositions of 22, 30, 45, 60 wt% HPC. The value for the viscosity at zero shear rate was approximated from the viscosity at the Newtonian plateau (Barnes, 2000, Shaw and Macknight, 2005). In Figure 5.7a, the viscosity of EC/HPC solution increases linearly with the increase of HPC fraction in the polymer blend. This result can be explained by the molecular weight of HPC being considerably higher than the molecular weight of EC. The entanglements between the polymer chains are higher when increasing the HPC ratio, resulting in an increase of viscosity (De Gennes, 1979).
Figure 5.7b shows the zero-shear specific viscosity *versus* the polymer concentration. The rheology measurements displayed in Figure 5.7b show that the viscosity is clearly increasing with increased evaporation of ethanol in the solution (*i.e.* increasing polymer concentration). The logarithmic plot of the zero-shear specific viscosity *versus* the polymer concentration was fitted with a power law. For both compositions, 30 and 45 wt% HPC, the viscosity increases in a similar manner: the exponents being 4.4 for HPC 30 wt% and 4.6 for HPC 45 wt%.
The rheological data provided more information about the kinetic trapping: with ethanol evaporation, the viscosity increases drastically, trapping the structure during the phase separation process (Schaefer *et al.*, 2016). The increase of viscosity as a function of increasing HPC ratio that is shown in Figure 5.7a is not so pronounced compared to the high increase of viscosity during evaporation shown in Figure 5.7b. Thus, the main parameters responsible for the kinetical trapping are most likely the total polymer concentration, and the ethanol evaporation rate.

5.2.2 Influence of spin-speed on the structure evolution and film thickness

Here the aim was to determine the effect of different spin-coating parameters on the phase-separated structure. After some testing, the spin time and the acceleration ratio were fixed to 45 s and 1:1, respectively. The effect of spin speed on the final film structure and thickness was investigated (**Paper I**).
Figure 5.8a shows the effect of the spin speed on the film thickness for different compositions. Figure 5.8b shows corresponding CLSM micrographs of spin-coated films at different spin speeds and 30 wt% HPC with the characteristic length scale L, displayed under the CLSM micrographs. It can be seen that the characteristic length scale L is decreasing with increasing spin speed. This suggests that the phase separation (SD followed by coarsening) is stopped in an earlier stage of coarsening at higher spin speed. One possible explanation is that at higher spin speed the evaporation is faster (Birnie and Manley, 1997).
In Figure 5.8a, spin curves were plotted for the compositions 22, 30, 45 and 60 wt% HPC in the polymer blend, *i.e.* the average thickness of the films h is plotted against the spin speed ω. The spin curves were fitted with a power law and the values of the exponent n were determined. It can be seen that the phase-separated polymer film is thinner when the spin speed is higher, *e.g.* $h_{HPC30}(1000\,rpm) = 1.5$ µm and $h_{HPC30}(8000\,rpm) = 0.5$ µm. The increase of centrifugal forces leads to more material being spread out in all directions and hence to a thinner film. There is also a small tendency that the films become thicker when increasing the HPC ratio. A possible explanation could be that the viscosity increases with increasing HPC ratio (refer to section "5.2.1 Rheology of EC/HPC solutions").

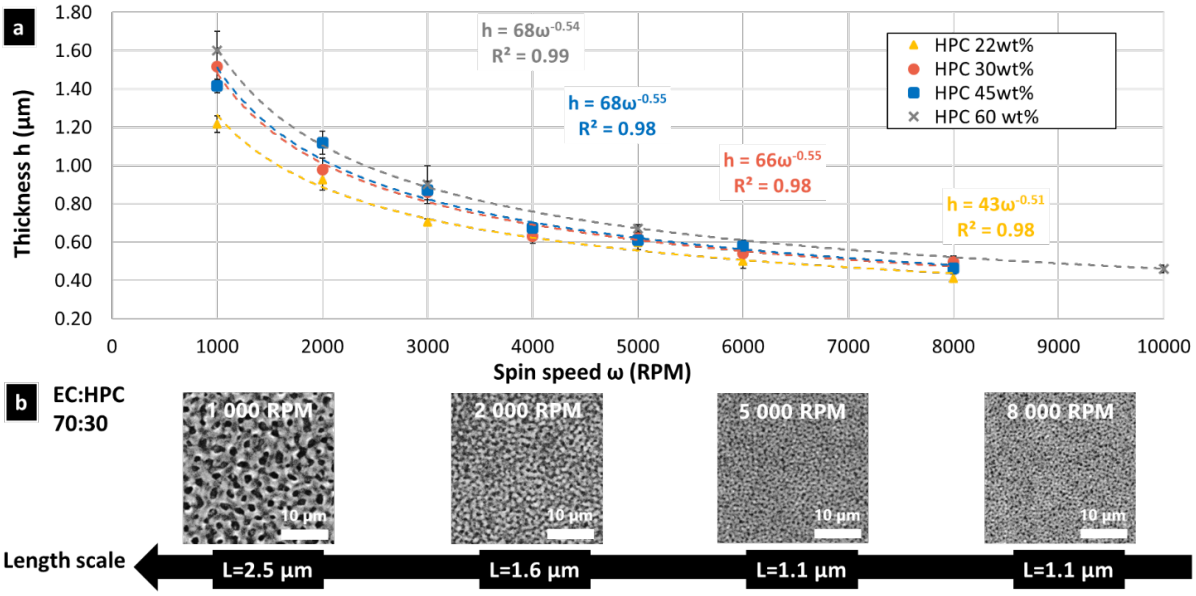

Figure 5.8 *Influence of the spin-coating parameters with a) thickness determined by profilometry versus the spin speeds (m ± sd) (nb_r=3) and b) micrographs of 30 wt% HPC films spin-coated at 4 different spin speed: 1000, 2000, 5000 and 8000 RPM, the corresponding length scale obtained by FFT is displayed. HPC is bright, EC is dark.*

Meyerhofer developed a mathematical model for spin-coated films that relates the film thickness to spin speed, initial viscosity and evaporation rate (Meyerhofer, 1978). In particular, it was shown that the thickness h decreases with increasing spin speed ω according to the relation $h \propto k\omega^{-0.5}$, with a constant k depending on the viscosity, density and concentration of the solution. The fits in Figure 5.8a show that the assumptions made by Meyerhofer leading to the relation $h \propto k\omega^{-0.5}$ are consistent with the experimental data obtained on the spin-coated EC/HPC mixtures (see **Paper I**).

5.2.3 Slowing down the evaporation process for optimized *in situ* CLSM monitoring

The EC/HPC phase separation is governed by the solvent evaporation and the system phase separates when enough ethanol has evaporated to enter the two-phase region in the phase diagram. During the evaporation, the structure becomes kinetically trapped before reaching equilibrium. The evaporation of ethanol in the thin EC/HPC film is relatively fast (in the order of minutes) and the imaging of the structure evolution *in situ* is time-limited due to practical reasons: the sample needs to be moved from the spin-coater to the CLSM, the imaging parameters must be adjusted, the sample has to be put into focus, and the interval between each frame cannot be reduced too much without reducing the signal-to-noise ratio. Therefore, the total time of phase separation before kinetic trapping had to be increased by reducing the solvent evaporation rate. One way to reduce the evaporation rate is to enrich the atmosphere in ethanol by producing the film in a closed environment such as a petri dish with a lid.

The evaporation during EC/HPC film formation in a petri dish was studied by gravimetry and is described in detail in **Paper III**. The results show no significant difference in evaporation rate for HPC 30 wt% and HPC 45 wt% for both closed and open lid. This indicates that the evaporation rate is independent of the polymer blend ratio. After linear regression of HPC 30

wt% data, slopes $m \pm sd$ (standard deviation based on three replicates) of -0.2580 ± 0.0005 and $-2.10 \pm 0.05\, mg/min$ were obtained for the closed and open petri dish, respectively. Hence, the evaporation is slowed down approximately 8 times at room temperature by closing the lid, which can be used to delay the onset of phase separation and to expand the observation window for CLSM analysis of the time-dependent film structure evolution.

5.2.4 Influence of the EC/HPC ratio on the time-dependent structure evolution

The combination of spin-coating in a petri dish, closed directly after spinning, and confocal microscopy allowed us to produce a uniform wet monolayer film, and to follow the phase separation during solvent evaporation. We fixed the spin speed at 2000 RPM and 3s. After spinning, the petri dish was directly closed with a lid. The structure evolution and the final dried structure were investigated, and the different structures were divided into bicontinuous and discontinuous structures. An overview of the influence of the EC/HPC ratio on the in-plane (**Paper II**) and cross-sectional (**Paper III**) structure evolution and possible explanations for the different coarsening mechanisms and phenomena involved in the structure formation are given.

5.2.4.1 In-plane structure evolution in a monolayer film

In this section, we give an overview of the in-plane structure evolution of phase-separated structures taking place in spin-coated EC/HPC thin films (**Paper II**). The main parameter that was varied is the EC/HPC ratio, and 13 different ratios ranging from 15 to 85 wt% HPC were investigated.

Figure 5.9 shows CLSM micrographs of the in-plane film structure evolution for 13 EC/HPC ratios at different key times of the phase separation. The first row corresponds to the stage before the phase separation has started, EC and HPC are in one phase and, the micrographs are grey and homogeneous. The second row corresponds to the phase separation start. Some vague structures can be observed, including white inclusions of HPC in EC matrix for the ratios 15 to 22 wt% HPC, black EC inclusions in HPC matrix for the ratios 45 to 85 wt% HPC, and interconnected structures for the ratios from 30 to 40 wt% HPC. HPC 25 wt% appears to be on the boundary between discontinuous and bicontinuous structures. The third row corresponds to the growth start, where the power fit starting point is taken (see Figure 4 in **Paper II** for a detailed description of the power fit). The fourth row shows the structure during coarsening and the fifth row corresponds to the power fit end where the growth ends. After this point the structure is kinetically trapped, and the growth is more or less stopped. Finally, the sixth row corresponds to the length scale at plateau, when the evaporation process is close to being complete, and almost only solid polymers remain.

It can be noticed that from the third to the fifth row, the structure evolution is noticeably different from the structure on the other rows depending on the ratio EC/HPC. Among the 13 ratios shown in Figure 5.9, we identified three situations: i) bright HPC droplet-like inclusions in a dark EC matrix forming a discontinuous structure, observed for the fractions frtom 15 to 22 wt% HPC; ii) a bicontinuous structure, where the volume fraction of EC and HPC are rather similar and the domains are interconnected, observed for the fractions from 30 to 40 wt% HPC; iii) dark EC droplet-like inclusions in a bright HPC matrix forming a discontinuous structure,

observed for the fractions from 45 to 85 wt% HPC. In the last row of Figure 5.9, the micrographs corresponding to the plateau when the structure is trapped are shown. The characteristic length scale for each micrograph was calculated using image analysis as described in **Paper II.** We observe that the length scale at the plateau is within the same range, $L \sim 0.6 - 1.6\ \mu m$, for the discontinuous structures that correspond to 15, 20, 22, 45, 50, 55, 60, 85 wt% HPC. The fraction 22 wt% HPC is probably close to the boundary between the metastable and the unstable regions (see **Paper II**). HPC 25 wt% appears to be on the boundary between discontinuous and bicontinuous structures. For the bicontinuous structures (30, 35, 37, 40 wt% HPC), the length scale is significantly larger than the discontinuous structure, ranging between 3.0 µm to 6.0 µm. The maximum characteristic length scale is obtained at 30 wt% HPC.

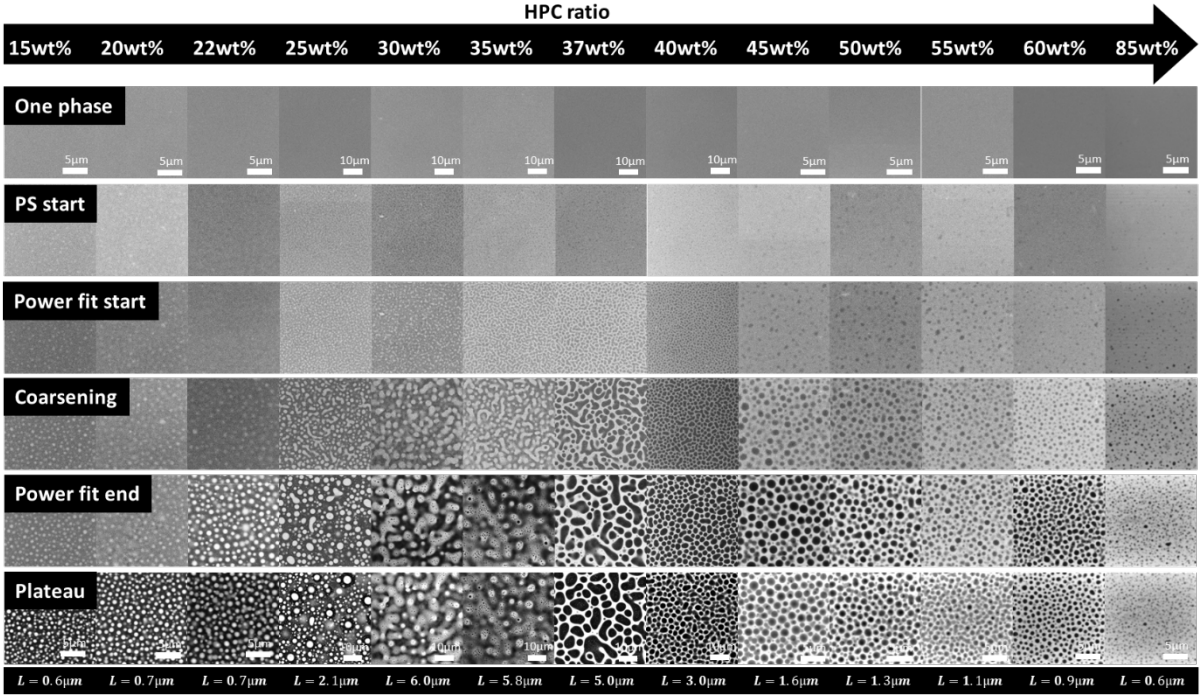

Figure 5.9 *Overview of the structure evolution of EC/HPC films with 13 different EC/HPC ratios. The x-axis is the HPC fraction, and the y-axis corresponds to different key times of phase separation: one phase, the phase separation (PS) starts, the start of structure growth, coarsening during growth, the end of structure growth and finally at plateau, when the structure is trapped. HPC is bright, EC is dark. The length scale at plateau, L, is given in the last row.*

In Figure 5.10, to the right, schematic illustrations of possible structures seen in Figure 5.9 are displayed. On the left in Figure 5.10, an illustration of the corresponding location in the ternary phase diagram is shown. Depending on the path that the mixture follows when moving from the 1-phase to the 2-phase region, and the kinetics, different mechanisms of phase separation and different morphologies are obtained (Bray, 2003, Bray, 2010, Siggia, 1979, Michels, 2011). Figure 5.10 shows an illustration of the structures obtained in Figure 5.9 after phase separation as a function of the EC/HPC ratio and how they can be sorted into different cases: *i)* cases *a* and *b,* when a discontinuous structure with HPC inclusions in an EC matrix is obtained. *a* describes the metastable region, where the structure is formed by nucleation and growth and *b*

the unstable region, where the discontinuous structure is formed by spinodal decomposition followed by PCT. The occurrence of PCT depends on many factors. In the EC/HPC system, the drying kinetics play an important role for the occurrence of PCT. With faster drying kinetics, it is more likely that a bicontinuous structure is formed (see **Paper II** for a more detailed discussion). *ii)* case *c,* when bicontinuous structures are formed by spinodal decomposition and both phases keep percolation. *iii)* cases *d* and *e* with a discontinuous structure of EC inclusions in an HPC matrix. Case *e* is formed by nucleation and growth and *d* by spinodal decomposition followed by PCT. In Figure 5.10 on the right, the difference between *a* and *b* and between *d* and *e is* that the inclusions in *b* and *d* have similar size (probably appearing at the same time) whereas in *a* and *e,* they are of different sizes (probably appearing at different times).

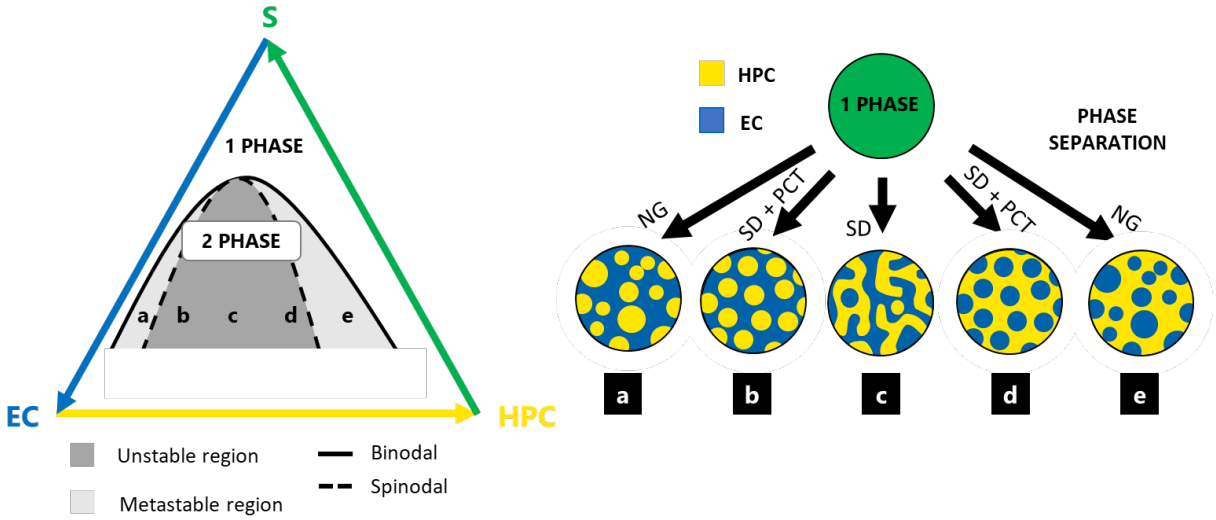

Figure 5.10 *Schematic illustration of the possible structures that can be obtained after phase separation of EC and HPC, showing the ternary phase diagram of EC and HPC in ethanol (left) and some examples a)–e) of possible structures (right); a) and e) are in the metastable region, whereas b)–d) are in the unstable region. Further, c) is bicontinuous whereas the others are discontinuous. NG is nucleation and growth; SD is spinodal decomposition; PCT is percolation to cluster transition.*

Among the cases shown in Figure 5.10, we believe that the HPC fractions from 15 wt% to 20 wt% correspond to case *a*. The structure evolution of 22 wt% HPC indicates that it corresponds to case *b*, which is in accordance with the percolation threshold found by Marucci *et al.* (2009) at 22 wt% HPC (refer to section "3.3.3 EC/HPC systems for drug release"). Below the percolation threshold, HPC inclusions are trapped in an EC matrix from an early stage of the phase separation and cannot be leached out. Hence, the most probable mechanism is nucleation and growth for 15 wt% and 20 wt% HPC, and spinodal decomposition followed by PCT for 22 wt% HPC. 25 wt% HPC is believed to be on the limit of cases b and c, which is consistent with the results shown in Figure 5.9. The bicontinuous structure observed for the HPC fractions from 30 wt% to 40 wt% is formed by spinodal decomposition and correspond to case *c*. For the fractions from 45 wt% to 60 wt% HPC, discontinuous structures are observed with inclusions of similar sizes which are likely formed by spinodal decomposition followed by PCT (case *d*). Finally, due to larger variations in droplet size it is likely that 85 wt% HPC corresponds to case *e*.

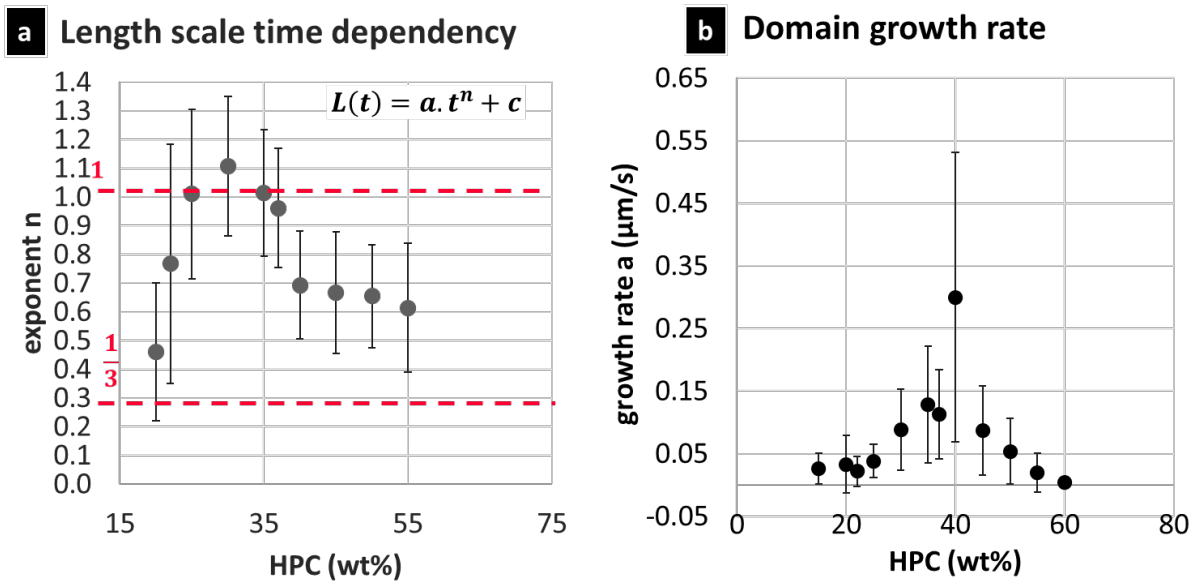

Figure 5.11 *Time dependence analysis, showing a) the exponent n versus the HPC fraction (m ± sd)(3< nb_r<5), also showing two different regimes of coarsening, the diffusive regime (1/3, bottom red dotted line) and the hydrodynamic regime (1, top dotted red line), b) the parameter a corresponding to the domain growth rate versus the HPC fraction (m ± sd)(3< nb_r<5).*

The length scale time dependency during structure growth is defined as $L(t) = at^n + c$, where a is the domain growth rate and n is the time exponent (Tanaka, 2001, Bray, 2003, Bray, 2010). Figure 5.11 shows the length scale time dependency and the domain growth rate of the phase-separated structure. It can be noted that the combination of a and n defines the overall coarsening rate; larger values of both a and n will correspond to a higher growth rate. The parameters a and n were estimated from the data by fitting $L(t)$ to the experimentally obtained length scales, see **Paper II** for the procedure. In Figure 5.11a, for the bicontinuous structures (30, 35, 37 wt% HPC), the time exponent is close to 1, showing that the interfacial tension-driven hydrodynamic coarsening is dominating (Siggia, 1979). For the discontinuous structures, the exponents are lower and closer to $1/3$, showing that the diffusive regime is having an important role in the coarsening (see **Paper II** for detailed discussion about the exponents).
In Figure 5.11b the domain growth rate a is plotted *versus* the HPC ratio. The bicontinuous structures exhibit a higher domain growth rate ($a > 0.05$ µm/s), indicating that the systems coarsen faster than the discontinuous structures. With a higher domain growth rate, it is likely that the final structure will exhibit a larger length scale. These results are in accordance with the results shown in Figure 5.9, where the length scales are larger for the bicontinuous structures than for the discontinuous ones. On the contrary, the circular shapes in the discontinuous structure, mainly formed by diffusion-driven coarsening, are growing at a slower rate ($a <$ 0.05 µm/s) and exhibit smaller length scales. Finally, it can be noticed that 40 wt% HPC has the highest domain growth rate, supporting a bicontinuous structure in this case.

5.2.4.2 Cross-sectional structure evolution in a monolayer film

In the previous section, we studied the in-plane structure evolution. However the final film used in the drug delivering pellets is a 3D structure (Fager, 2020). To assess the 3D structure and to understand fully the structure evolution during phase separation, the monolayer films were observed in the cross-sectional plane (xz-plane) (**Paper III**).
Figure 5.12 shows CLSM-micrographs corresponding to the cross-sectional structure evolution of a monolayer film for the 13 EC/HPC ratios at different key times of the phase separation.

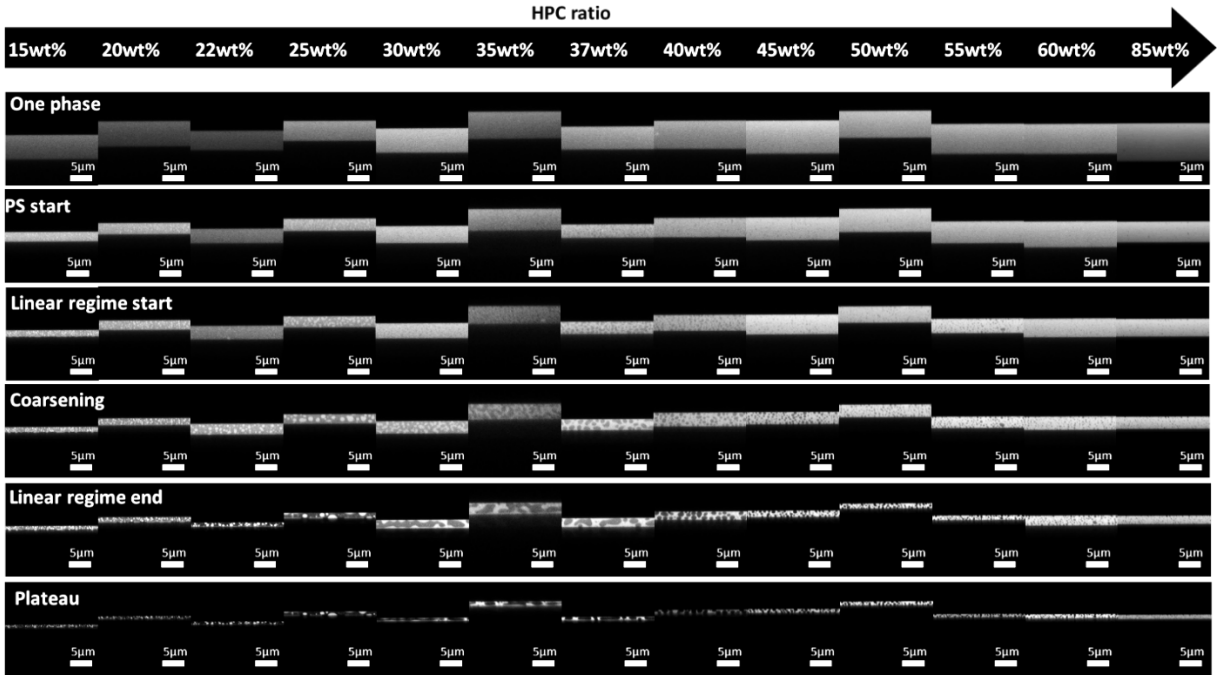

Figure 5.12 *Overview of the cross-sectional structure evolution in EC/HPC films with 13 different EC/HPC ratio. The x-axis is the HPC ratio, and the y-axis corresponds to the different key times of phase separation: one phase, the start of phase separation, the start of the linear fit, during the linear regime (coarsening, at the end of the linear regime and finally at plateau, when the shrinkage has ended. HPC is bright, EC is dark.*

The first row corresponds to the one-phase stage before the phase separation has started. In this stage, EC and HPC are miscible and the CLSM micrographs show a homogeneous mixture. The second row represents the phase separation start and some vague structures can be observed, including bright inclusions of HPC in the EC matrix for 15,20 and 22 wt% HPC, dark EC inclusions in the HPC matrix for 45,50,55,60 and 85 wt% HPC, and interconnected structures for 30,35,37 wt% HPC. The third row corresponds to the growth start, and the start of the linear regime of the shrinkage. The fourth row shows the structure during coarsening. The fifth row is the 'linear regime end'. After this point, the structure is kinetically trapped, the coarsening is stopped, and only shrinkage is observed. Finally, the sixth row corresponds to the structure at plateau, when the evaporation process is nearly complete, and more or less only dried polymers remain. During solvent evaporation of the films in Figure 5.12, the thickness of the films is decreasing as a function of time. It can be noticed from the third to the fifth column that the structure evolution is noticeably different depending on the EC/HPC ratio. The type of morphology of the phase-separated structures in the cross-sectional view is in accordance with previous in-plane observations in Figure 5.9 and in **Paper II**. Additionally, the length scale of

the structures at the plateau Figure 5.12 is significantly larger for the bicontinuous structures that for the discontinuous structures which is in accordance with the previous results shown in Figure 5.9 and in **Paper II**.

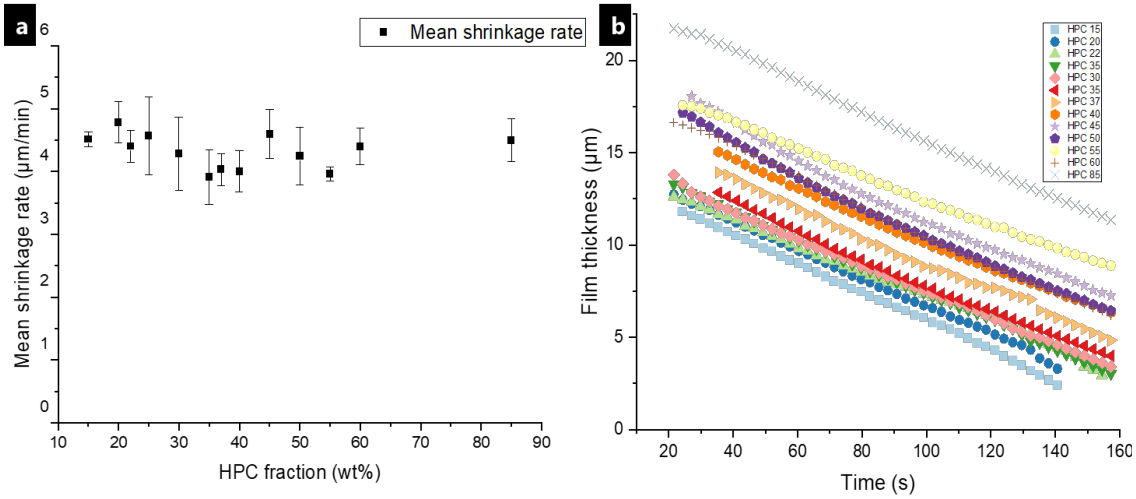

Figure 5.13 *a) Mean shrinkage rate (m ± sd) (3< nb_r<5) during the linear regime calculated for the 13 EC/HPC ratios with b) an example of one replicate for each ratio showing the linear regime.*

The difference between the shrinkage rates for the different EC/HPC ratios, was investigated (see **Paper III**). Figure 5.13 shows the mean shrinkage rates in the linear regime for all 13 EC/HPC ratios. Figure 5.13a shows the mean value obtained by averaging the replicates while Figure 5.13b displays one replicate per EC/HPC ratio. A Tukey's multiple comparison test (Keselman and Rogan, 1977) was used to test the pairwise differences in the mean shrinkage rate between the HPC fractions. None of the differences was significant (all p-values for the pairwise comparisons were > 0.05; the lowest being p ≈ 0.3). This is in accordance with Figure 5.13b, where the slope of the shrinkage in the linear regime is the same for all the ratios. Our hypothesis is that the shrinkage rate is independent of the HPC fraction and mainly depends on the evaporation process. This is also supported by the results of the gravimetric evaporation study, where no significant difference in shrinkage rate between HPC 30 wt% and HPC 45 wt% was observed (see **Paper III**).

5.2.4.3 Curvature evolution during phase separation

To investigate hydrodynamic coarsening, we evaluated the curvature evolution. A novel image analysis method was developed to assess the time-dependent curvature changes (refer to section "4.6.2 Curvature map of the interface between EC and HPC"). It was seen in Figure 5.11 that the time exponent of the film formation for bicontinuous structures were close to 1, which is a strong indication for hydrodynamic coarsening being dominating.

Figure 5.14 shows the time-dependent evolution of the mean curvature (average of three replicates) for the bicontinuous structures (30 – 40 wt% HPC) and for 25 wt% HPC. It can be seen that the mean curvature in Figure 5.14a in the early stage of phase separation (t =100 –

120 s) is high for all the ratios (in the range 0.8 – 0.9 μm^{-1}), signifying that the growing interfaces exhibit small radii. Figures 5.14b and c show two examples of the curvature evolution for 25 wt% HPC and 35 wt% HPC, respectively. Typically, the curvature decreases and the shape of the structure changes rapidly between 140 and 200 s, and at about 250s a plateau is reached due to the kinetic trapping of the structure. This behavior is observed for the ratios 30, 35, 37 and 40 wt% HPC, for which the structure is bicontinuous. For 25 wt% HPC, displayed in Figure 5.14a and b, the drop of curvature is less pronounced. This is in accordance with the observation that the fraction 25 wt% HPC is at the limit between bicontinuous and discontinuous (limit between cases b and c in Figure 5.10). It appears that for HPC 25 wt%, the phase separation takes place through spinodal decomposition creating a bicontinuous structure. This structure first grows through self-similar growth and hydrodynamic coarsening (giving rise to the exponent n close to 1 in Figure 5.11). Then in the end, slightly before kinetic trapping, the PCT occurs resulting in the discontinuous structure observed in Figure 5.9, in the curvature map in Figure 5.14b, and in the plateauing of the mean curvature reduction observed in Figure 5.14a.

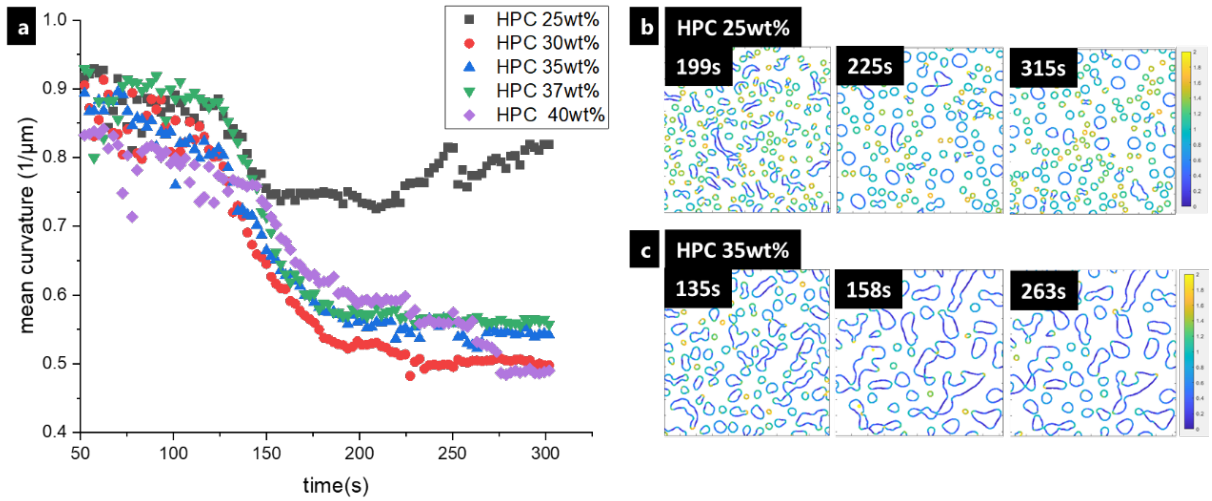

Figure 5.14 *a) Mean curvature versus time for the fractions 25, 30, 35, 37, 40 wt% HPC. ($m \pm sd$) ($3 < nb_r < 5$) and corresponding curvature map during phase separation with the corresponding color scale to the right with b) 25 wt% HPC and c) 35 wt% HPC*

These clearly show that the growth of the bicontinuous structures in phase-separated EC/HPC systems is governed by interfacial tension-driven hydrodynamical coarsening.

5.2.5 Coarsening of bicontinuous and discontinuous phase-separated structures

From the previous sections we saw that, in our model set-up, the phase separation of EC/HPC could give rise to two types of structures, bicontinuous and discontinuous. The bicontinuous structures are formed by SD while the discontinuous structures are formed by NG or SD followed by PCT. In this section, we will describe and summarize the findings by comparing the two coarsening types. Details can be found in **Paper II**, and **Paper III**. The denotations bicontinuous and discontinuous structure will be used later to characterize multilayer films.

5.2.5.1 *Coarsening of bicontinuous structures*

For the bicontinuous type structures, the structure evolution in a 37 wt% HPC monolayer film, is shown in Figure 5.15 as an example. Figure 5.15a is displaying four CLSM micrographs corresponding to the in-plane structure evolution of an interconnected pattern, typical for spinodal decomposition. Figure 5.15b is showing the corresponding curvature at the interface between EC and HPC. Figure 5.15c is the corresponding curvature distribution. Figure 5.15d is displaying four CLSM micrographs in the xz-plane showing the cross-sectional structure evolution and the estimation of the thickness (denoted by h). Note that the upper surface is the glass surface, and the lower surface is the air surface.

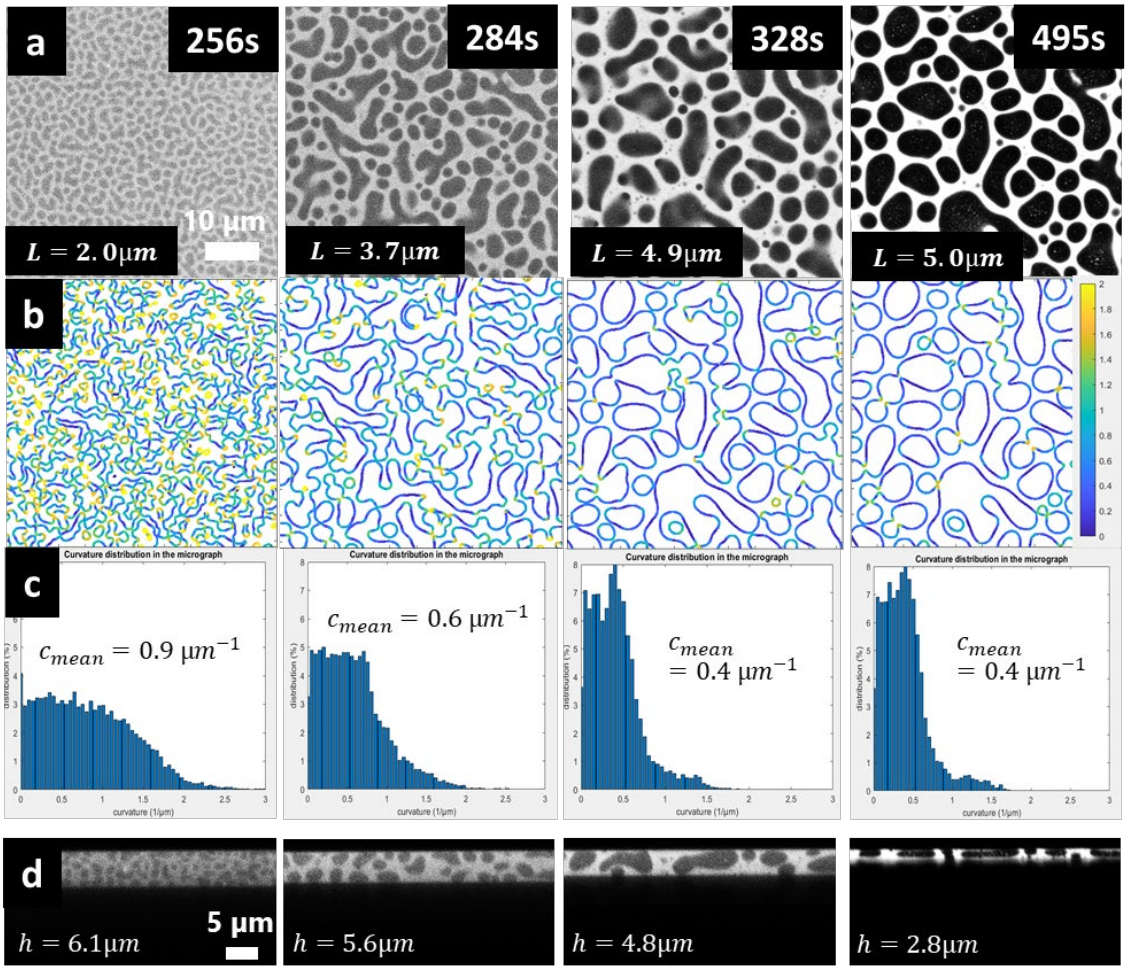

Figure 5.15 *Structure evolution during phase separation of a monolayer EC/HPC thin film with 37wt% HPC that leads to a bicontinuous structure. Example of a monolayer film with 37 wt% HPC. a) CLSM in-plane xyt micrographs with the length scale calculated with FFT image analysis; b) interface identification and curvature calculation, with the corresponding color scale on the right with c) the corresponding curvature distribution and the mean curvature d) CLSM cross-sectional xzt micrographs with the thickness calculated with image analysis. The upper surface is the glass surface, and the lower surface is the air surface. HPC is bright, EC is dark.*

The length scale shown in Figure 5.15a is increasing over time. The first micrograph at 256 s corresponds to an intermediate stage of the spinodal composition. The second micrograph at

284 s corresponds to the coarsening phase, the length scale has increased from 2.0 µm to 3.7 µm. At plateau (495 s), the structure is trapped and almost all the ethanol has evaporated, the characteristic length scale is about 2.5 times the initial length scale. It can be observed that at 328 s (third image from the left), the length scale *L* is nearly equal to the thickness *h*. We believe that after this point, the coarsening is mainly taking place in 2D, not in 3D. After trapping, the structure can still shrink in the z direction. The changes of curvature during phase separation in Figure 5.15b and Figure 5.15c show that the structure is shifting from having high curvature to having low curvature, *e.g.* the mean curvature at early stage is changing from $c_{mean}(t = 256s) = 0.9\ \mu m^{-1}$ to $c_{mean}(t = 495s) = 0.4\ \mu m^{-1}$ at plateau. When the curvature changes in this manner it implies that the coarsening is interfacial tension driven and that the main mechanism of coarsening is hydrodynamic growth (see also section 3.2.4 Coarsening of phase-separated structures and time dependency).

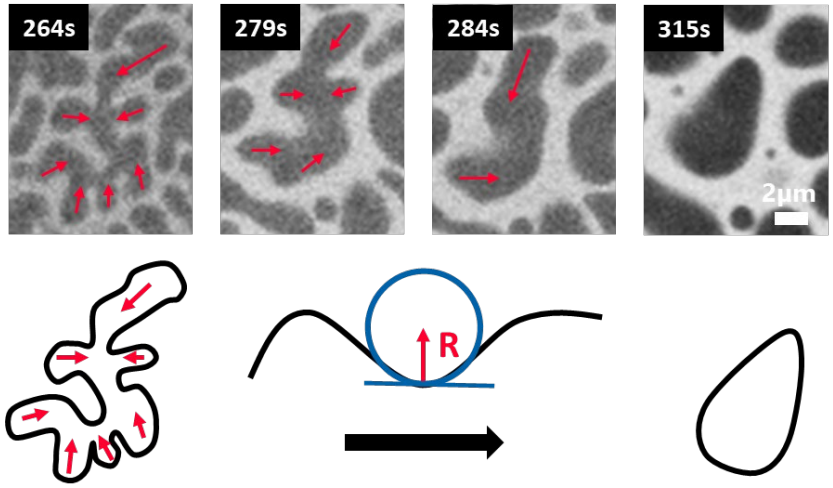

Figure 5.16. *Typical hydrodynamic growth during coarsening of 37 wt% HPC. HPC is bright, EC is dark. The Laplace pressure gradients that cause the Poiseuille flow and the hydrodynamic growth are indicated (red arrows). At the bottom, schematic illustration of the hydrodynamic growth and representation of the curvature, with R the radius of curvature, R_{mean} the mean radius of curvature and c_{mean} the mean curvature.*

The series of CLSM micrographs in Figure 5.16 is showing an example of a time-dependent structure evolution in a bicontinuous structure with 37 wt% HPC. The structure evolution is typical for the hydrodynamic growth mechanism. In the middle of the first micrograph at 264 s, a large dark EC domain with arms attached to a central body is shown. The interfacial curvature is high in the arms, which corresponds to higher Laplace pressure. The red arrows in the CLSM micrograph at 264 s represent the Laplace pressure gradients from the arms to the center causing a Poiseuille flow. Thus, EC is flowing from the arms to the center as we can observe in the series of micrographs from 264 s to 315 s. At the end of the coarsening, the interfacial curvature has decreased. Similar coarsening behavior can be seen for several domains in the bicontinuous structure evolution in Figure 5.9. Similar behavior has been found also in other systems: Bouttes *et al.* (2015) observed hydrodynamic coarsening for silicate melt

and noticed the similar changes of curvature over time caused by flow from regions with high curvature towards the regions with low curvature.

5.2.5.2 Coarsening of discontinuous structures

In discontinuous structures, inclusions of either HPC or EC domains appear and grow in a matrix enriched in the other polymer. In the previous section we observed that the discontinuous structures could be originated from nucleation and growth or spinodal decomposition followed by PCT. For the discontinuous structure type, an example of the structure evolution in a 60 wt% HPC monolayer film is shown.

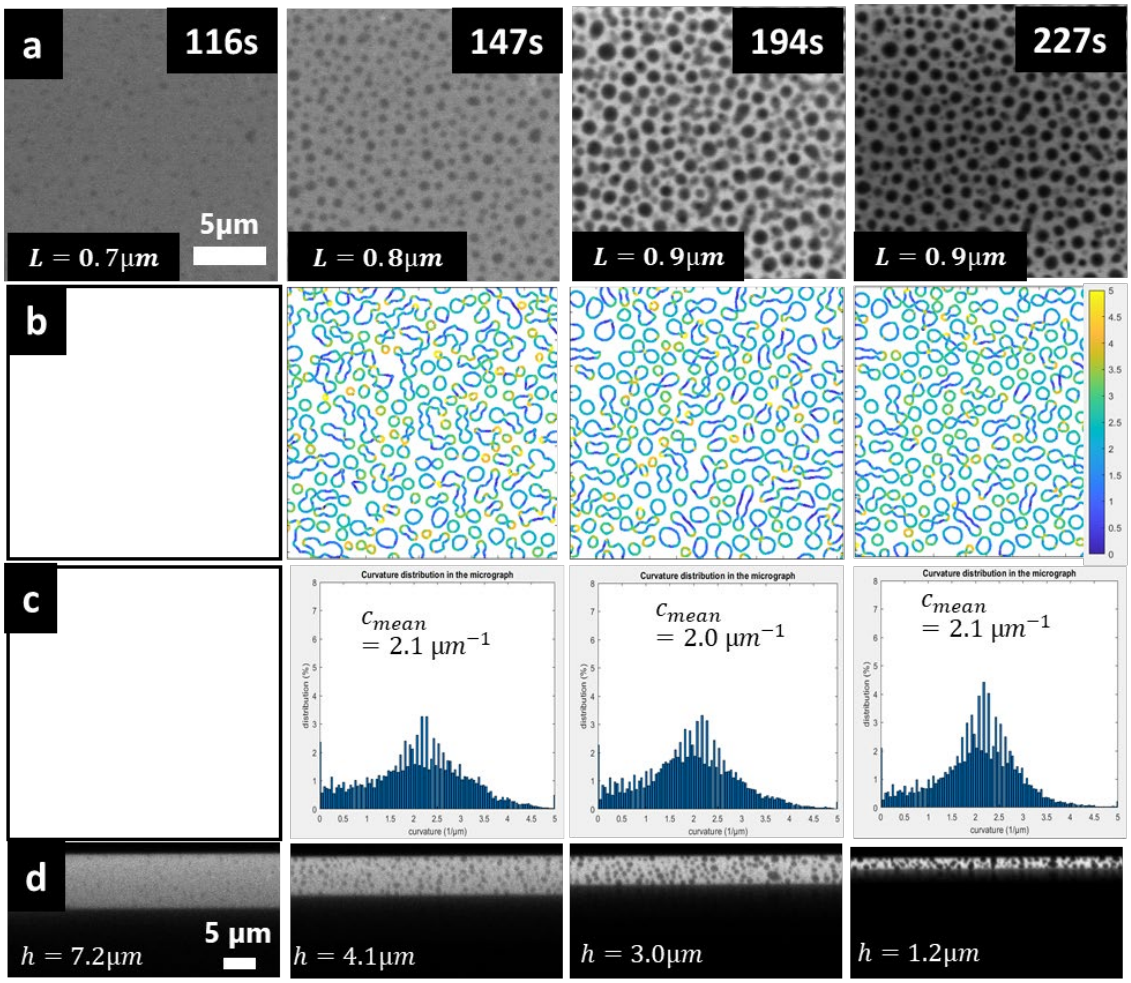

Figure 5.17 *Structure evolution during phase separation of a monolayer EC/HPC thin film with 60wt% HPC that leads to a discontinuous structure. a) CLSM in-plane xyt micrographs with the length scale calculated with image analysis b) interface identification and curvature calculation, with the corresponding color scale on the right with c) the corresponding curvature distribution and the mean curvature d) CLSM cross-sectional xzt micrographs with the thickness calculated with image analysis. The upper surface is the glass surface, and the lower surface is the air surface. HPC is bright, EC is dark.*

Figure 5.17 is showing the structure evolution of a thin film with 60 wt% HPC during phase separation. Figure 5.17a is displaying four CLSM micrographs corresponding to the structure evolution of a typical discontinuous pattern with EC inclusions in a continuous HPC phase.

Figure 5.17b is showing the corresponding curvature at the inclusion interfaces. Figure 5.17c is displaying the corresponding curvature distribution. Finally, Figure 5.17d is showing four CLSM micrographs in the cross-sectional plane, which display the structure evolution and the estimated film thickness. It can be observed in Figure 5.17a that the discontinuous structure is growing over time. In the early stage of phase separation ($t = 116\ s$), EC inclusions start to appear, and while keeping their circular shape they grow over time, *e.g.* the mean diameter is $D = 0.7\ \mu m$ at early stage compared to $0.9\ \mu m$ at plateau. To determine the length scale L, we used image analysis to estimate the diameter of the circular shapes. Because the structure is keeping its circular shape the curvature is not evolving so much, as seen in Figure 5.17b and Figure 5.17c are displaying, even if the size of the inclusions are increasing slightly.
Figure 5.17d is showing the film evolution on the cross-sectional plane. It confirms that the structure is discontinuous also in the depth direction, and that the EC inclusions are spherically shaped. It can be noticed that the diameter of the inclusions is generally smaller than the film thickness during the whole experiment. At $h = 3.0\ \mu m$ and $t = 194s$ the structure is kinetically trapped and does not grow further. However, shrinkage can be observed between the micrograph in Figure 5.17d from $h = 3.0\ \mu m$ to $h = 1.2\ \mu m$ showing that the structure growth is trapped before the evaporation is complete. We believe that at this point the viscosity of the mixture is so high that the mobility of the phases is heavily retarded, and only evaporation and shrinkage is observed.

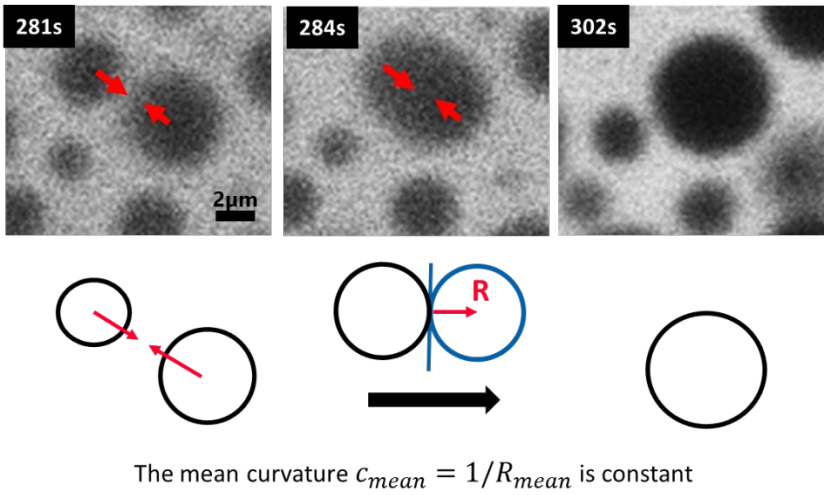

Figure 5.18 *Typical coalescence observed during phase separation of 45 wt% HPC. HPC is bright, EC is dark. At the bottom, schematic illustration of the hydrodynamic growth and representation of the curvature, with R the radius of curvature, R_{mean} the mean radius of curvature and c_{mean} the mean curvature.*

In Figure 5.18, three CLSM micrographs at 45 wt% HPC were selected to show an example of structure evolution that takes place during coarsening in discontinuous structures. After the PCT, the structure can grow through coalescence and/or Ostwald ripening. At $t = 281s$, two dark EC inclusions start to move towards each other (indicated by red arrows) and finally coalesce at $t = 302s$, which increases the inclusion size. This type of coarsening mechanism is typically observed in discontinuous structures. The initial and final states are structures with circular inclusions.

5.2.6 Estimation of the ternary phase diagram

In the following part, we developed a new method to estimate the binodal curve in the phase diagram of a ternary mixture. We used the information from the cross-sectional micrographs and the profilometry to assess the ethanol content at each time of the phase separation and to estimate the position of the binodal curve in the EC/HPC/EtOH ternary phase diagram. It was assumed that the evaporation process is complete after one week of drying. Hence the thickness over time is providing information about the ethanol fraction for each micrograph: the mean volume fraction of solid material is given by the final thickness divided by the current thickness: $\varphi_S(\mathrm{t}) = h_{dry}/h(t)$ and the fraction of ethanol is $\varphi_{EtOH}(\mathrm{t}) = 1 - \varphi_S(t)$ (van Franeker *et al.*, 2015) (**Paper III**).

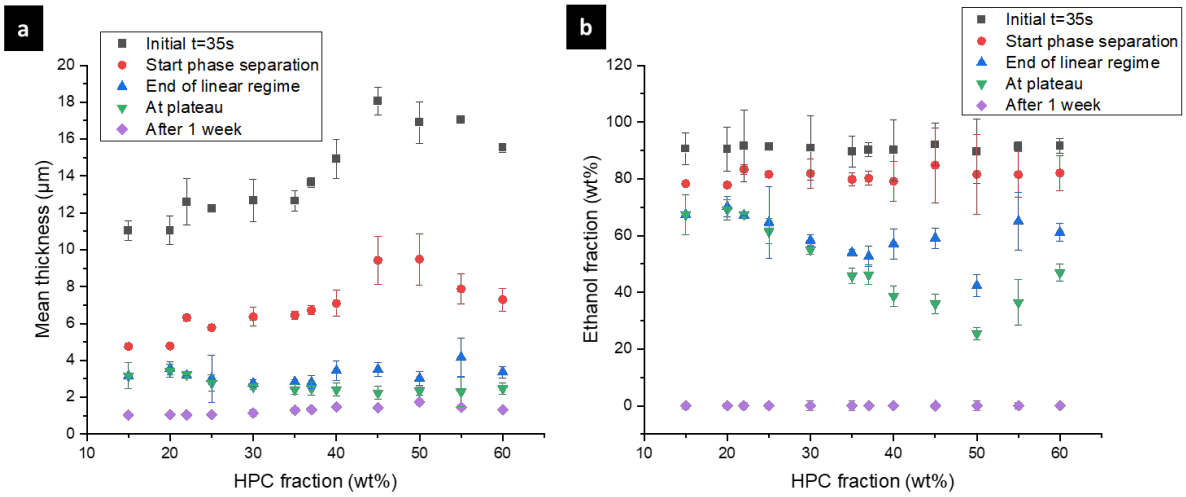

Figure 5.19 *a) Mean thickness (m ± sd) (3< nb_r<5) versus the HPC fraction at key times of the phase separation process b) Ethanol fraction versus the HPC fraction (m ± sd) (3< nb_r<5), assuming that after one week the ethanol fraction is 0 wt%.*

Figure 5.19 shows the film thickness and the ethanol fraction versus the HPC fraction for different key times of the phase separation. In Figure 5.19a, the thickness during shrinkage of the film follows the same trend as observed in the previous sections, where the mean thickness is increasing with the HPC fraction. From the thickness estimation, the ethanol fraction is estimated and plotted in Figure 5.19b. Given the information in Figure 5.19, we can estimate the position of the binodal curve in the ternary phase diagram EC/HPC/EtOH.

Figure 5.20 is showing the estimated phase diagram. The blue curve corresponds to the binodal curve determined experimentally in the previous work by Baderstedt *et al.(2011).* They studied the phase separation in EC/HPC solutions by letting EC/HPC mixtures of different compositions rest in closed vials for at least one month. By visual inspection of the meniscus, they could determine at which composition the mixture would phase separate and hence estimate the binodal curve. The red dots are the estimated positions of the binodal curve according to our work. We note that the estimated location of the binodal curve is in accordance with the one found by Baderstedt *et al.,* which supports that our method can be used to estimate the location of the binodal curve of EC/HPC/EtOH at room temperature. In **Paper III**, the limitations of this method for the estimation of the binodal curve are discussed.

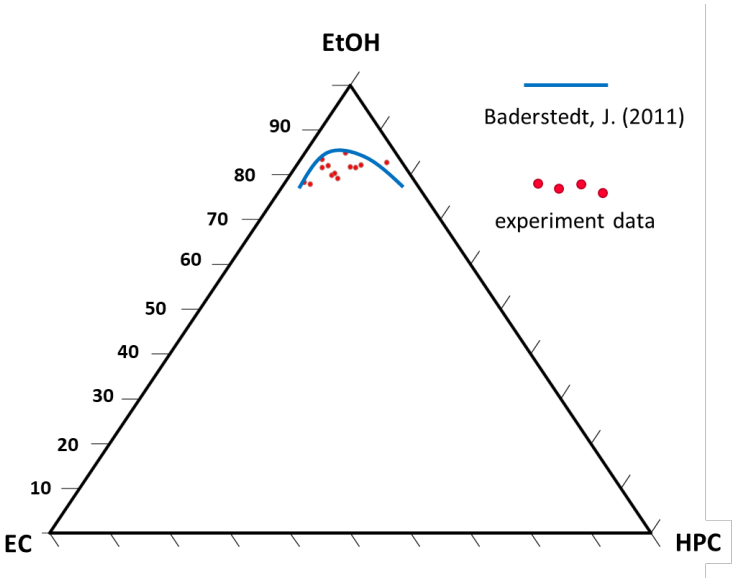

Figure 5.20 *Estimated phase diagram of EC/HPC in EtOH, showing the binodal curve from Baderstedt et al. (2011) (blue solid line) and the binodal curve estimated from the cross-section height in the CLSM micrographs (red dots).*

5.3 Multilayer film formation

Two major aims of this thesis were to mimic the production of a multilayer film and to understand the structure evolution when the layers interact. In the previous sections, spin-coating was used to deposit a monolayer of EC/HPC on a glass substrate and the development of the phase-separated structure was characterized. The effect of the spin-coating parameters was investigated (**Paper I)** and the influence of the EC/HPC ratio on the structure evolution during phase separation in monolayer films was extensively discussed (**Paper II** and **Paper III**). In this part, we characterized the influence of the EC/HPC ratio and the spin speed on the final structure of the multilayer films. In addition, we also investigated the phenomena induced by the deposition of a new layer onto an already present multilayer film. During the coating of successive layers, layers will interact, and the goal was to investigate these interactions. One of our hypotheses is that by coating successive layers, the system might undergo what we call a templating and a redissolution.

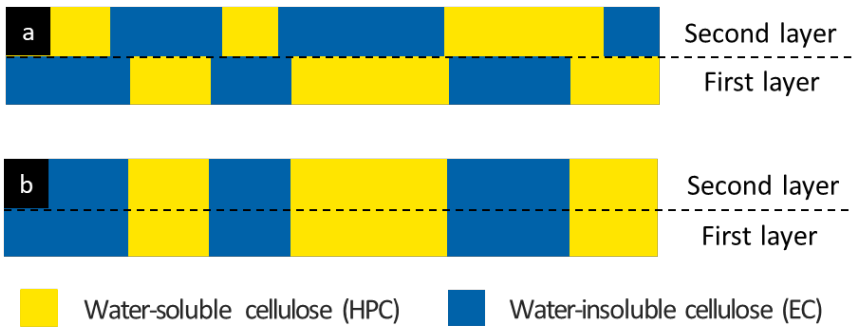

Figure 5.21 *Schematic illustration of the templating effect a) no templating effect between the first and the second layer b) templating effect between the first and the second layer.*

An illustration of the templating effect is given in Figure 5.21. In Figure 5.21a, the second layer is formed, and the pattern (alternation of EC and HPC domains) is independent of the first layer

pattern. In Figure 5.21b, templating is shown. During templating, the large affinity of HPC to HPC and EC to EC is making the structure of the second layer similar to the first layer.
The redissolution effect takes place when a layer of wet solution is entering in contact with dried material underneath (already dried and layered). The ethanol contained in the wet layer dissolves some of the dried EC/HPC and the dissolution is likely to change the structure.

5.3.1 Films with constant EC/HPC ratio and constant spin speed.

In the following section, we compare the effects of the spin-coating parameters and the EC/HPC ratio on the structure of monolayer and multilayer EC/HPC films produced by spin-coating.
Figure 5.22 displays four 8-layer films produced using 4 different experimental conditions. The four films were obtained through the spin-coating process as explained in section 2.2 and **Paper IV** with either 30 wt% or 45 wt% HPC and spun at either 2000 or 8000 RPM.

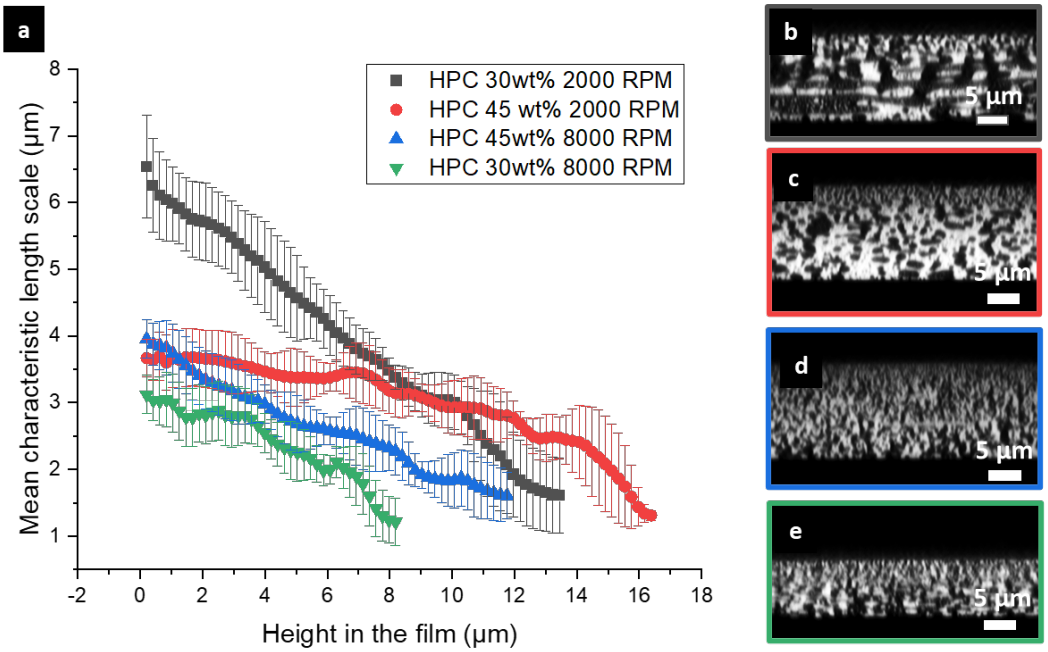

Figure 5.22 *Influence of EC/HPC ratio and spin speed on multilayer films with 8 layers. a) the characteristic length scale (m ± sd) (nb_r=3) in the film as a function of height for the 4 conditions. The characteristic length scale was obtained with Fourier image analysis. The micrographs in b - e) show the corresponding CLSM-cross-sections with b) 30 wt% HPC 2000 RPM, c) 45 wt% HPC 2000 RPM, d) 45 wt% HPC 8000 RPM and e) 30 wt% HPC 8000 RPM. The bottom part in the CLSM micrographs is the surface to the substrate and the top part is the surface to the air. HPC is bright and EC is dark.*

By examining the thickness of the film, it is possible to observe the influence of both the HPC fraction and the spin speed on the thickness of the film. The overall thickness of the multilayer films is increasing with increasing HPC fraction and decreasing spin speed. This is in accordance with the results found in section "5.2.2 Influence of spin speed on the structure evolution and film thickness", where we could estimate the spinning curves of the EC/HPC system showing that with higher spin speed, thinner film and shorter length scale was obtained. The viscosity measurement of EC/HPC solutions made in **Paper I** showed that the viscosity

was increasing with increasing HPC fraction and indeed, in Figure 5.22 it can be seen that the thickness of the film increases with increasing HPC fraction.
Figure 5.22a also shows the mean characteristic length scale at different heights in the sample obtained by Fourier image analysis. The image analysis was performed on the in-plane micrographs (one micrograph every 0.21 µm in the sample as described in **Paper I)**. Figures 5.22b, c, d, and e show cross-sectional micrographs of one of the film replicates for each experimental condition. By looking at the cross-sectional micrographs, it appears that the structure of the films obtained with 30 wt% HPC (see Figure 5.22b and e) exhibits larger structures, while the film structures obtained with 45 wt% HPC exhibits smaller structures (see Figure 5.22c and d). These observations are in accordance with results in section "5.2.4Influence of the EC/HPC ratio on the time-dependent structure evolution" and **Paper II**.
In the cross-sectional micrographs in Figures 5.22b, c, d, e, it can be noted that there is a gradient in the domain size ranging from a bigger structure at the substrate surface to smaller structure at the air surface. This can also be observed in Figure 5a with the decreasing length scale from the substrate surface to the air surface. Secondary phase separation is particularly visible in Figure 5.22b, where small domains of EC appear in bigger domains of HPC, and vice-versa.
Figure 5.23 shows an example of a multilayer film made of 10 layers with alternating 30 wt% HPC and 45 wt% HPC characterized by CLSM and SEM. The secondary phase separation is clearly visible in Figure 5.23. In particular, we can see in the CLSM micrograph in Figure 5.23a small domains of HPC in larger EC domains, that after leaching correspond to pores in the SEM micrograph in Figure 5.23b. The length scale of the secondary phase separation is significantly smaller than the length scale of the primary phase separation (Tanaka, 1994, Tanaka and Araki, 1998).

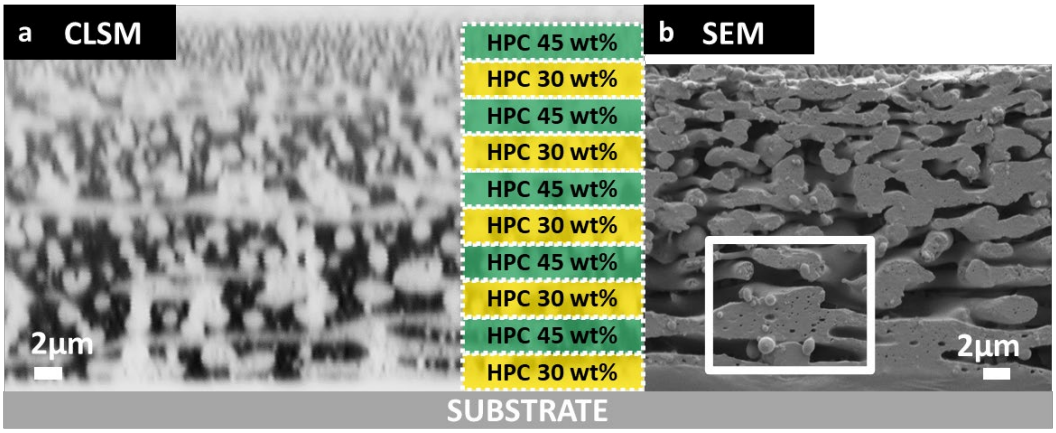

Figure 5.23 *Characterization of a multilayer EC/HPC film made of 10 layers with alternating HPC concentration (30 wt% and 45 wt% HPC). a) CLSM micrograph showing a film cross-section in the xz plane with the corresponding HPC fraction indicated for each layer (HPC in dark and EC in bright). b) SEM micrograph of the cross-section obtained with a cryostat after leaching of HPC. The secondary phase separation in the EC phase is particularly visible in the white rectangle.*

5.3.2 Structure evolution during the interaction between a multilayer film and a droplet of EC/HPC

During the industrial coating process, the polymer solution is sprayed onto the surface of the pellet to form a film. By increasing the time spent in the Wurster fluidized bed, the number of passages for each pellet in the spraying zone increases, resulting in a thicker coating (Heinrich *et al.*, 2015). In the following section, the aim was to understand the interaction between a dried multilayer film and droplets of polymer solution hitting the film. Therefore, a set-up was developed to monitor *in situ* the structure development and the interaction between a multilayer film and droplets of polymer solutions with different EC/HPC ratios. The structure evolution was characterized with CSLM and the thickness evolution during shrinkage due to solvent evaporation was estimated with image analysis (**Paper IV**).

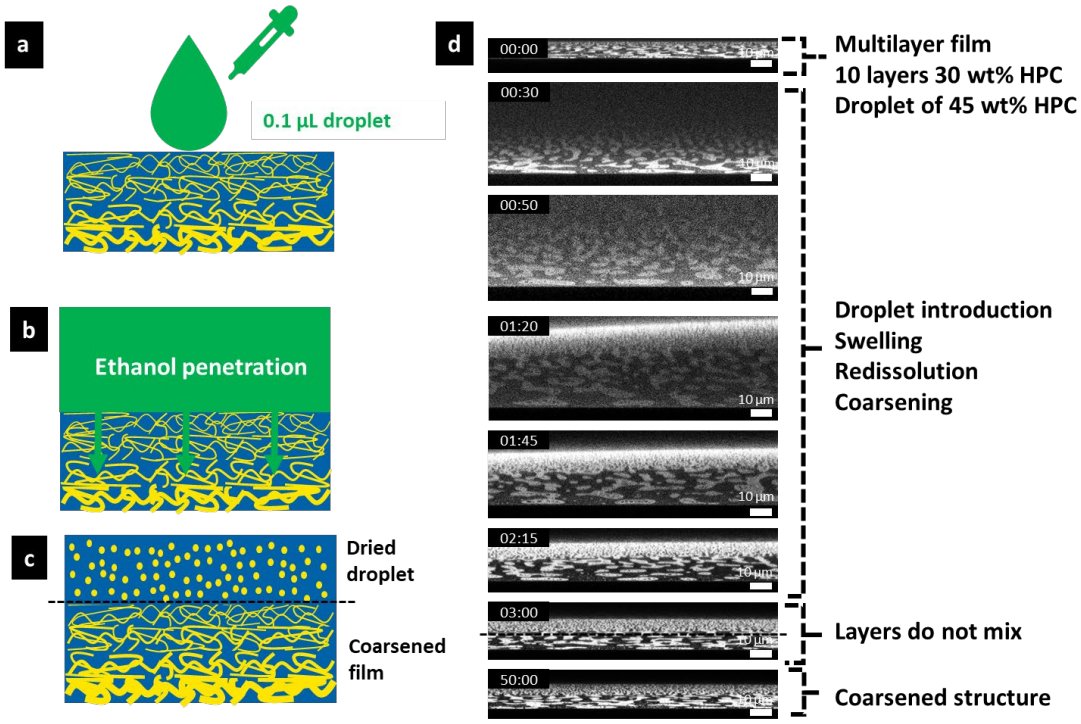

Figure 5.24 *a - c) Schematic illustration of the interaction between a droplet with a different EC/HPC ratio compared to the EC/HPC ratio in the multilayer film. d) CLSM-micrograph time series showing an example of the experiment with a 10 layer 30 wt% HPC film and a 0.1µL droplet with 45 wt% HPC.*

Figures 5.24a to c show a schematic illustration of the experimental set-up and the phenomena taking place. Figure 5.24d shows the structure evolution of a multilayer film made of 10 layers of 30 wt% HPC during the introduction of a 0.1µL 45 wt% HPC droplet.

Several phenomena can be observed during the structure evolution. When the droplet is deposited, the ethanol from the droplet penetrates the film. It results in swelling of the film, redissolution of the already present layers and coarsening of the phase-separated structure, see Figure 5.24b. Then the ethanol evaporates, and the film shrinks. An example of all these phenomena can be seen in Figure 5.24d. In the CLSM cross-sectional micrographs, the coarsening within the multilayer film can be observed while the film is shrinking, resulting in

larger length scales in the first 10 layers (see the image analysis in Figure10 in **Paper IV**). In Figure 5.24d, we can observe that during the shrinkage of the film, a clear bright phase is present at the top already after 1:20 min. The lower part of the bright phase forms an interface that corresponds to the interface between the 10-layer film and the droplet material. This is illustrated in Figure 5.24c and also visible in Figure 5.24d. This experiment shows that even with a very large amount of polymer solution deposited onto the surface of the multilayer film, the ethanol penetrates, and redissolves the polymer material, but the polymers from the successive layers do not mix.

5.3.3 Films with varying EC/HPC ratio and spin speed

Fager *et al.* (2020) observed using FIB-SEM that the film structure coated onto the pellets made through the industrial process of fluidized bed spraying was layered. Interfaces were visible between the layers exhibiting different porosity. Our hypothesis is that since the coating in the fluidized spraying device is rather chaotic, the parameters of coating are varying between each passage through the spraying zone, thus giving rise to different structures in each layer. Probably many phenomena are taking place, but we can identify three main possibilities: for each passage, the following three parameters can influence the porosity: the pellet drying rate, the ethanol content, and the EC/HPC ratio. It was shown in **Paper I**, **Paper II** and **Paper III** on monolayers, that the change of spin speed (directly related to the drying rate) and EC/HPC ratio have effect on both the layer thickness and the length scale of the structure. Here, the multilayer films were produced with varying EC/HPC ratio and spin speed during the successive deposition cycles.

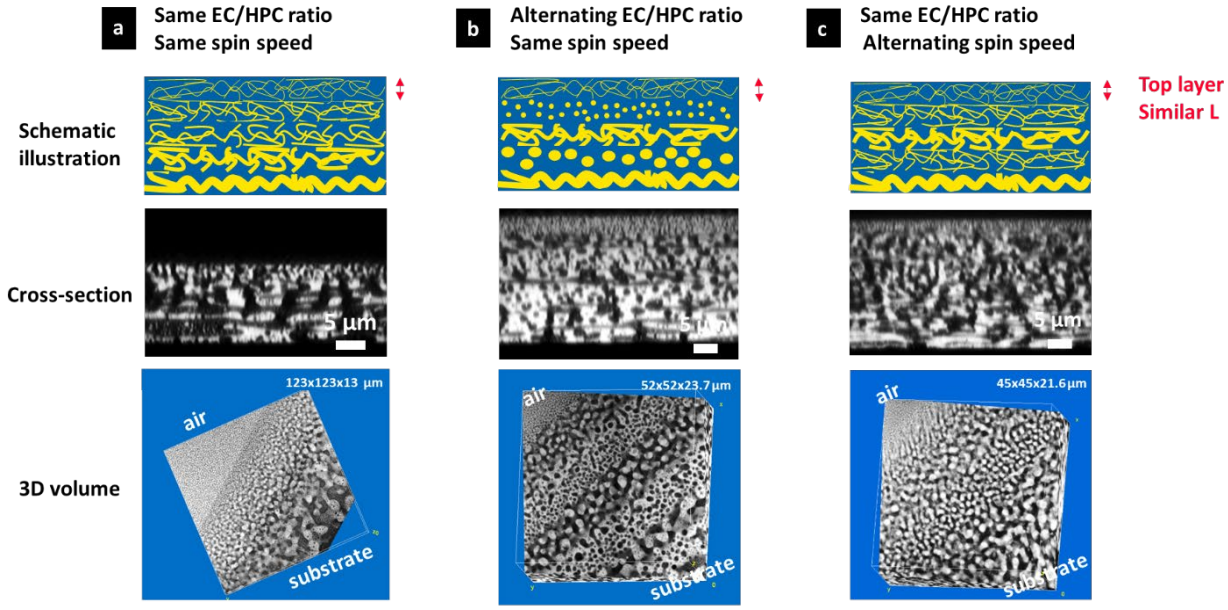

Figure 5.25 *Illustration of the effect of the EC/HPC ratio and the spin speed on the multilayer film structures. In the top, middle and bottom rows, schematic illustration of the multilayer film, CLSM cross-sections and 3D volumes, are shown, respectively. a) 8 layers 30 wt% HPC film spun at 2000 RPM, b) 10 layers HPC film alternating with 30 and 45 wt% HPC spun at 2000 RPM and, c) 10 layers 30 wt% HPC film with alternance between 2000 and 8000 RPM.*

Figure 5.25 shows schematic illustrations of three examples of multilayer films. In Figure 5.25a, a film made with constant EC/HPC ratio and spin speed is shown. In Figure 5.25b, a multilayer film is displayed where the spin speed is kept constant and the EC/HPC ratio is varied. A multilayer film where the EC/HPC ratio is kept constant, and the spin speed is varied is shown in Figure 5.25c.
In Figure 5.25b, a 10-layer film was produced by alternating between 30 wt% HPC and 45 wt% HPC. In **Paper IV**, the film cross-section was imaged with CLSM and SEM, and a 3D volume was obtained with CLSM and FIB-SEM. Here, we show only the CLSM micrographs. On the cross-section in Figure 5.25b, it seems difficult to identify the single layers, but it is possible to recognize the morphology with bigger domains closer to the substrate and smaller domains closer to the air surface (see **Paper IV**). When comparing the length scale throughout the film in Figure 5.25a, where the EC/HPC ratio was constant, and the length scale through the film in Figure 5.25b, where the EC/HPC ratio changes, we can see that, even though the general trend is a gradient in length scale, we can see the influence of alternating the EC/HPC ratio. By alternating between 30 wt% HPC and 45 wt% HPC, an alternation between bigger and smaller structures is observed. This observation is confirmed by the 3D volume in the bottom of Figure 5.25b where it is easy to see the transition between the layers made with alternating EC/HPC ratio. We can observe a bicontinuous-like larger structures which is likely to correspond to the layers made of 30 wt% HPC and a more discontinuous-like structures which is likely to be made of 45 wt% HPC.
Figure 5.25c shows an example of a 10-layer film made by changing the spin speed from 2000 RPM to 8000 RPM. As for the films in Figures 5.25 a and b, it is more difficult to identify the layers in the cross-section image. However, in the 3D volume it is possible to observe the alternation between smaller and bigger structures resulting from alternating spin speed during the spin-coating process. The general trend in Figure 5.25 is that the length scale is decreasing from the substrate surface to the air surface (see **Paper IV** for the quantitative image analysis). As discussed previously, the redissolution takes place in each deposition cycle and in the layers already deposited, the phase separation is resumed, leading to coarsening and larger structures. However, we do not have a gradient in Figure 5.25c as strong as the one observed in Figure 5.25a. It seems that there is, like in Figure 5.25b, an alternation between small and bigger structures, with smaller length scale and thinner layer when the spin speed was 8000 RPM and bigger length scale and thicker layer when the spin speed was 2000 RPM (see **Paper IV)**.

Finally, the layer that is in contact with the air exhibits significantly smaller structure as can be seen in Figures 5.25a to c. The layer close to the air is drying faster (Mokarian-Tabari *et al.*, 2010, Raj Kumar, 2012, De Gennes, 2002, Cummings *et al.*, 2018, De Gennes, 2001), so that the phase-separated structure is trapped at an earlier stage, resulting in smaller structures. The length scales of the top observed in Figures 5.25a, b, c are within a similar value range (see **Paper IV).** It is also in the same order as in the monolayer films investigated in **Paper I.**

During the multilayer film formation in the industrial fluidized bed spraying device, it is highly probable that many phenomena are competing as stated in the introduction section. However, the influence of spin speed which mimics the influence of the pellet drying rate can help to answer some of the questions concerning the varying porosity in the industrial pellets.

5.3.4 Mechanisms involved during the multilayer film formation

The observations in the previous sections indicated that it was likely that during the multiple deposition cycles through the spin-coating process, the successive layers do not mix. In addition, in the industrial pellets, two observations were made: first, it was possible to observe layers and second, those layers exhibited varying porosity and structure (Fager, 2020). It was seen in "5.3.1 Films with constant EC/HPC ratio and spin speed", and Figure 5.22 that when the spin-coating parameters and the EC/HPC ratio of the coating solution are kept constant at every deposition cycle, the structure size from one layer to another decreases from the substrate surface to the air surface.

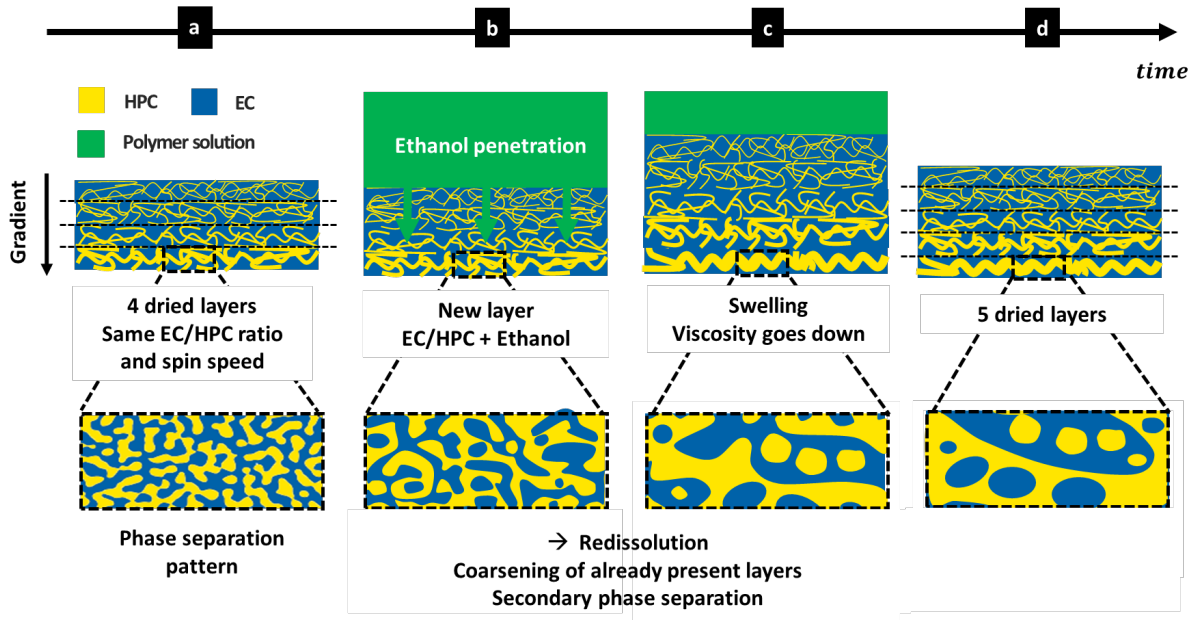

Figure 5.26 *Schematic illustration of the phenomena taking place during the coating of an EC/HPC layer on a multilayer film. On the top the view of the multilayer film going from 4 to 5 layers. On the bottom row, a magnified view of the phase-separated structure during redissolution. With a) the 4 layers film b) the coating of the 5th layer with ethanol penetration c) Swelling of the film and redissolution d) the final dried 5 layers film.*

The formation of multilayer films corresponds to a superposition of the monolayer structure formation mechanisms with additional effects induced by the application of a new layer. Figure 5.26 shows a schematic illustration of the phenomena taking place during the coating of a new layer on an EC/HPC film constructed with constant spin speed and constant EC/HPC ratio. The presence of the gradient in structure size can be explained by the redissolution effect. When introducing polymer solution during successive deposition cycles, the ethanol contained in the solution, penetrates in the film, and redissolves the dried polymer material (Figure 5.26b). With this redissolution, the mobility of EC and HPC in the precedent layers increase, and the structure that was trapped by solvent quenching can continue to coarsen (Figure 5.26b and c). The layers closer to the substrate undergo redissolution more times than the layers at the surface resulting in a gradient in phase separation/coarsening stage throughout the film, with more advanced stages in the first layers compared to the last layers. The redissolution is confirmed by the

presence of a secondary phase separation that is visible on the layers close to the substrate surface in Figure 5.22 and represented in Figure 5.26.
Finally, it was seen that the successive layers do not mix (**Paper IV**). The HPC domains in the newly introduced layer will find the HPC domains and the EC domains will find the EC domains (templating), which might increase the tendency to form bicontinuous structures. However, in most cases an interface could be observed between successive layers, see for instance Figure 5.24 and Figure 5.25 and **Paper IV**. Our hypothesis is that when EC and HPC are being redissolved by the ethanol from the newly introduced layer, the phase separation restarts, and the structure coarsens within the already present layer. Since EC and HPC are immiscible, there is no driving force for the polymers from the already deposited layer to mix with the newly introduced polymers. This likely increases the tendency to form layers with different structures and porosity.

6 Summary Figure: Structure evolution of phase-separated EC/HPC films for controlled drug release

In this section, we summarize the methods used and the main results obtained in this PhD work. The following "Figure 5.27 *Summary Figure*" is a schematic illustration of the EC/HPC phase separation in monolayer and multilayer films for the tailoring of the porous structure that controls the drug release rate in medical pellets.

In 1) the direct relation between the structure of the pellet coating and the drug release rate is shown. The polymer solution is coated onto the drug pellet, and a phase-separated coating is obtained. After swallowing of the pellet and leaching of HPC, the porous structure is formed, and the drug can be released. To tailor the porous film structure in 2), we need to first tailor the phase-separated structure and in 3) understand the different phase separation mechanisms responsible for the phase-separated structure. To tailor the phase-separated structure, we needed to gather knowledge and understanding about the phase separation that takes place during the industrial spray-coating process. However, since the fluidized bed spraying device is a challenging environment to investigate the detailed structure evolution into, it was decided to find a way the mimic the industrial process 4).

An experimental set-up was developed using a combination of spin-coating, CLSM and image analysis to characterize the structure evolution *in situ* in monolayer films. In 5) we determined the different coarsening mechanisms taking place during the structure evolution of bicontinuous and discontinues structures in monolayer films. We also determined the time dependency of each coarsening mechanisms. Information about the phase separation kinetics and coarsening mechanisms provided essential understanding that could be used in the multilayer films (transition from 4) to 7)). The formation of multilayer films corresponded to a superposition of the monolayer structure formation mechanisms with additional effects induced by the application of a new layer.

From the data of the monolayer structure evolution of the monolayer we could also estimate the position of the binodal curve in the EC/HPC/EtOH phase diagram in 6). Then, in 7) with the knowledge gathered on the monolayers we could make multilayer films in a controlled way and mimic the industrial pellet by making multilayer films. The multilayer films presented varying porosity with a gradient going from the substrate surface to the air surface. Finally, an *in situ* experimental set-up was developed to characterize the interaction between a multilayer film and a droplet, see 8). The results showed that the layers do not mix when coating a new layer on a multilayer film.

Figure 6.1

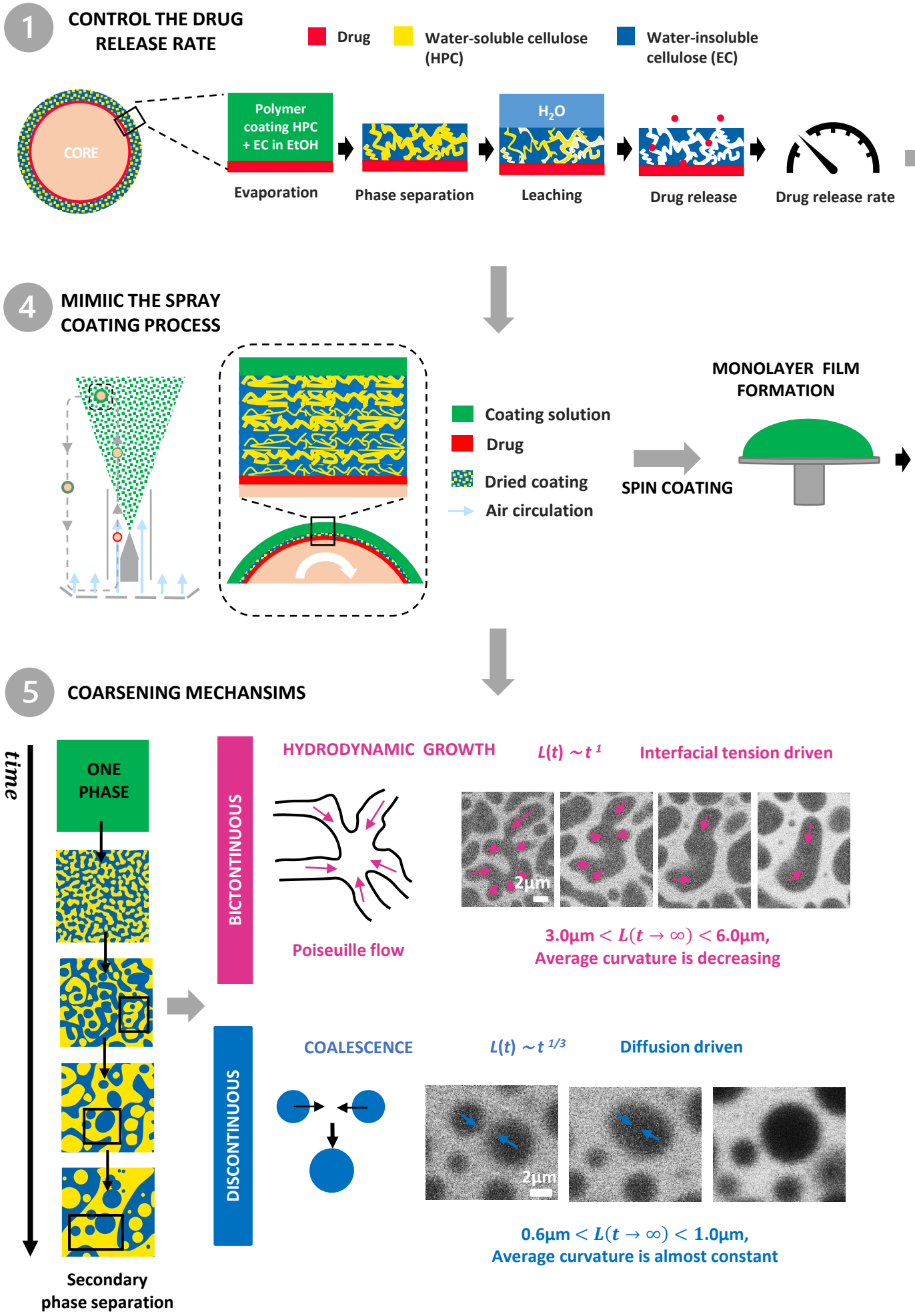
1
CONTROL THE DRUG RELEASE RATE
Drug
Water-soluble cellulose (HPC)
Water-insoluble cellulose (EC)
CORE
Polymer coating HPC + EC in EtOH
Evaporation
Phase separation
H_2O
Leaching
Drug release
Drug release rate
4
MIMIIC THE SPRAY COATING PROCESS
Coating solution
Drug
Dried coating
Air circulation
SPIN COATING
MONOLAYER FILM FORMATION
5
COARSENING MECHANSIMS
time
ONE PHASE
Secondary phase separation
BICTONTINUOUS
HYDRODYNAMIC GROWTH
$L(t) \sim t^{1}$
Interfacial tension driven
Poiseuille flow
2μm
3.0μm < $L(t \to \infty)$ < 6.0μm,
Average curvature is decreasing
DISCONTINUOUS
COALESCENCE
$L(t) \sim t^{1/3}$
Diffusion driven
2μm
0.6μm < $L(t \to \infty)$ < 1.0μm,
Average curvature is almost constant

Summary Figure

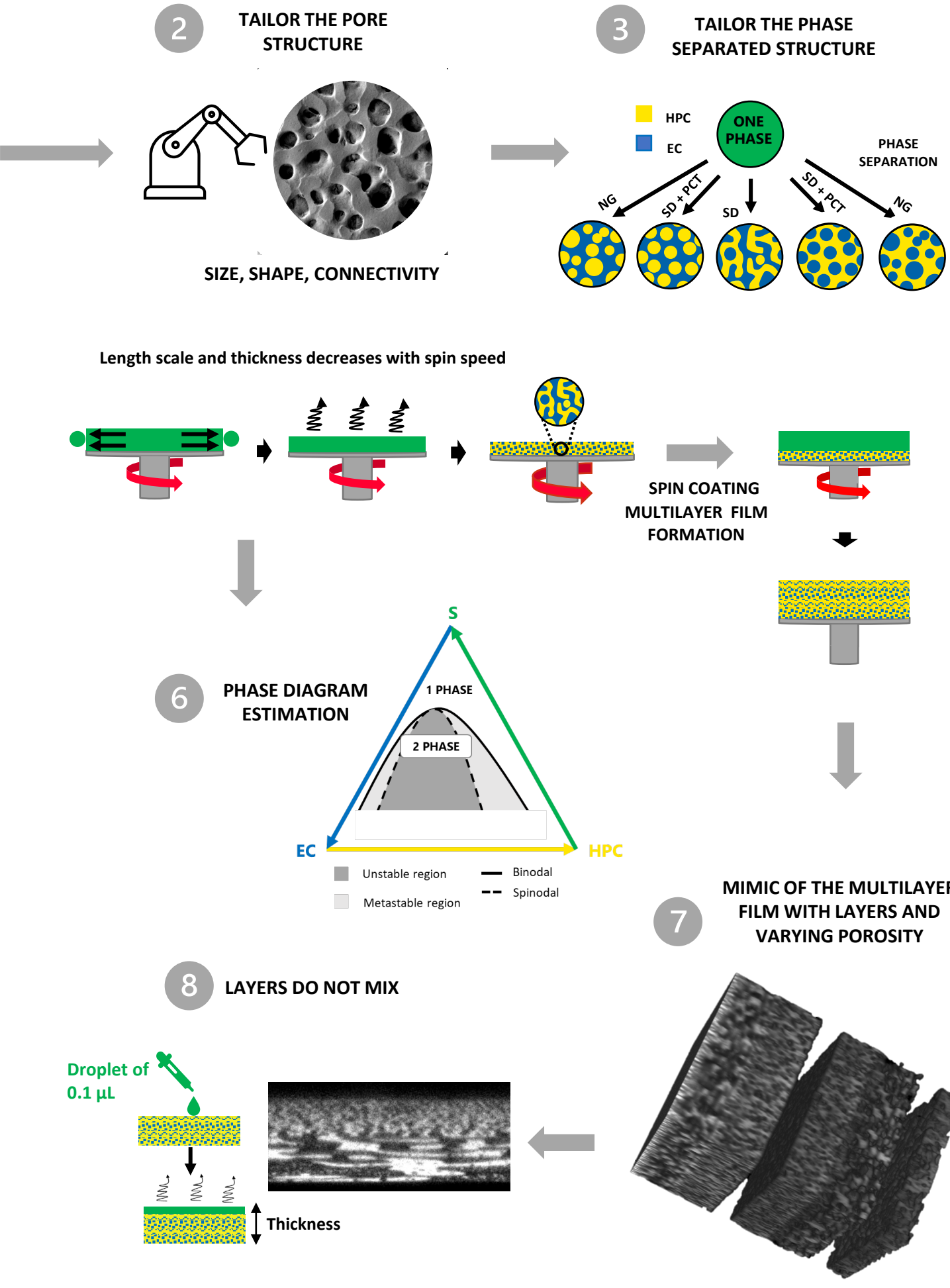

7 Conclusions

It was found that the combination of confocal laser scanning microscopy, scanning electron microscopy, focused ion beam scanning electron microscopy, image analysis, rheology and profilometry was very powerful to investigate spin-coated phase-separated monolayer and multilayer films made of EC/HPC. The spin-coating technique provided good control and reproducibility of the final film structures and made it possible to mimic the structure evolution inside the fluidized bed spraying used in the industrial pellet manufacturing process.

When characterizing monolayer films, our results showed that the final characteristic length scale of the phase-separated structure and film thickness decreased with increasing spin speed. Investigation of the in-plane phase separation kinetics and coarsening mechanism provided further understanding of the processes controlling the phase-separated structure of thin EC/HPC films. The influence of the EC/HPC ratio on the final structure was determined and two cases, bicontinuous and discontinuous were identified. Bicontinuous structures were related to a hydrodynamic regime with interfacial tension-driven hydrodynamic coarsening. A diffusive regime with coalescence, small structures, and slow growth rate were found for the discontinuous structures. Larger structures and higher growth rates were found for the bicontinuous structures than for the discontinuous ones. A new image analysis method for characterization of the 2D interface curvature evolution was developed. Evaluation of the curvature evolution of the interface between EC and HPC showed that the mean curvatures of bicontinuous structures decreased with time and that the curvature distributions became narrower, supporting an interfacial tension-driven hydrodynamic coarsening mechanism of the bicontinuous structures.

Investigation of the cross-sectional structure evolution was performed. The shrinkage rate was extracted, and estimation of the binodal curve in the EC/HPC/EtOH phase diagram was performed. It was observed that during the shrinkage of the film, the phase-separated structure undergoes a transition from a 3D to a nearly 2D structure evolution along the surface. This transition appears when the typical length scale of the phase-separated structure is in the order of the thickness of the film. Analysis of the time-dependent film thickness observed via CLSM showed that the evaporation was independent of the EC/HPC ratio which is in accordance with the gravimetric investigation. It was also found that the film thickness decreases linearly and rapidly during the first minutes after spin-coating, and then slowly with a lower slope for several hours.

In multilayer films, the effects of the EC/HPC ratio and spin speed on the structure formation were investigated. Multilayer films made with a constant EC/HPC ratio showed structures quite similar to the structures of the monolayer films. A gradient with larger structures close to the substrate and smaller structures close to the air surface was found. This gradient was explained by the redissolution and coarsening of the layers already coated during successive deposition cycles. The redissolution and coarsening were induced by the ethanol that rapidly penetrated the already present multilayer film. Variation of the EC/HPC ratio between different layers resulted in a layered structure with different porosities. *In situ* characterization of the structure

evolution of the interaction between a multilayer film and a droplet of polymer solution showed that the multilayer film and the new droplet do not mix. This results in an interface between the already present multilayer film and the new layer. However, a templating effect was observed where no abrupt changes (or discontinuities) at the interface between the two layers were seen. Finally, by varying the spin speed every other layer, and therefore the drying kinetics, we produced a layered film exhibiting varying porosity. Based on the observations, we proposed a possible explanation for the formation of the layered coating in the industrial process.

Understanding how phase separation and pore formation take place on the microscopic level and how it can be more precisely controlled to optimize the drug release is a challenging and complete task. In this PhD work, by mimicking the industrial process of spray-coating, we developed a mechanistic understanding of the structure evolution of phase-separated EC/HPC films. Based on this work, we offer more possibilities into tailoring the porous structure and therefore the release of the drug.

8 Future Outlook

Many questions remain and would be of interest for further study. During the formation of a multilayer film with spin-coating, we expected that by redissolution of the layers already deposited by the ethanol from the new layer, the whole polymer material would mix, and phase separate to form a thicker layer. However, we noticed that the new and the already deposited preceding layer do not mix, giving rise to an interface between the multilayer film and the newly formed layer. The nature of this interaction is yet to be determined. We hypothesized that the non-mixing of the successive layers was caused by the absence of driving forces for already phase-separated polymers to mix with the newly introduced polymers. An on-going collaboration with Jens Poulsen and Jan Westergren from Wendelsbergs beräkningskemi is bringing new insights on this matter. Computer simulations based on Cahn-Hilliard and Flory-Huggins theory are being used to explain why the successive layers do not mix during the multilayer film formation. Initial results are very promising. They describe the interaction between a dried 45 wt% HPC layer, and a new layer of 100 wt% EC in ethanol, and in accordance with the experimental results they show that the layers do not mix. This work will be added to **Paper IV**.

To complete the study of **Paper IV**, additional experiments are being performed to explore the effect of spin speed on the multilayer film. We are performing FIB-SEM tomography on the film with alternating spin speed between each deposition cycle.

Since it was shown in previous work from Andersson et al. (2015) that the molecular weight of EC and HPC has a strong influence on the final film structure, it would be of interest to investigate the effect of molecular weight (Mw) and degree of substitution (DS) on the structure evolution. The same experiments performed in **Paper I**-**IV** could be repeated with varying Mw and DS.

Similarly, it would be interesting to investigate the effect of the ratio between the total polymer content and the ethanol on the structure evolution when spin-coating a multilayer film. The same experiments performed in **Paper I**-**IV** could be repeated with varying the polymer/ethanol ratio.

In **Paper III**, we developed a new method to estimate the position of the spinodal curve in the EC/HPC/EtOH phase diagram. To be able to apply this method to other systems (other polymers than EC and HPC), it would be interesting to improve the phase diagram estimation developed in **Paper III**. This was performed by estimating the ethanol content based on film thickness and the accuracy could be increased for example by using a CLSM with higher axial resolution. It would also be relevant to estimate the EC/HPC/EtOH phase diagram at different pressures and temperatures, closer to the conditions of the industrial process of spray-coating.

In this work, we used spin-coating to mimic the industrial process. In future work, a promising direction would be to compare and investigate additional ways to mimic the fluidized bed spraying device. For example, to further explore the structure formation in the industrial process, we could investigate the structure evolution *in situ* during the interaction between an EC/HPC multilayer film and droplets of equivalent size to the fluidized bed spraying device.

Another aspect of the EC/HPC system that would be relevant to study further is the leaching of HPC from an EC/HPC multilayer film cross-section *in situ.* This could be achieved using water

vapor in E-SEM (Environmental SEM), with inspiration from the work by Jansson et al. (Jansson *et al.*, 2013, Jansson *et al.*, 2014).

Finally, since the coating is intended to be applied on another layer consisting of the drug, it would be valuable to investigate the interaction between the drug layer and the first layers of EC/HPC during the coating of a pellet.

References

AARTS, D. G. A. L., LEKKERKERKER, H. N. W., GUO, H., WEGDAM, G. H. & BONN, D. 2005. Hydrodynamics of Droplet Coalescence. *Physical Review Letters,* 95**,** 164503-1 - 164503-4.

ALEXANDER, F. J., CHEN, S. & GRUNAU, D. W. 1993. Hydrodynamic spinodal decomposition: Growth kinetics and scaling functions. *Physical Review B,* 48**,** 634-637.

ALIG, I., RÜLLMANN, M., HOLST, M. & XU, J. 2003. Phase separation by continuous quenching: similarities between cooling experiments in polymer blends and reaction-induced phase separation in modified thermosets. *Macromolecular Symposia,* 198**,** 245-258.

ANDERSSON, H. 2015. *Structure control by phase separation and influence on mass transport in films for controlled release.* Doctoral Thesis, Chalmers Universit of Technology.

ANDERSSON, H., HÄBEL, H., OLSSON, A., SANDHAGEN, S., VON CORSWANT, C., HJÄRTSTAM, J., PERSSON, M., STADING, M. & LARSSON, A. 2016. The influence of the molecular weight of the water-soluble polymer on phase-separated films for controlled release. *International Journal of Pharmaceutics,* 511**,** 223-235.

ANDERSSON, H., HJÄRTSTAM, J., STADING, M., VON CORSWANT, C. & LARSSON, A. 2013. Effects of molecular weight on permeability and microstructure of mixed ethyl-hydroxypropyl-cellulose films. *European Journal Pharmaceutical Sciences,* 48**,** 240-8.

ANDERSSON, H., MARUCCI, M., HJÄRTSTAM, J., STADING, M., VON CORSWANT, C. & LARSSON, A. 2009. New insights into the effects of polymer molecular weight on release mechanisms through polymer blend coatings. *European Journal of Pharmaceutics and Biopharmaceutics,* 83**,** 301-6.

ANDERSSON, H., ÖHGREN, C., JOHANSSON, D., KNIOLA, M. & STADING, M. 2011. Extensional flow, viscoelasticity and baking performance of gluten-free zein-starch doughs supplemented with hydrocolloids. *Food Hydrocolloids,* 25**,** 1587-1595.

ASHLAND. 2017. *Klucel hydroxypropylcellulose, Physical and chemical properties* [Online]. USA. [Accessed].

BADERSTEDT, J. 2011. *The effect of molecular weight on the performance of ethyl cellulose membranes.* Master Thesis, Chalmers University of Technology.

BAILEY, A. E., POON, W. C., CHRISTIANSON, R. J., SCHOFIELD, A. B., GASSER, U., PRASAD, V., MANLEY, S., SEGRE, P. N., CIPELLETTI, L., MEYER, W. V., DOHERTY, M. P., SANKARAN, S., JANKOVSKY, A. L., SHILEY, W. L., BOWEN, J. P., EGGERS, J. C., KURTA, C., LORIK, T., JR., PUSEY, P. N. & WEITZ, D. A. 2007. Spinodal decomposition in a model colloid-polymer mixture in microgravity. *Physical Review Letters,* 99**,** 205701.

BARBERO, N., BARNI, E., BAROLO, C., QUAGLIOTTO, P., VISCARDI, G., NAPIONE, L., PAVAN, S. & BUSSOLINO, F. 2009. A study of the interaction between fluorescein sodium salt and bovine serum albumin by steady-state fluorescence. *Dyes and Pigments,* 80**,** 307-313.

BARMAN, S. 2020. *The pore geometry of pharmaceutical coatings: statistical modelling, characterization methods and transport prediction.* Doctoral Thesis, Chalmers University of Technology.

BARNES, H. 2000. *Handbook of Elementary Rheology,* University of Wales.

BINDER, K., PURI, S., DAS, S. K. & HORBACH, J. 2010. Phase Separation in Confined Geometries. *Journal of Statistical Physics,* 138**,** 51-84.

BINDER, K. & STAUFFER, D. 1974. Theory for slowing down of the relaxation and spinodal decomposition of binary mixtures. *Physical Review Letters,* 33**,** 1006-1009.

BIRNIE, D. P. 2011. Rational solvent selection strategies to combat striation formation during spin coating of thin films. *Journal of Materials Research,* 16**,** 1145-1154.

BIRNIE, D. P. & MANLEY, M. 1997. Combined flow and evaporation of fluid on a spinning disk. *Physics of Fluids,* 9**,** 870-875.

BOUTTES, D., LAMBERT, O., CLAIREAUX, C., WOELFFEL, W., DALMAS, D., GOUILLART, E., LHUISSIER, P., SALVO, L., BOLLER, E. & VANDEMBROUCQ, D. 2015. Hydrodynamic coarsening in phase-separated silicate melts. *Acta Materialia,* 92**,** 233-242.

BRAY, A. J. 2003. Coarsening dynamics of phase separating systems. *Philosophical Transactions of the Royal Society of London A* 361**,** 781–792.

BRAY, A. J. 2010. Theory of phase-ordering kinetics. *Advances in Physics,* 51**,** 481-587.

BUXTON, G. A. & CLARKE, N. 2007. Ordering polymer blend morphologies via solvent evaporation. *Europhysics Letters,* 78**,** 56006.

CAHN, J. W. 1965. Phase separation by spinodal decomposition in isotropic systems. *Journal of Chemical Physics,* 42**,** 93-99.

CHESTERS, A. K. 1991. The modelling of coalescence processes in fluid-liquid dispersions : a review of current understanding. *Chemical Engineering Research and Design,* 69**,** 259-270.

CLARK, A. H. 1995. Kinetics of demixing. *Biopolymer Mixtures.* Nottingham University Press.

CLARK, E. A. & LIPSON, J. E. G. 2012. LCST and UCST behavior in polymer solutions and blends. *Polymer,* 53**,** 536-545.

COEURJOLLY, D. & SVENSSON, S. 2003. Estimation of Curvature along Curves with Application to Fibres in 3D Images of Paper. *SCIA'03: Proceedings of the 13th Scandinavian conference on Image analysis.*

CUMMINGS, J., LOWENGRUB, J. S., SUMPTER, B. G., WISE, S. M. & KUMAR, R. 2018. Modelling solvent evaporation during thin film formation in phase separating polymer mixtures. *Soft Matter,* 14**,** 1833-1846.

DANDAPAT, B. S., SANTRA, B. & KITAMURA, A. 2005. Thermal effects on film development during spin coating. *Physics of Fluids,* 17.

DAS, N. C. 2014. Phase behaviour and separation kinetics of polymer blends. *Journal of Microscopy,* 253**,** 198-203.

DATT, C., THAMPI, S. P. & GOVINDARAJAN, R. 2015. Morphological evolution of domains in spinodal decomposition. *Physical Review E,* 91**,** 010101- 1-5.

DE GENNES, P. G. 1979. *Scaling concepts in polymer physics,* Ithaca and London, Cornell University Press.

DE GENNES, P. G. 1985. Wetting: statics and dynamics. *Reviews of Modern Physics,* 57**,** 827-863.

DE GENNES, P. G. 2001. Instabilities during the evaporation of a film: Non-glassy polymer + volatile solvent. *The European Physical Journal E,* 6**,** 421-424.

DE GENNES, P. G. 2002. Solvent evaporation of spin cast films: “crust” effects. *The European Physical Journal E,* 7**,** 31-34.

DE GENNES, P. G., BROCHARD-WYART, F. & QUERE, D. 2004. *Capillarity and Wetting Phenomena: Drops, Bubbles, Pearls, Waves*

DEBENEDETTI, P. G. 2000. Phase separation by nucleation and by spinodal decomposition: fundamentals. *In:* PUBLISHERS, K. A. (ed.) *Supercritical Fluids.* E. Kiran et al.

DEPREZ, J. 2016. *Dynamic and Microscturcure in Porous Polymer Films.* Master Thesis, Ghent University.

DHONT, J. K. G. 1996. Spinodal decomposition of colloids in the initial and intermediate stages. *The Journal of Chemical Physics,* 105**,** 5112-5125.

DONATO, L., GARNIER, C., NOVALES, B., DURAND, S. & DOUBLIER, J.-L. 2005. Heat-Induced Gelation of Bovine Serum Albumin/Low-Methoxyl Pectin Systems and the Effect of Calcium Ions. *Biomacromolecules,* 6**,** 374-385.

DOWCELLULOSICS. 2005. *ETHOCEL, Ethylcellulose Polymers Technical Handbook* [Online]. USA. [Accessed].

DUNBAR, A. D., MOKARIAN-TABARI, P., PARNELL, A. J., MARTIN, S. J., SKODA, M. W. & JONES, R. A. 2010. A solution concentration dependent transition from self-stratification to lateral phase separation in spin-cast PS:d-PMMA thin films. *European Physical Journal E,* 31**,** 369-75.

EBBENS, S., HODGKINSON, R., PARNELL, A. J., DUNBAR, A., MARTIN, S. J., TOPHAM, P. D., CLARKE, N. & HOWSE, J. R. 2011. In Situ Imaging and Height Reconstruction of Phase Separation Processes in Polymer Blends during Spin Coating. *ACS Nano,* 5**,** 5124-5131.

EDSBÄCKER, S., BENGTSSON, B., LARSSON, P., LUNDIN, P., NILSSON, Å., ULMIUS, J. & WOLLMER, P. 2003. A pharmacoscintigraphic evaluation of oral budesonide given as controlled-release (Entocort) capsules. *Alimentary Pharmacology & Therapeutics,* 17**,** 525-536.

EL KHOURY, D. 2017. *Towards the use of Electrostatic Force Microscopy to study interphases in nanodielectric materials.* Doctoral Thesis, Grenoble University, Grenoble, France.

FAGER, C. 2018. *3D Reconstruction of Porous and Poorly Conductible Soft Materials using FIB-SEM Tomography.* Licentiate thesis, Chalmers University of Technology.

FAGER, C. 2020. *Quantitative 3D reconstruction of porous polymers using FIB-SEM tomography.* Doctoral Thesis, Chalmers University of Technology.

FAGER, C., BARMAN, S., RÖDING, M., OLSSON, A., LORÉN, N., VON CORSWANT, C., BOLIN, D., ROOTZEN, H. & OLSSON, E. 2020a. 3D high spatial resolution visualisation and quantification of interconnectivity in polymer films. *International Journal of Pharmaceutics,* 587**,** 119622.

FAGER, C., GEBÄCK, T., HJÄRTSTAM, J., RÖDING, M., OLSSON, A., LORÉN, N., VON CORSWANT, C., SÄRKKÄ, A. & OLSSON, E. 2021a. Correlating 3D porous structure in polymer films with mass transport properties using FIB-SEM tomography. *Chemical Engineering Science: X,* 12**,** 100109.

FAGER, C., RÖDING, M., OLSSON, A., LORÉN, N., VON CORSWANT, C., SARKKA, A. & OLSSON, E. 2020b. Optimization of FIB-SEM Tomography and Reconstruction for Soft, Porous, and Poorly Conducting Materials. *Microscopy and Microanalysis,* 26**,** 837-845.

FAGER, C., VON CORSWANT, C., RÖDING, M., VIRIDÉN, A., JOHANSSON, M.-O., OLSSON, A., LORÉN, N. & OLSSON, E. 2021b. Correlating release properties with porous structure of pellet coatings used for controlled drug release. . *In:* MANUSCRIPT (ed.) *International Journal of Pharmaceutics.* .

FANG, L., WEI, M., BARRY, C. & MEAD, J. 2010. Effect of Spin Speed and Solution Concentration on the Directed Assembly of Polymer Blends. *Macromolecules,* 43**,** 9747-9753.

FARRELL, J. E. & VALLS, O. T. 1989. Spinodal decomposition in a two-dimensional fluid model. *Physical Review B,* 40**,** 7027-7039.

FIROOZMAND, H., MURRAY, B. S. & DICKINSON, E. 2012. Microstructure and elastic modulus of mixed gels of gelatin+oxidized starch: Effect of pH. *Food Hydrocolloids,* 26**,** 286-292.

FISCHER, H., MURRAY, M., KELLER, A. & ODELL, J. A. 1995. On the phase diagram of the system hydroxypropylcellulose-water. *Journal of Materials Science,* 30**,** 4623-4627.

FLORY, P. J. 1942. Thermodynamics of High Polymer Solutions. *The Journal of Chemical Physics,* 10**,** 51-61.

FOWLER, P. D., RUSCHER, C., MCGRAW, J. D., FORREST, J. A. & DALNOKI-VERESS, K. 2016. Controlling Marangoni-induced instabilities in spin-cast polymer films: How to prepare uniform films. *European Physical Journal E,* 39**,** 90.

FOX, S. C., LI, B., XU, D. & EDGAR, K. J. 2011. Regioselective Esterification and Etherification of Cellulose: A Review. *Biomacromolecules,* 12**,** 1956-1972.

FRANSSON, S., LOREN, N., ALTSKAR, A. & HERMANSSON, A.-M. 2009. Effect of Confinement and Kinetics on the Morphology of Phase Separating Gelatin-Maltodextrin Droplets. *Biomacromolecules,* 10**,** 1446-1453.

FREDENBERG, S., WAHLGREN, M., RESLOW, M. & AXELSSON, A. 2011. The mechanisms of drug release in poly(lactic-co-glycolic acid)-based drug delivery systems--a review. *International Journal of Pharmaceutics,* 415**,** 34-52.

FURUKAWA, H. 1985. Effect of inertia on droplet growth in a fluid. *Physical Review A,* 31**,** 1103-1108.

GEBÄCK, T., MARUCCI, M., BOISSIER, C., ARNEHED, J. & HEINTZ, A. 2015. Investigation of the Effect of the Tortuous Pore Structure on Water Diffusion through a Polymer Film Using Lattice Boltzmann Simulations. *The Journal of Physical Chemistry B,* 119**,** 5220-5227.

GIANNUZZI, L. A. 2005. *Introduction to Focused Ion Beams*, Springer US.

GIBBS, J. W. 1961. *The Scientific Papers of J. Willard Gibbs,* Dover, New York.

GOLDSTEIN, J., NEWBURY, D. E., JOY, D. C., LYMAN, C. E., ECHLIN, P., LIFSHIN, E., SAWYER, L. & MICHAEL, J. R. 2003. *Scanning Electron Microscopy and X-Ray Microanalysis*, Springer US.

GUPTA, H., BHANDARI, D. & SHARMA, A. 2009. Recent Trends in Oral Drug Delivery: A Review. *Recent Patents on Drug Delivery & Formulation,* 3**,** 162-173.

HASHIMOTO, T. 1988. Dynamics in spinodal decomposition of polymer mixtures. *Phase Transitions,* 12**,** 47-119.

HAVAIĆ, T., ĐUMBIR, A.-M., GRETIĆ, M., MATIJAŠIĆ, G. & ŽIŽEK, K. 2018. Droplet Impact Phenomena in Fluidized Bed Coating Process with a Wurster Insert. *International Journal of Chemical Engineering,* 2018**,** 1-11.

HEINRICH, S., DOSTA, M. & ANTONYUK, S. 2015. Multiscale Analysis of a Coating Process in a Wurster Fluidized Bed Apparatus. *Mesoscale Modeling in Chemical Engineering Part I.*

HENDERSON, I. C. & CLARKE, N. 2004. Two-Step Phase Separation in Polymer Blends. *Macromolecules,* 37**,** 1952-1959.

HERIOT, S. Y. & JONES, R. A. 2005. An interfacial instability in a transient wetting layer leads to lateral phase separation in thin spin-cast polymer-blend films. *Nature Materials,* 4**,** 782-6.

HILL, M. 1995. Ostwald ripening in polyethylene blends. *Polymer,* 36**,** 3369-3375.

HUANG, H., WU, Z., QI, X., ZHANG, H., CHEN, Q., XING, J., CHEN, H. & RUI, Y. 2013. Compression-coated tablets of glipizide using hydroxypropylcellulose for zero-order release: In vitro and in vivo evaluation. *International Journal of Pharmaceutics,* 446**,** 211-218.

HUTTON, J. T. & MORRIS, J. L. 1992. Long-acting carbidopa-levodopa in the management of moderate and advanced Parkinson's disease. *Neurology,* 42**,** 51-6; discussion 57-60.

HUYNH, C. T. & LEE, D. S. 2015. Controlled Release. *Encyclopedia of Polymeric Nanomaterials.*

JAMIE, E. A. G., DULLENS, R. P. A. & AARTS, D. G. A. L. 2012. Spinodal decomposition of a confined colloid-polymer system. *The Journal of Chemical Physics,* 137**,** 204902.

JANSSON, A. 2014. *Development of Novel In Situ Microscopy Techniques for the Study of Water Interaction with Soft Materials.* Doctor of Philosophy, Chalmers University of Technology.

JANSSON, A., BOISSIER, C., MARUCCI, M., NICHOLAS, M., GUSTAFSSON, S., HERMANSSON, A.-M. & OLSSON, E. 2014. Novel Method for Visualizing Water Transport Through Phase-Separated Polymer Films. *Microscopy and Microanalysis,* 20**,** 394-406.

JANSSON, A., NAFARI, A., SANZ-VELASCO, A., SVENSSON, K., GUSTAFSSON, S., HERMANSSON, A. M. & OLSSON, E. 2013. Novel method for controlled wetting of materials in the environmental scanning electron microscope. *Microsc Microanal,* 19**,** 30-7.

JARKE, A. 2009. *Effect of manufacturing conditions and polymer ratio on the permeability and film morphology of ethyl cellulose and hydroxypropyl cellulose free films produced by using a novel spray method.* Master Thesis, Uppsala University.

JASNOW, D. 1984. Critical phenomena at interfaces. *Reports on Progress in Physics,* 47**,** 1059.

JIN, W., XU, W., GE, H., LI, J. & LI, B. 2015. Coupling process of phase separation and gelation in konjac glucomannan and gelatin system. *Food Hydrocolloids,* 51**,** 188-192.

JINNAI, H., KITAGISHI, H., HAMANO, K., NISHIKAWA, Y. & TAKAHASHI, M. 2003. Effect of confinement on phase-separation processes in a polymer blend observed by laser scanning confocal microscopy. *Physical Review E,* 67**,** 021801.

JONES, R. A. L. & RICHARDS, R. W. 1999. *Polymers at Surfaces and Interfaces,* Cambridge, UK, Cambridge University Press.

JONG, D. 2008. Drug delivery and nanoparticles: Applications and hazards. *International Journal of Nanomedicine***,** 133.

JONKMAN, J. & STELZER, E. 2002. Resolution and Contrast and Two-Photon Microscopy. *Confocal and Two-Photon Microscopy: Foundations, Applications and Advances.* New York: Wiley.

KENDON, V. M., CATES, M. E., PAGONABARRAGA, I., DESPLAT, J.-C. & BLADON, P. 2001. Inertial effects in three-dimensional spinodal decomposition of a symmetric binary fluid mixture: a lattice Boltzmann study. *Journal of Fluid Mechanics,* 440**,** 147-203.

KESELMAN, H. J. & ROGAN, J. C. 1977. The Tukey multiple comparison test: 1953–1976. *Psychological Bulletin,* 84**,** 1050-1056.

KHANDELWAL, M. & ALAN, H. W. 2013. Hierarchical Organisation in the Most Abundant Biopolymer – Cellulose. *MRS Online Proceedings Library,* 1504**,** 10.1557/opl.2013.379.

KIM, J. Y., CHO, C. H., PALFFY-MUHORAY, P. & KYU, T. 1993. Polymerization-induced phase separation in a liquid-crystal-polymer mixture. *Physical Review Letters,* 71**,** 2232-2235.

KLEIN, E. 2002. The role of extended-release benzodiazepines in the treatment of anxiety: a risk-benefit evaluation with a focus on extended-release alprazolam. *The Journal of clinical psychiatry,* 63 Suppl 14**,** 27-33.

KLEMM, D., HEUBLEIN, B., FINK, H. P. & BOHN, A. 2005. Cellulose: fascinating biopolymer and sustainable raw material. *Angewandte Chemie International Edition,* 44**,** 3358-93.

KONINGSVELD, R., KONINGSVELD, R., STOCKMAYER, W. H. & NIES, E. 2001. *Polymer Phase Diagrams: A Textbook*, Oxford University Press.

KOUIJZER, S., MICHELS, J. J., VAN DEN BERG, M., GEVAERTS, V. S., TURBIEZ, M., WIENK, M. M. & JANSSEN, R. A. J. 2013. Predicting Morphologies of Solution

Processed Polymer:Fullerene Blends. *Journal of the American Chemical Society,* 135**,** 12057-12067.

LANGER, R. & PEPPAS, N. 1983. Chemical and Physical Structure of Polymers as Carriers for Controlled Release of Bioactive Agents: A Review. *Journal of Macromolecular Science, Part C,* 23**,** 61-126.

LANGER, R. & PEPPAS, N. A. 2003. Advances in biomaterials, drug delivery, and bionanotechnology. *AIChE Journal,* 49**,** 2990-3006.

LAUGER, J., LAY, R. & GRONSKI, W. 1994. The percolation-to-cluster transition during spinodal decomposition of an off-critical polymer mixture. Observation by light scattering and optical microscopy. *Journal of Chemical Physics,* 101**,** 7181-7184.

LI, X., LIU, Y., LI, N., XIE, D., YU, J., WANG, F. & WANG, J. 2016. Studies of phase separation in soluble rice protein/different polysaccharides mixed systems. *LWT - Food Science and Technology,* 65**,** 676-682.

LI, X., XING, R., ZHANG, Y., HAN, Y. & AN, L. 2004. Molecular weight effects on the phase morphology of PS/P4VP blend films on homogeneous SAM and heterogeneous SAM/Au substrates. *Polymer,* 45**,** 1637-1646.

LIPIN, A. A. & LIPIN, A. G. 2022. Prediction of coating uniformity in batch fluidized-bed coating process. *Particuology,* 61**,** 41-46.

LORÉN, N., HERMANSSON, A.-M., WILLIAMS, M. A. K., LUNDIN, L., FOSTER, T. J., HUBBARD, C. D., CLARK, A. H., NORTON, I. T., BERGSTRÖM, E. T. & GOODALL, D. M. 2001. Phase Separation Induced by Conformational Ordering of Gelatin in Gelatin/Maltodextrin Mixtures. *Macromolecules,* 34**,** 289-297.

LORÉN, N., LANGTON, M. & HERMANSSON, A. M. 2007. *Confocal fluorescence microscopy (CLSM) for food structure characterisation*.

MARUCCI, M., HJÄRTSTAM, J., RAGNARSSON, G., ISELAU, F. & AXELSSON, A. 2009. Coated formulations: new insights into the release mechanism and changes in the film properties with a novel release cell. *Journal of Controlled Release,* 136**,** 206-12.

MARUCCI, M., RAGNARSSON, G., VON CORSWANT, C., WELINDER, A., JARKE, A., ISELAU, F. & AXELSSON, A. 2011. Polymer leaching from film coating: effects on the coating transport properties. *International Journal of Pharmaceutics* 411**,** 43-8.

MCDONOUGH, R., CUETO, R., PHILLIES, G. D. J., RUSSO, P. S., DORMAN, D. & STRELETZKY, K. A. 2015. Fluorescent Labeling Can Alter Polymer Solution Dynamics. *Macromolecules,* 48**,** 7245-7255.

MEYERHOFER, D. 1978. Characteristics of resist films produced by spinning. *Journal of Applied Physics,* 49**,** 3993–3997.

MEZZENGA, R., SCHURTENBERGER, P., BURBIDGE, A. & MICHEL, M. 2005. Understanding foods as soft material. *Nature Materials,* 4**,** 729-740.

MICHELS, J. J. 2011. Surface-Directed Spinodal Decomposition of Solvent-Quenched Organic Transistor Blends. *ChemPhysChem,* 12**,** 342-348.

MOKARIAN-TABARI, P., GEOGHEGAN, M., HOWSE, J. R., HERIOT, S. Y., THOMPSON, R. L. & JONES, R. A. L. 2010. Quantitative evaluation of evaporation rate during spin-coating of polymer blend films: Control of film structure through defined-atmosphere solvent-casting. *European Physical Journal E,* 33**,** 283-289.

MORRIS, E. R., CUTLER, A. N., ROSS-MURPHY, S. B. & REES, D. A. 1981. Concentration and shear rate dependence of viscosity in random coil polysccharide solutions. *Carbohydrate Polymers,* 1**,** 5-21.

MULLER-BUSCHBAUM, P. & STAMM, M. 2001. Film Thickness dependence of the domain size in weakly incompatible thin polymer blend films. *Colloid Polymer Science,* 279**,** 376-381.

NGUYEN, T. & LATKANY, R. 2011. Review of hydroxypropyl cellulose ophthalmic inserts for treatment of dry eye. *Clinical ophthalmology,* 5**,** 587-591.

OTTESEN, V. 2011. Nucleation and growth. *In:* GROWTH, N. A. (ed.) *Wikimedia.*

OUGIZAWA, T. & INOUE, T. 1986. UCST and LCST Behavior in Polymer Blends and Its Thermodynamic Interpretation. *Polymer Journal,* 18**,** 521-527.

PAWLEY, J. 2006. *Handbook of Biological Confocal Microscopy*, Springer US.

PETERSSON, M. 2005. Characterization of Phase Separation in Film Forming Biopolymer Mixtures. *Biomacromolecules,* 6**,** 932-941.

PICKER-FREYER, K. M. & DÜRIG, T. 2007. Physical mechanical and tablet formation properties of hydroxypropylcellulose: In pure form and in mixtures. *AAPS PharmSciTech,* 8**,** 82.

PICULELL, L., BERGFELDT, K. & NILSSON, S. 1995. Factors Determining Phase Behaviour of Multi Component Polymer Systems. *Meeting, Biopolymer mixtures.* Nottingham: Nottingham University Press.

PLAYNE, D. P. & HAWICK, K. A. Data Parallel Three-Dimensional Cahn-Hilliard Field Equation Simulation on GPUs with CUDA. *In:* PDTA, ed., 2009.

PURI, S. & BINDER, K. 1994. Surface effects on spinodal decomposition in binary mixtures and the interplay with wetting phenomena. *Physical Review E,* 49**,** 5359-5377.

RAJ KUMAR, A. 2012. Drying Induced Phase Separation. *Journal of Chemical Engineering,* 27.

RAWLINGS, J. M. & LUCAS, M. L. 1985. Plastic pH electrodes for the measurement of gastrointestinal pH. *Gut,* 26**,** 203-207.

RENKEMA, J. M. S. 2004. Relations between rhological properties and network structure of soy protein gels. *Food Hydrocolloids,* 18**,** 39-47.

RHODES, C. T. & PORTER, S. C. 1998. Coatings for controlled-release drug delivery systems. *Drug Development and Industrial Pharmacy,* 24**,** 1139-54.

RÖDING, M., FAGER, C., OLSSON, A., VON CORSWANT, C., OLSSON, E. & LORÉN, N. 2021. Three-dimensional reconstruction of porous polymer films from FIB-SEM nanotomography data using random forests. *Journal of Microscopy,* 281**,** 76-86.

SAGUI, C. & GRANT, M. 1999. Therory of nucleation and growth during phase separation. *Physical Review E,* 59.

SAKELLARIOU, P. & ROWE, R. C. 1995. Interactions in cellulose derivative films for oral drug delivery. *Progress in Polymer Science,* 20**,** 889-942.

SAKELLARIOU, P., ROWE, R. C. & WHITE, E. F. T. 1985. The thermomechanical properties and glass transition temperatures of some cellulose derivatives used in film coating. *International Journal of Pharmaceutics,* 27**,** 267-277.

SCHAEFER, C. 2016. *Theory of nanostructuring in solvent-deposited thin polymer films.* Doctoral Thesis, Eindhoven University of Technology.

SCHAEFER, C., MICHELS, J. J. & VAN DER SCHOOT, P. 2016. Structuring of Thin-Film Polymer Mixtures upon Solvent Evaporation. *Macromolecules,* 49**,** 6858-6870.

SCHAEFER, C., VAN DER SCHOOT, P. & MICHELS, J. J. 2015a. Structuring of polymer solutions upon solvent evaporation. *Physical Review E,* 91**,** 022602 1-6.

SCHAEFER, C., VAN DER SCHOOT, P. & MICHELS, J. J. 2015b. Structuring of polymer solutions upon solvent evaporation. *Physical Review E,* 91**,** 022602.

SCHMID, B., SCHINDELIN, J., CARDONA, A., LONGAIR, M. & HEISENBERG, M. 2010. A high-level 3D visualization API for Java and ImageJ. *BMC Bioinformatics,* 11**,** 274.

SCHOBER, T. J., BEAN, S. R., BOYLE, D. L. & PARK, S.-H. 2008. Improved viscoelastic zein–starch doughs for leavened gluten-free breads: Their rheology and microstructure. *Journal of Cereal Science,* 48**,** 755-767.

SCHOLTEN, E., M. C. SAGIS, L. & VAN DER LINDEN, E. 2004a. Coarsening Rates of Bicontinuous Structures in Polymer Mixtures. *Macromolecules,* 38**,** 3515-3518.

SCHOLTEN, E., VISSER, J. E., SAGIS, L. M. C. & VAN DER LINDEN, E. 2004b. Ultralow Interfacial Tensions in an Aqueous Phase-Separated Gelatin/Dextran and Gelatin/Gum Arabic System: A Comparison. *Langmuir,* 20**,** 2292-2297.

SCRIVEN, L. E. & STERNLING, C. V. 1960. The Marangoni Effects. *Nature,* 187**,** 186-188.

SERSHEN, S. & WEST, J. 2002. Implantable, polymeric systems for modulated drug delivery. *Advanced Drug Delivery Reviews,* 54**,** 1225-1235.

SHAW, M. & MACKNIGHT, W. 2005. *Introduction to Polymer Viscoelasticity*, Wiley.

SHEPPARD, C. & SHOTTON, D. 1997. *Confocal Laser Scanning Microscopy*, Springer Singapore.

SHOTTON, D. 1989. Confocal scanning optical microscopy and its applications for biological specimens. *Journal of Cell Science,* 94**,** 175.

SIGGIA, E. D. 1979. Late stages of spinodal decomposition in binary mixtures. *Physical Review A,* 20**,** 595-605.

SOLON, A. P., STENHAMMAR, J., CATES, M. E., KAFRI, Y. & TAILLEUR, J. 2018. Generalized thermodynamics of motility-induced phase separation: phase equilibria, Laplace pressure, and change of ensembles. *New Journal of Physics,* 20**,** 075001 1-23.

STEWART, S., DOMÍNGUEZ-ROBLES, J., DONNELLY, R. & LARRAÑETA, E. 2018. Implantable Polymeric Drug Delivery Devices: Classification, Manufacture, Materials, and Clinical Applications. *Polymers,* 10**,** 1379.

SUNG, L., KARIM, A., DOUGLAS, J. F. & HAN, C. C. 1996. Dimensional Crossover in the Phase Separation Kinetics of Thin Polymer Blend Films. *Physical Review Letters,* 76**,** 4368-4371.

TAKENO, H., NAKAMURA, E. & HASHIMOTO, T. 1999. Heterogeneous percolation-to-cluster transition in phase separation of an off-critical polymer mixture. *Journal of Chemical Physics,* 110**,** 3612-3620.

TANAKA, H. 1994. Double phase separation in a confined, symmetric binary mixture: Interface quench effect unique to bicontinuous phase separation. *Physical Review Letters,* 72**,** 3690-3693.

TANAKA, H. 2001. Interplay between wetting and phase separation in binary fluid mixtures: roles of hydrodynamics. *Journal of Physics: Condensed Matter,* 13**,** 4637–4674.

TANAKA, H. 2012. Viscoelastic phase separation in soft matter and foods. *Faraday Discussions,* 158.

TANAKA, H. & ARAKI, T. 1998. Spontaneous Double Phase Separation Induced by Rapid Hydrodynamic Coarsening in Two-Dimensional Fluid Mixtures. *Physical Review Letters,* 81**,** 389-392.

TANAKA, H. & NISHI, T. 1985. New types of phase separation behavior during the crystallization process in polymer blends with phase diagram. *Physical Review Letters,* 55**,** 1102-1105.

TIWARI, G., TIWARI, R., SRIWASTAWA, B., BHATI, L., PANDEY, S., PANDEY, P. & BANNERJEE, S. K. 2012. Drug delivery systems: An updated review. *International Journal of Pharmaceutical Investigation,* 2**,** 2-11.

TOLSTOGUZOV, V. 2003a. Some thermodynamic considerations in food formulation. *Food Hydrocolloids,* 17**,** 1-23.

TOLSTOGUZOV, V. 2003b. Thermodynamic considerations of starch functionality in foods. *Carbohydrate Polymers,* 51**,** 99-111.

TOOLAN, D. T. W. & HOWSE, J. R. 2013. Development of in situ studies of spin coated polymer films. *Journal of Materials Chemistry C,* 1**,** 603-616.

TRAN, T. L., CHAN, P. K. & ROUSSEAU, D. 2006. Morphology control in symmetric polymer blends using two-step phase separation. *Computational Materials Science,* 37**,** 328-335.

UHRICH, K. E., CANNIZZARO, S. M., LANGER, R. S. & SHAKESHEFF, K. M. 1999. Polymeric Systems for Controlled Drug Release. *Chemical Reviews,* 99**,** 3181-3198.

VAN FRANEKER, J. J., WESTHOFF, D., TURBIEZ, M., WIENK, M. M., SCHMIDT, V. & JANSSEN, R. A. J. 2015. Controlling the Dominant Length Scale of Liquid–Liquid Phase Separation in Spin-coated Organic Semiconductor Films. *Advanced Functional Materials,* 25**,** 855-863.

WALHEIM, S., BÖLTAU, M., MLYNEK, J., GEORG, K. & STEINER, U. 1997. Structure Formation via Polymer Demixing in Spin-Cast Films. *Macromolecules,* 30**,** 4995-5003.

WASSÉN, S., BORDES, R., GEBÄCK, T., BERNIN, D., SCHUSTER, E., LORÉN, N. & HERMANSSON, A.-M. 2014. Probe diffusion in phase-separated bicontinuous biopolymer gels. *Soft Matter,* 10**,** 8276-8287.

WASSÉN, S., LORÉN, N., VAN BEMMEL, K., SCHUSTER, E., RONDEAU, E. & HERMANSSON, A.-M. 2013. Effects of confinement on phase separation kinetics and final morphology of whey protein isolate–gellan gum mixtures. *Soft Matter,* 9**,** 2738–2749.

WILLIAMS, E. L., GORELIK, S., PHANG, I., BOSMAN, M., VIJILA, C., SUBRAMANIAN, G. S., SONAR, P., HOBLEY, J., SINGH, S. P., MATSUZAKI, H., FURUBE, A. & KATOH, R. 2013. Nanoscale phase domain structure and associated device performance of organic solar cells based on a diketopyrrolopyrrole polymer. *RSC Advances,* 3.

WILTZIUS, P., CUMMING, A. W. & SHI, B. Q. 1994. Domain growth and wetting in phase-separating fluid mixtures. *Macromolecular Symposia,* 79**,** 71-80.

WISE, M. B. & MILLETT, P. C. 2018. Two-dimensional bicontinuous structures from symmetric surface-directed spinodal decomposition in thin films. *Physical Review E,* 98**,** 022601.

YAMAMURA, M., NISHIO, T., TOSHIHISA, K. & ATACHI, K. 2002. Evaporation-induced pattern formation in polymer films via secondary phase separation. *Chemical Engineering Science,* 57**,** 2901-2905.

YIANTSIOS, S. G., SERPETSI, S. K., DOUMENC, F. & GUERRIER, B. 2015. Surface deformation and film corrugation during drying of polymer solutions induced by Marangoni phenomena. *International Journal of Heat and Mass Transfer,* 89**,** 1083-1094.

ZHANG, F., JESPERSEN, K. G., BJÖRSTRÖM, C., SVENSSON, M., ANDERSSON, M. R., SUNDSTRÖM, V., MAGNUSSON, K., MOONS, E., YARTSEV, A. & INGANÄS, O. 2006. Influence of Solvent Mixing on the Morphology and Performance of Solar Cells Based on Polyfluorene Copolymer/Fullerene Blends. *Advanced Functional Materials,* 16**,** 667-674.

ZHOU, B., LIU, J., YE, T., WANG, Y., XU, W. & LI, B. 2014. Phase separation in mixtures of ovalbumin and konjac glucomannan: physicochemical and microscopic investigations. *Int J Biol Macromol,* 70**,** 167-73.

ZOLALI, A. M. & FAVIS, B. D. 2017. Partial to complete wetting transitions in immiscible ternary blends with PLA: the influence of interfacial confinement. *Soft Matter,* 13**,** 2844-2856.

ZOUMPOULI, G. A. & YIANTSIOS, S. G. 2016. Hydrodynamic effects on phase separation morphologies in evaporating thin films of polymer solutions. *Physics of Fluids,* 28**,** 082108.